

**Inaugural dissertation**  
for  
obtaining the doctoral degree  
of the  
Combined Faculty of Mathematics, Engineering and Natural Sciences  
of the  
Ruprecht - Karls - University  
Heidelberg

presented by  
M.Sc. Valentin Schoop  
born in Rastatt, Germany  
Oral examination: 25.5.2022



**Proximity biotinylation at organelle contact sites  
reveals GRAMD1B as a sterol transporter  
acting at the lysosome-ER interface**

**Referees:**

Prof. Dr. Britta Brügger

Dr. Doris Höglinger



## Abstract

Contact sites between membranes of different cellular organelles are involved in a wide variety of biological processes. While many of the key factors involved in their formation have been identified and many proteins that act primarily at these contact sites have been studied extensively, a comprehensive picture of both the architecture but also the function of these contacts is still missing. This lack of knowledge is to a large degree due to the small dimensions of these interfacing membranes, which make their identification and analysis using conventional methods rather challenging. This work establishes a proximity-labelling assay based on a split biotin ligase connected to known protein tether-pairs at three distinct contact sites of the endoplasmic reticulum (ER) with lysosomes, mitochondria and endosomes, respectively. Proteins that were biotinylated at these membrane contact sites were then identified by mass spectrometry based proteomics. The resulting list of identified hits contained both novel proteins, as well as proteins that had previously been reported to fulfill a role at membrane contact sites, highlighting the efficacy of the assay.

The function of one such protein, GRAMD1B, was investigated further. This protein is essential for non-vesicular cholesterol import to the ER from the plasma membrane, but was also found to locate to contact sites with lysosomes and interact with the major lysosomal cholesterol exporting protein, NPC1. Results of the split biotin ligase assay confirmed a localization at lysosome-ER contact site, which led us to further study its function at this contact. Using a lysosomally prelocalized, modified cholesterol probe in GRAMD1B-overexpressing cells, pulse-chase measurements of cholesterol esterification suggested an involvement of GRAMD1B in two separate lysosome-to-ER transport processes with different temporal scales: A fast and direct cholesterol transport at lysosome-ER contacts dependent on NPC1 as well as an import from the plasma membrane to the ER at slower timescales. This was substantiated by the fact that the impact of GRAMD1B-overexpression on the faster transport process was reduced by NPC1-deficiency, while trapping of cholesterol at the plasma membrane only reduced the effect at later time points. In addition, live-cell microscopic analysis showed GRAMD1B's ability to recruit ER tubules to cholesterol-laden lysosomes and confirmed a dependency on the presence of NPC1 in the lysosomal membrane. This further strengthens the hypothesis of a dual role of GRAMD1B in the transport of cholesterol to the ER, with spatial coupling of two cholesterol transporters at the lysosome-ER interface.

Overall, this work shows that proximity labelling using split biotin ligase fragments fused to known contact site tether pairs is a powerful tool to identify proteins acting at organelle contacts. One such protein, GRAMD1B, acts in multiple routes of subcellular cholesterol trafficking, where this work focusses on its function in direct lysosome-to-ER transport of sterols. The applied methods, particularly the use of modified cholesterol probes prelocalized to lysosomes to observe lysosomal egress, as well as the insights gained from studying GRAMD1B's actions at lysosome-ER contacts, will contribute to a more comprehensive understanding of subcellular cholesterol homeostasis, which, in turn, is relevant for a wide variety of physiological and pathophysiological processes.

## Zusammenfassung

Kontaktstellen zwischen Membranen verschiedener Zell-Organellen spielen eine wichtige Rolle in zahlreichen biologischen Abläufen. Viele der Schlüsselfaktoren, die an ihrer Bildung beteiligt sind, wurden bereits identifiziert, und viele Proteine, die vorrangig an diesen Kontaktstellen agieren, sind ausgiebig untersucht worden – doch was bisher aussteht, ist ein vollständiges Bild sowohl der Architektur als auch der Funktion dieser Kontakte. Dass dieses Wissen noch fehlt, liegt zu einem großen Teil an den geringen Ausmaßen dieser miteinander in Verbindung stehenden Membranen, was ihre Identifikation und Analyse mit herkömmlichen Methoden zu einer großen Herausforderung macht. Die vorliegende Arbeit etabliert eine Methode zur Proximitäts-Markierung an Membrankontaktstellen, basierend auf einer gespaltenen Biotin-Ligase (Split-BioID), die an drei bekannten Paaren von Tether-Proteinen angebracht wurde, welche sich an Kontaktstellen des endoplasmatischen Retikulums (ER) mit Lysosomen, Mitochondrien oder Endosomen befinden. Proteine, die an diesen Membrankontaktstellen biotinyliert wurden, wurden anschließend durch massenspektrometrische Proteomik identifiziert. Die daraus resultierende Liste der identifizierten Treffer enthielt sowohl neuartige Proteine als auch Proteine, von denen bereits zuvor berichtet worden war, dass sie eine Rolle an Membrankontaktstellen spielen, was die Wirksamkeit dieser Methode unterstreicht.

Die Funktion eines dieser Proteine, GRAMD1B, wurde genauer untersucht. Dieses Protein spielt eine essentielle Rolle für den nicht-vesikulären Cholesterinimport aus der Plasmamembran in das endoplasmatische Retikulum, es wurde jedoch auch festgestellt, dass es sich an Kontaktstellen mit Lysosomen befindet und mit dem wichtigsten lysosomalen Cholesterinexport-Protein, NPC1, interagiert. Die Ergebnisse des Split-BioID Ansatzes bestätigten ein vermehrtes Vorkommen des Proteins an der Kontaktstelle zwischen Lysosomen und dem ER, was mich dazu veranlasste, seine Funktion an dieser Position genauer zu untersuchen. Unter Verwendung eines lysosomal vorlokalisierenden, modifizierten Cholesterinanalogs in GRAMD1B-überexprimierenden Zellen, deuteten Puls-Chase-Messungen der Cholesterinveresterung auf eine Beteiligung von GRAMD1B an zwei separaten Transportprozessen von Lysosomen zum ER mit unterschiedlichen Zeitskalen hin: Ein schneller und direkter Cholesterintransport an Lysosom-ER-Kontaktstellen, der von NPC1 abhängig ist, sowie ein Import von der Plasmamembran zum ER über eine längere Zeitspanne. Dies wurde durch die Tatsache

untermauert, dass der Einfluss der GRAMD1B-Überexprimierung auf den schnellen Transportprozess durch einen Mangel an NPC1 verringert wurde, während die Immobilisierung von Cholesterin an der Plasmamembran den Effekt nur zu späteren Zeitpunkten reduzierte. Eine mikroskopische Analyse in lebenden Zellen zeigte darüber hinaus, dass GRAMD1B die Fähigkeit besitzt, ER-Tubuli zu cholesterinbeladenen Lysosomen zu rekrutieren, und bestätigte zudem eine Abhängigkeit von der Präsenz von NPC1 in der lysosomalen Membran. Dies untermauert die Hypothese einer doppelten Rolle von GRAMD1B beim Transport von Cholesterin zum ER, mit einer räumlichen Kopplung von zwei Cholesterintransport-Proteinen an der Kontaktfläche zwischen Lysosom und ER.

Insgesamt zeigt die vorliegende Arbeit, dass die Proximitäts-Markierung unter Verwendung von Fragmenten einer gespaltenen Biotin-Ligase, die mit bekannten Kontaktstellen-Tether-Paaren verknüpft sind, ein leistungsfähiges Werkzeug darstellt, um Proteine zu identifizieren, die an Kontaktstellen von Organellen agieren. Eines dieser Proteine, GRAMD1B, spielt bei mehreren Routen des subzellulären Cholesterintransports eine Rolle, wobei sich die vorliegende Arbeit auf seine Funktion beim direkten Transport von Sterolen von Lysosomen zum ER konzentriert. Die angewandten Methoden, insbesondere die Verwendung eines modifizierten Cholesterinanalogs, das in Lysosomen vorlokalisiert, für die Beobachtung des Austritts aus Lysosomen, sowie die Erkenntnisse, die aus der Untersuchung der Aktivitäten von GRAMD1B an Lysosom-ER-Kontaktstellen gewonnen wurden, werden zu einem umfassenderen Verständnis der subzellulären Cholesterin-Homöostase beitragen, welche wiederum für eine große Bandbreite von physiologischen und pathophysiologischen Prozessen relevant ist.

# Table of Contents

Abstract .....	1
Zusammenfassung .....	3
Table of Contents .....	5
List of Figures .....	7
List of Tables .....	8
1 Introduction .....	11
1.1 Membrane contact sites .....	11
1.1.1 Description and properties of membrane contacts .....	11
1.1.2 Contact site formation and tether proteins .....	12
1.1.3 Methodologies and challenges in studying MCSs .....	13
1.1.4 Functions of membrane contact sites .....	16
1.1.5 Intracellular lipid transport .....	16
1.1.6 Lipid transport at membrane contact sites .....	17
1.2 Cholesterol .....	18
1.2.1 Intracellular sterol distribution .....	18
1.2.2 Synthesis and ER-export of cholesterol .....	18
1.2.3 The SREBP processing pathway .....	18
1.2.4 LDL-cholesterol uptake and lysosomal export .....	20
1.2.5 Lysosomal cholesterol export defects .....	23
1.2.6 Plasma membrane cholesterol .....	24
1.3 Multifunctional lipid probes .....	27
1.3.1 Organelle targeted caged cholesterol .....	28
2 Aim of this thesis .....	31
3 Results and Discussion .....	32
3.1 Split-BioID at membrane contact sites .....	32
3.1.1 Designing and testing Split-BioID bait pairs .....	32
3.1.2 Proteomic analysis of targets of Split-BioID at MCS .....	35
3.1.3 Correcting the localization of Split-BioID baits by stable expression .....	40
3.1.4 Split-BioID in stable cells produces a different list of proteins .....	43
3.1.5 Validation of proteins of interest .....	50
3.2 GRAMD1B at Lysosome-ER contact sites .....	56
3.2.1 Lysosome to ER transport of Lyso-pacCholesterol is facilitated by GRAMD1B ...	57
3.2.2 GRAMD1B is recruited to LDL-rich endosomes in an NPC1 dependent manner.	65
4 Conclusion and Outlook .....	71
5 Materials and Methods .....	75

5.1	Reagents, Buffers and Media.....	75
5.2	Plasmids and Primers .....	76
5.2.1	Plasmids .....	76
5.2.2	DNA oligonucleotides .....	77
5.3	Antibodies .....	78
5.4	DNA extraction, amplification and cloning .....	79
5.5	Quantitative RT-PCR .....	79
5.6	Cultivation of human cell lines.....	80
5.7	Generation of stable cell lines .....	80
5.8	Generation of NPC1-KO cell line.....	81
5.9	Cell lysis .....	82
5.10	Protein concentration measurements.....	82
5.11	Western blot analysis.....	83
5.12	Immunofluorescence staining.....	83
5.13	Fluorescence microscopy .....	84
5.14	SplitBioID experiments.....	84
5.14.1	Cloning of BioID constructs .....	84
5.14.2	Biotinylation screening .....	84
5.14.3	Split-BioID assay for proteomic analysis .....	85
5.14.4	Immunoblot analysis of proteins of interest.....	86
5.14.5	LC-MS/MS measurements .....	86
5.14.6	Analysis of mass spectrometric data .....	87
5.15	Lyso-pacCholesterol esterification assays.....	88
5.15.1	Lyso-pacCholesterol esterification assays in the presence of ALOD4 .....	89
5.16	Expression, purification and evaluation of ALOD4.....	89
5.16.1	Expression of ALOD4.....	89
5.16.2	Purification of ALOD4.....	90
5.16.3	Fluorescence labelling of ALOD4 .....	91
5.16.4	ALOD4 binding assay .....	91
5.17	GRAMD1B relocalization analysis.....	92
5.17.1	Image acquisition .....	92
5.17.2	Data analysis .....	93
	List of Abbreviations .....	94
	Bibliography.....	98
	Appendix .....	113
	Acknowledgements .....	126

## List of Figures

Figure 1: Intracellular membrane contact sites.....	12
Figure 2: The study of membrane contact sites .....	15
Figure 3: Modes of monomeric lipid exchange.....	17
Figure 4: Uptake and metabolism of LDL-particles .....	20
Figure 5: Proteins involved in cholesterol export from lysosomes .....	21
Figure 6: Uptake, transport and metabolism of Lyso-pacCholesterol .....	29
Figure 7: Split-BioID at membrane contact sites .....	31
Figure 8: Cloning of Split-BioID constructs.....	33
Figure 9: Initial test of biotinylation activity .....	34
Figure 10: Streptavidin pulldown of biotinylated proteins .....	35
Figure 11: Data analysis workflow and volcano plot of first LC-MS/MS results.....	37
Figure 12: Immunofluorescence imaging of Split-BioID cells.....	39
Figure 13: Cloning of conventional (nonSplit-) BioID constructs.....	40
Figure 14: Biotinylation activity of stable BioID cell lines .....	41
Figure 15: Immunofluorescence imaging of stable cell line biotinylation patterns.....	42
Figure 16: Results of third Split-BioID proteomic screen (Volcano plot) .....	43
Figure 17: Results of third Split-BioID proteomic screen (Volcano plot) .....	46
Figure 18: Immunoblot of MAVS biotinylated by different BioID constructs .....	51
Figure 19: Immunoblot analysis of biotinylation levels of proteins of interest.....	53
Figure 20: Quantification of POI levels in streptavidin pulldown .....	54
Figure 21: Workflow of the Lyso-pacCholesterol esterification assay.....	57
Figure 22: TLC analysis of Lyso-pacCholesterol esterification. ....	59
Figure 23: Validation of cell surface binding by purified ALOD4.....	61
Figure 24: TLC analysis of Lyso-pacChol esterification in the presence of ALOD4 .....	63
Figure 25: Analysis workflow of GRAMD1B recruitment to LDL containing endosomes.....	66
Figure 26: Results of recruitment analysis of GRAMD1B to LDL particles .....	68

## List of Tables

Table 1: Overview of studies using proximity labeling to research MCS.....	15
Table 2: Significant hits of first Split-BioID screen (transient expression).....	38
Table 3: Result evaluation of first proteomic screen.....	39
Table 4: Significant hits of second Split-BioID screen (stable expression) .....	44
Table 5: Result evaluation of second proteomic screen .....	45
Table 6: Significant hits of third Split-BioID screen (stable expression).....	47
Table 7: Result evaluation of third proteomic screen.....	48
Table 8: Overlaps between own and published proteomic datasets.....	48
Table 9: Results of the recruitment analysis of GFP-GRAMD1B to LDL particles .....	68

“It’s not the mountain we conquer, but ourselves”

– Sir Edmund Hillary



“With chopsticks, I cut through the dark-skinned egg, releasing molten yoke into waiting broth.

Face bathed in the warming steam, I tasted.

*Sheltered from the rain*

*Soothing train, ramen-numbed brain*

*I reap contentment*

With the Zen meal consumed and consumed by the Zen meal, I exited back into the chaotic Tokyo night.”

– Gordon Vanstone





# 1 Introduction

## 1.1 Membrane contact sites

The evolution of higher life forms began with the development of intracellular organelles, allowing primitive life forms to divide their internal volume into multiple separate compartments, which increased their ability to adapt to a wider spectrum of environmental conditions [1]. These cellular organelles differ not only in their chemical properties such as ion concentration, pH range or redox-status, which allow for a wider array of parallel metabolic processes, but they also harbor very different subsets of proteins and lipids [2]. In order for all organelles to work together and form a functional living organism, these membrane-delimited compartments needed to be able to maintain highly efficient communication and exchange of materials with each other. Such an exchange of proteins, metabolites and signaling molecules occurs successfully via budding, trafficking and fusion of membrane vesicles between organelles [3]. However, only in the last two decades it has become apparent, that a large part of intracellular transport and signaling between two organelles rather occurs in a non-vesicular fashion at regions where membranes form close contacts.

### 1.1.1 Description and properties of membrane contacts

At these so-called membrane contact sites (MCSs), two organelles are found in very close apposition without touching or fusing. The distance of the membranes can vary depending on the organism and the participating organelles but was observed to be in the range between 10-30 nm in the majority of cases [4–6]. More variable is the lateral extent of the contact sites, reaching from small patches of ~10 nm diameter to extensive sheets that cover up to 40% of the plasma membrane (PM) with contacts to the endoplasmic reticulum (ER) [5,7]. Depending on their molecular function, contact sites also vary in their temporal stability. Signaling or stress induced MCSs for example seem to be more dynamic with interactions as short as a few seconds [8,9], while MCSs that are involved in organellar restructuring or cell movement were observed in yeast to last for minutes [10,11] or even permanently [12].

While some prominent organellar interactions like PM-ER or ER-mitochondria contact sites have already been identified in the 1950s by electron microscopy [13,14], we only

recently discovered how ubiquitous and manifold MCSs really are and that essentially every cellular compartment forms these contacts with other organelles (Figure 1) [15,16].

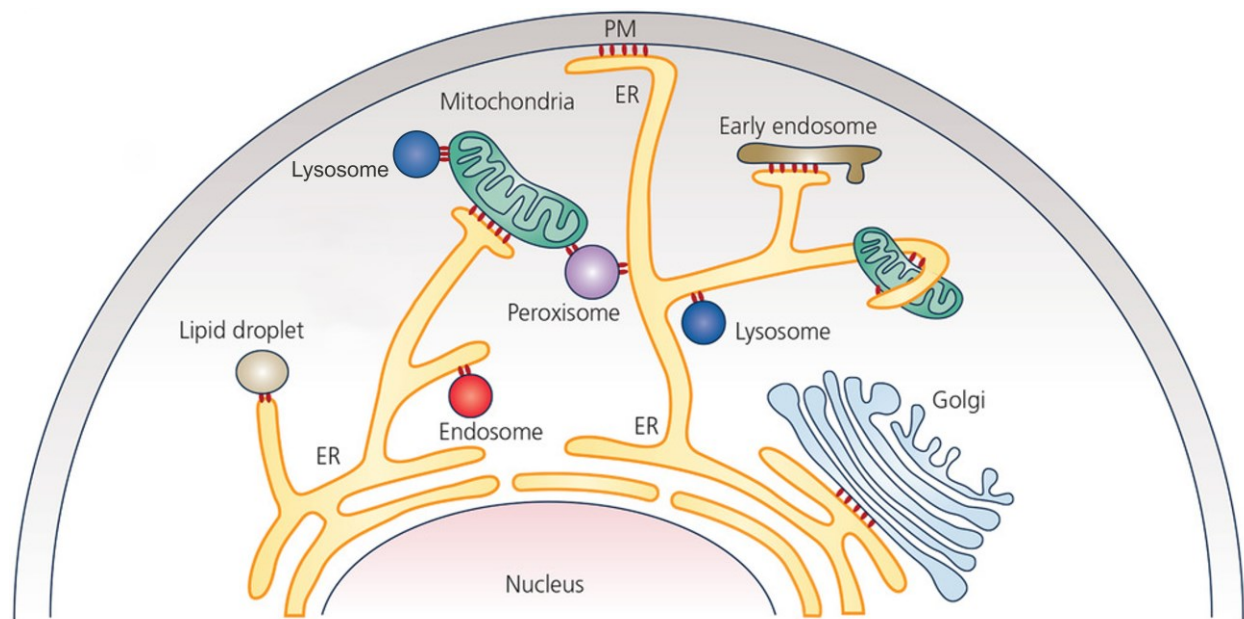


**Figure 1:** Intracellular membrane contact sites. Membrane contact sites are regions of close apposition of two different organelles. They are formed by essentially all cellular organelles and are imperative for a variety of molecular functions. Adapted from Jing et al. [17] with permission under CC BY-NC 4.0

### 1.1.2 Contact site formation and tether proteins

Membrane contact sites are formed and maintained by proteins, which span the gap between two organellar membranes and physically tether them to each other. This tethering can be mediated by soluble or transmembrane proteins featuring domains for binding to membrane lipids or to other transmembrane proteins [18]. These protein-protein interactions are often mediated by the binding of conserved domains to sequence motifs. The most common of these interactions is the binding of proteins that exhibit an FFAT motif (two phenylalanines in an acidic track), to the highly abundant VAP-proteins (vesicle-associated membrane protein (VAMP) associated protein) in the ER membrane [19–21]. More recent definitions of tethers attribute an additional function at the MCS they establish, instead of merely increasing the affinity of the two organelles for each other [1]. Examples for this are lipid transporters such as the oxysterol binding protein (OSBP), which acts as a tether between ER and the Golgi apparatus [22] and the calcium release-activated channel protein ORAI, which binds the ER membrane protein STIM1 (stromal interaction molecule 1) in order to promote calcium influx into the ER [23].

Another new understanding about tethers is that most MCSs between the same two organelles can be formed by multiple different tether pairs [24]. This can be either for reasons of increased robustness if one of the tether pairs fails [25] or because different tether pairs form different MCSs with individual cellular functions [11,26,27]. Some tether proteins, including the yeast sterol transporter Ltc1/Lam6 [28,29] and the lysosomal StART-domain containing protein 3 (STARD3) [30], were also found to localize to multiple different contact sites or were observed to relocalize to a different MCS in response to cellular stress [31].

### 1.1.3 Methodologies and challenges in studying MCSs

Since tether proteins hold the two opposing membranes in a distance of below 30 nm, it is very difficult to study those using conventional microscopic methods, which are restricted by the diffraction limit of light. While some studies have successfully applied fluorescence microscopy to study membrane contact sites [15], most efforts have been focusing on the development of various other methods to overcome these problems [32]. Electron microscopy (EM) has been used very successfully in the study of MCS, due to its very high resolution and good contrast in membrane staining (Figure 2A) [30,33–36]. However, since EM is not applicable in living cells and requires fixation and immunologic labelling in order to identify the localization of target-proteins, transient or rarely occurring interactions of organelles may be missed. Another approach is the use of split fluorophores, whose inactive fragments are attached to different organellar membranes. Upon organellar contact formation the two fragments come in close proximity and are able to recombine and fluoresce, thereby marking the extent, shape and position of the MCSs [16]. While this provides a very clear indication for MCS formation in living cells, concerns remain whether the overexpression of these split fluorophores might artificially induce organellar tethering.

#### 1.1.3.1 Proximity labelling at membrane contact sites

Instead of focusing on MCS visualization, other methods rather aim at the discovery of unknown contact site proteins, for example by employing biochemical purification of interfacing membranes, which is followed by protein identification via immunoblotting or proteomic analysis [37–40]. This method, however, relies on either strong contact site formation that endures cell lysis and fractionation or leads to the enrichment of *in vitro*

interacting membrane proteins. Therefore, results of these studies are expected to miss many key components, while also being riddled with contaminants [41]. In order to omit purification of intact membranes, *in vivo* proximity-labelling techniques have been developed, that can be used to identify proteins at membrane contact sites. An overview of these methods is presented in

Table 1.

The most common proximity labelling methods release activated biotin molecules that covalently bind to any protein in a ~10 nm radius. This allows for subsequent affinity purification of the biotinylated proteins and their identification using mass spectrometry. For example, expressing an engineered organelle-targeted ascorbate peroxidase (APEX2) and adding H<sub>2</sub>O<sub>2</sub> and biotin-phenol to the cells, resulted in a comprehensive list of proteins that interact with the outer mitochondrial membrane [42]. By cross-referencing that list with proteins located at other organelles, one can then identify proteins that must be located at MCS [41,42]. A similar approach uses a method called BioID, which depends on biotinylation via a mutant version of the *E. coli* biotin ligase (BirA). This mutated version, termed BirA\*, is missing its substrate specificity, allowing for promiscuous biotinylation of all proteins in the vicinity after the simple addition of biotin [43,44]. BioID has proven useful in a variety of interaction studies throughout the cell [45–47] and was also successfully applied to study protein interactions at membrane contact sites [47,48]. Because BirA\* is rather large (~35 kDa) and biotinylation quite slow (6 - 24 h), there have been many efforts recently to improve upon its size and efficiency [49,50], as well as to extend its application scenarios. By creating inactive split versions of the biotin ligase that can resume activity upon reassembly (Figure 2B) [51–54], it was possible to make the labeling assay context sensitive, thereby increasing its specificity. In the study of protein complexes, for example, the background biotinylation can be greatly reduced this way, given that only interaction partners of the intact complex are biotinylated and no interaction partners of either of the two bait proteins alone. To apply this approach at membrane contact sites, the two inactive fragments can be anchored to two distinct organellar membranes, which allows proximity labelling to only occur at regions of close membrane apposition [52]. The resulting set of biotinylated proteins should be exclusively located at MCS, eliminating the need to cross-reference the datasets of two independent proximity-labelling assays.

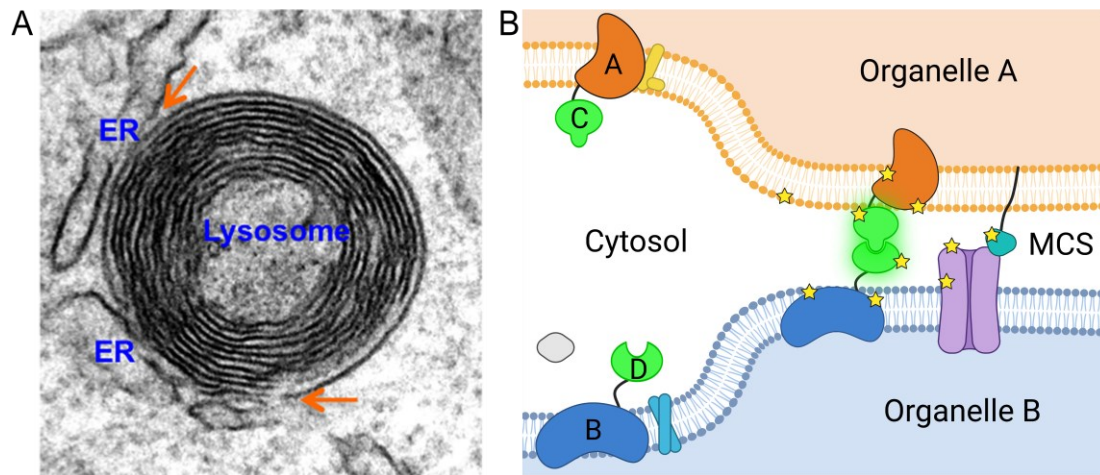


**Figure 2:** The study of membrane contact sites presents a challenge to this day. Visualization of MCS has to be performed at very high resolutions due to the small distances of the membranes. Other techniques focus on the identification of MCS proteins, (A) Electron micrograph of membrane contact sites (arrows) between lysosome and endoplasmic reticulum (ER). Image reprinted from Martello et al. [55] with permission under CC BY-NC 4.0. (B) Context sensitive proximity labelling at membrane contact sites. Membrane proteins of two different organelles (proteins A and B) serve as bait and are fused to inactive fragments of promiscuous biotin ligase BirA\* (proteins C and D). Upon reassembly of the fragments at contact sites, proximal proteins are biotinylated (stars). Created with Biorender.com

**Table 1:** Overview of studies using proximity labeling to research membrane contact sites. OMM = Outer mitochondrial membrane, ERM = endoplasmic reticulum membrane

Technique	Bait	Bait location	Labelling specificity	Ref.
APEX	OMM targeting sequence	OMM	all proteins interacting with mitochondria	[42]
APEX	OMM or ERM targeting sequences	OMM or ERM	all proteins interacting with either mitochondria or ER	[41]
BioID	VAPA, VAPB or MOSPD1-3	ERM	proteins binding to MSP-domains (= FFAT-motif containing proteins)	[48]
BioID	192 distinct proteins	32 different sub-compartments	cell-wide map	[47]
Split-BioID	Tom20 and Sec61B	OMM and ERM	proteins at ER-mitochondria MCS	[52]
Split-TurboID	OMM and ERM targeting sequences	OMM and ERM	proteins at ER-mitochondria MCS	[53]

### 1.1.4 Functions of membrane contact sites

Membrane contact sites have shown to be involved in many crucial cellular processes such as apoptosis, organelle trafficking, dynamics and biogenesis [11,56], as well as in regulation of immune responses [57] and they might even have been essential in the evolution of eukaryotic life itself [58].

Since MCSs can act as regulatory hubs for non-vesicular transport between two organelles, they play a key role in the exchange of molecules or ions like lipids and  $\text{Ca}^{2+}$ , where diffusion over longer distances is not a viable option. Calcium signaling is one of the most important pathways of higher organisms and plays a role in many different processes such as muscle contraction, cell migration, immune response and transcription [12,59]. Since calcium levels in the cytosol are usually more than 100-fold lower than in the ER lumen, any transport between organelles occurs either via vesicle exchange or in a non-vesicular fashion at membrane contact sites in order to avoid non-directed diffusion into the cytosol [23,33,57]. Similarly, the exchange of lipids between cellular membranes is made much more efficient by the use of dedicated vesicular or non-vesicular transport pathways, since spontaneous diffusion, while possible, is highly inefficient due to the disadvantageous interaction of their hydrophobic tails with the aqueous cytosol [60,61].

### 1.1.5 Intracellular lipid transport

The lipid composition of cellular membranes is highly variable throughout the cell, which makes efficient and regulated lipid transport essential for many signaling pathways and maintenance of organelle identity. Even inside the membrane of the same organelle, lipids were found to be distributed very heterogeneously where they form highly enriched micro domains [62,63]. Controlled by flippases, some cellular membranes also exhibit an asymmetric lipid distribution across the two leaflets of the lipid bilayer, which can be essential for signaling events at the cell surface or to steer membrane curvature in vesicle budding events [64].

Intracellular lipid trafficking starts for many lipid species with their biosynthesis at the ER membrane [65], from where they are transported to their intended destinations. These transport routes often involve vesicular export through the cisternae of the cis- and trans-Golgi network, but happens also independently of the Golgi network in a non-vesicular fashion [66], which is thought to occur predominantly at membrane contact sites [67].

### 1.1.6 Lipid transport at membrane contact sites

The monomeric lipid exchange at MCSs is a three-step process, consisting of the desorption from the donor membrane, the traversing of the hydrophilic gap and the insertion of the lipid into the acceptor membrane (Figure 3). The two first steps are energetically quite costly and therefore slow, but the whole process can be significantly accelerated by a group of proteins, termed lipid transport or transfer proteins (LTPs) [68].

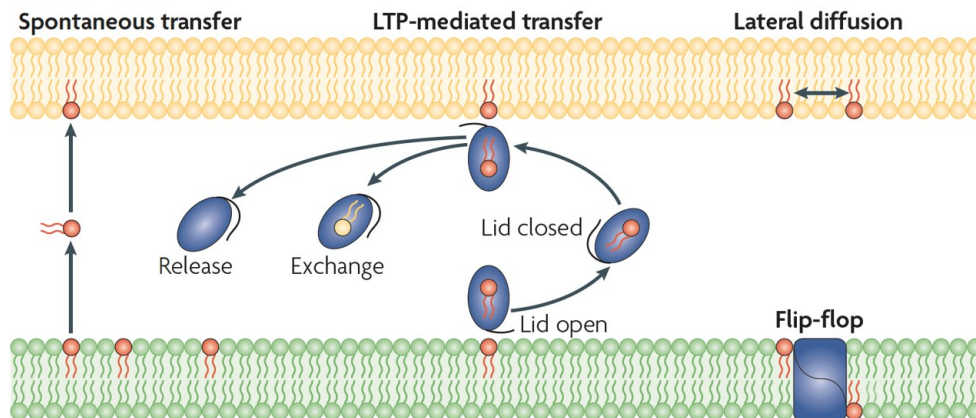


**Figure 3:** Modes of monomeric lipid exchange between two unconnected membranes. Graphic by Sima Lev [65] with permission under license number 5247701089181

This class of proteins was initially discovered *in vitro* as a group of soluble proteins that aid lipid transfer between mitochondria and ER-microsomes [69], but later more and more membrane-bound LTPs were described [70]. Lipid transfer proteins contain hydrophobic pockets, which accept and shield lipids from the aqueous environment, thereby aiding in the diffusion through the gap [65]. Whether LTPs also favor the rate-limiting step of membrane desorption, is still under debate [71].

LTPs can be classified according to their shape or according to their substrate specificity. The structure of lipid transport proteins can be box-like, with a single entry into the hydrophobic pocket and a flexible lid, bridge-like with an elongated groove or even tube-shaped [72]. Box shaped proteins act as shuttles that move between the two exchanging membranes and can be either soluble or anchored to one or both of the membranes via a tether. Some box-like LTPs were shown to drive a counter exchange of two different lipids on their way back and forth between the membranes [22,73,74]. In reference to their lipid binding specificity, LTPs can be grouped into the three main classes of sphingolipid-, phospholipid- and sterol-transfer proteins [65].

This work focusses on the study of intracellular cholesterol transport. Therefore, pathways and transfer proteins involved in it will be explained in more detail in the following chapters.

### 1.2 Cholesterol

#### 1.2.1 Intracellular sterol distribution

Sterols are some of the most important components of biological membranes with cholesterol playing a central role. Cholesterol is highly heterogeneously distributed among intracellular membranes, with up to 90% of all cellular cholesterol residing in the plasma membrane [75] and only 0.5 - 1 % of it being located at the ER [76]. This means that at times the concentration in the plasma membrane is up to 40-50 mol %, while it might be below 5 mol % in the ER membrane, where it is synthesized.

Even small changes in cholesterol concentrations can drastically alter the properties of essentially all membranes, since cholesterol integrates into the phospholipid bilayer of membranes, where it modulates rigidity and permeability and maintains membrane integrity [77]. In order to maintain this delicate balance throughout all organelles, a number of specialized transport proteins have evolved.

#### 1.2.2 Synthesis and ER-export of cholesterol

While only about 5% of total body cholesterol is synthesized *de novo* through the mevalonate pathway at the ER [78], this process still remains essential for the regulation of cholesterol levels throughout the cell. Starting from the ER, newly synthesized cholesterol is transported to the PM either in a vesicular, energy-dependent, but Golgi-independent fashion [79] or through non-vesicular transport pathways directly to the PM [80] and Golgi [81]. Excess cellular cholesterol can be secreted from the cell via the PM-proteins ABCA1 and ABCG1 (ATP-binding cassette sub-family members A1 and G1) into the extracellular space, where it is packed into high-density lipoprotein (HDL) particles with apolipoproteins [82].

#### 1.2.3 The SREBP processing pathway

Since even small changes in local cholesterol concentrations can have strong effects on membrane properties, it is important that sensing of cholesterol levels is tightly coupled to synthesis, uptake and excretion of cholesterol. This is achieved through a feedback mechanism that is mediated by the ER proteins INSIG1 (insulin-induced gene 1 protein), SREBP (Sterol regulatory element-binding protein) and SCAP (SREBP cleavage-activating protein) (Figure 4). If cholesterol levels in the ER are below 5 mol % [76], SCAP

is free to move and able to escort the transcription factor SREBP to the cis-Golgi, where it is proteolytically cleaved and thereby activated and released. Free SREBP can then bind in the nucleus to the sterol regulatory element (SRE) or liver X receptor (LXR), which regulates expression levels of various genes involved in cholesterol biosynthesis and metabolism [83,84]. At ER cholesterol concentrations above 5 mol % [76], binding efficiency of SCAP to the ER-anchored INSIG is increased, which results in the retention of SCAP in the ER membrane [85,86]. In the case of excess cellular cholesterol, esterification by ACAT1 (Acyl-coenzyme A:cholesterol acyltransferase) at the ER membrane allows the cell to store cholesterol in lipid droplets, which are connected to the ER membrane [1]. ACAT1 is also able to directly sense high cholesterol levels in the ER via its sterol-sensing domain (SSD), which results in allosteric activation of enzymatic activity [87]. Similarly, biosynthesis is directly affected by increased ER cholesterol levels through accelerated degradation of the rate-limiting enzyme HMG-CoA reductase (HMGCR), after sterol-binding induced dissociation of its SSD from INSIG [88].

## 1.2.4 LDL-cholesterol uptake and lysosomal export

Another source of cellular cholesterol, besides de novo synthesis, is the dietary uptake in the form of high or low-density lipoprotein particles (HDL, LDL), containing cholesteryl esters [77,82,89]. LDL receptors (LDLR) on the cell surface bind to extracellular LDL particles and initiate endocytosis, followed by ester hydrolysis via acid lipases in late endosomes and lysosomes (LE/Lys). Thereby freed cholesterol is highly insoluble and collects in hydrophobic pockets and internal vesicles in the lysosomal lumen, from where it is shuttled to the limiting membrane by means of the soluble Niemann-Pick type C protein 2 (NPC2) [90–92]. Upon reaching the limiting membrane, cholesterol is handed off to the highly abundant cholesterol binding proteins LAMP1 and LAMP2 (lysosome-associated membrane glycoprotein), which might serve as a reservoir for export [93]. From there, cholesterol is able to travel to the cytosolic face of the membrane, by passing through the hydrophobic tunnels [94] of the transmembrane proteins NPC1 (Figure 4) [95–97] or LIMP-2 (lysosomal integral membrane protein 2) [98,99].

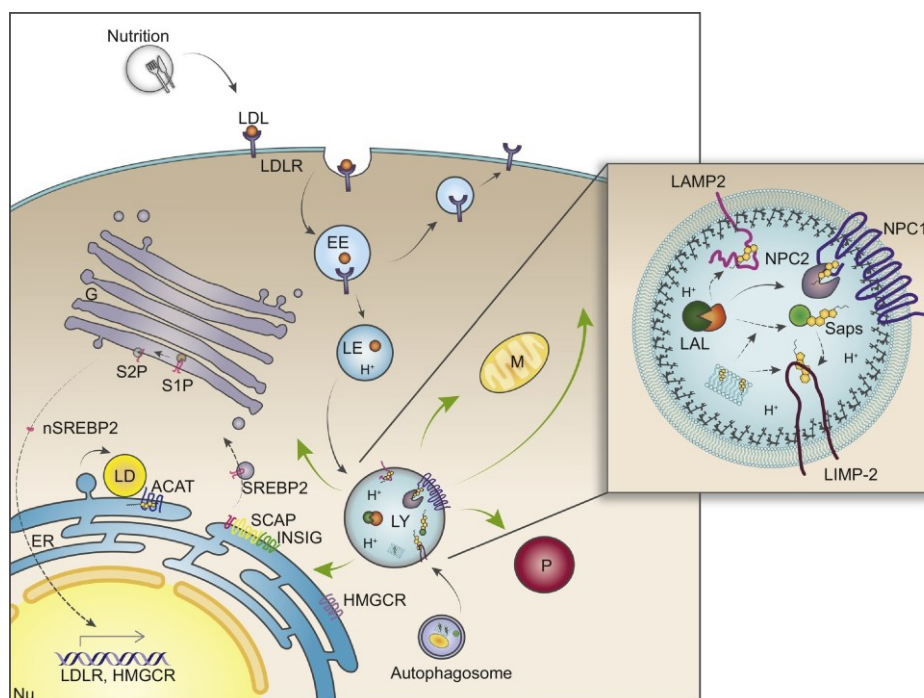


**Figure 4:** Endocytic uptake of LDL-particles rich in cholesteryl-esters is one of the main sources for cellular cholesterol. Cholesterol is released by lysosomal acid lipases (LAL), exported from the lysosomes and distributed throughout the cell. Rising cholesterol levels in the ER deactivate the SREBP pathway through the retention of SCAP at the ER, resulting in decreased expression of key factors in cholesterol uptake (LDLR) and biosynthesis (HMGCR). Graphic by Meng et al [100] used with permission under the license number 5245871243905

The overall relatively low levels of cholesterol in the limiting membrane, indicate that export of liberated cholesterol to other parts of the cell occurs rather rapidly [78,101]. This transport is facilitated by a variety of contact site tethers and lipid transport proteins (Figure 5). Evidence suggests that about 30% of endocytosed cholesterol is directly transferred to the ER [102,103] at membrane contact sites. This efflux is likely facilitated by both ER-anchored proteins such as ORP5 or GRAMD1B [30,104] as well as by endosomal proteins such as ORP1L [8,105] and STARD3 that bind to the ER anchored VAPs.

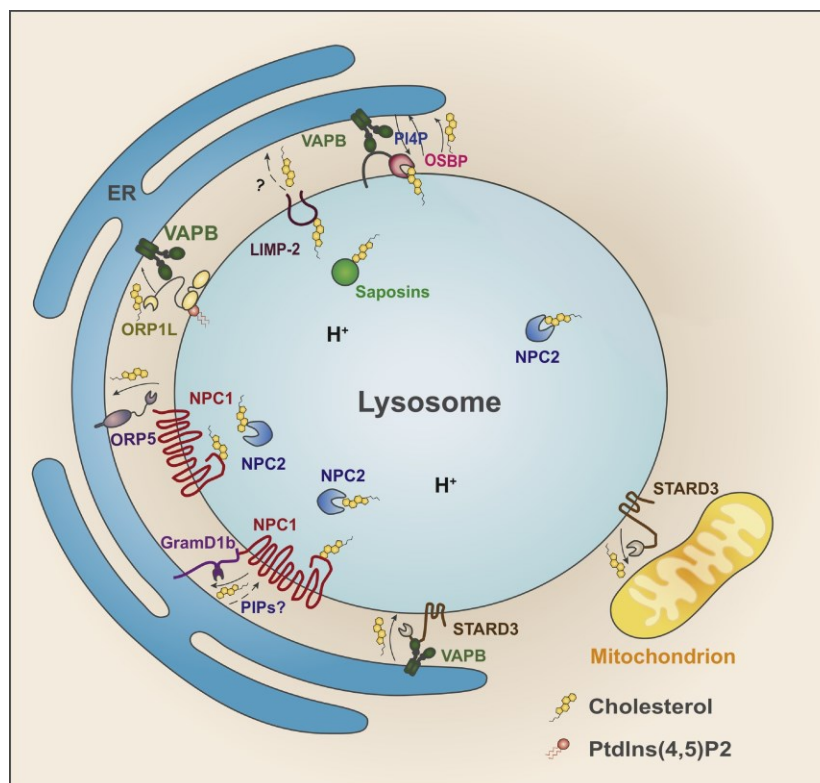


**Figure 5:** Lipid transport and tether proteins involved in cholesterol export from lysosomes to other organelles. Graphic by Meng et al. [100] adapted with permission under the license number 5245871243905

### 1.2.4.1 Sterol transport proteins

Oxysterol binding protein (OSBP)-related proteins, called ORPs (or Osh in yeast) are one of the largest families of lipid binding proteins and are involved in sterol transport throughout the cell [106,107]. Sterol binding in these proteins is mediated via their OSBP-related ligand-binding domain (ORD) and many of them contain an additional pleckstrin homology (PH) domain for binding or sensing of phosphoinositides (PIPs) [108]. ORPs have been shown to carry out multiple functions at different contact sites throughout the cell. The soluble protein OSBP for example localizes to ER-Golgi contact sites and

promotes a counter-exchange of oxysterol and the phosphoinositide PI(4)P [22], while both the lysosomal ORP1L and the ER resident ORP5 localize to ER-LE/Lys contact sites in order to enable export of endosomal cholesterol to the ER [8,104,105]. Export of endosomal cholesterol to mitochondria, however, seems to be mediated primarily by a member of a different family of sterol transporters, the lysosomal StAR-like protein STARD3 [30,109–112].

In this group of proteins, cholesterol-binding is mediated via the so-called steroidogenic acute regulatory protein (StAR)-related lipid transfer domain, or short START [113]. This domain is highly conserved in animals and plants and is found in 15 mammalian proteins, which can be categorized phylogenetically into six sub-families [114]. While all these StAR-like proteins, also called STARD 1-15, contain a START domain, they widely differ in their cellular localization, lipid binding specificity, and overall functionality. The START protein class contains some of the most significant intracellular cholesterol transporters. STARD4 for example is a soluble LTP and has been shown to mediate a large percentage of all non-vesicular cholesterol transfer between multiple different membranes, such as the PM, lysosomes and the ER [115,116].

The late endosomal protein STARD3 (or MLN64), which is anchored to the limiting membrane via a unique cholesterol-binding MENTAL domain [117] was, besides its involvement in cholesterol export to mitochondria, also found to form contact sites with the ER through tethering to VAP-A, VAP-B and MOSPD2 [6,24]. At these contact sites, STARD3 appears to mediate a retrograde transport of cholesterol to lysosomes [118] in order to keep ER cholesterol levels low and to supply endosomes with the amount of cholesterol needed for the formation of intraluminal vesicles [119].

When not bound to the ER, ORP1L and STARD3 are also involved in relocalization of lysosomes to the perinuclear region of the cell, through dynein motor assembly with Rab7a and RILP (Rab interacting lysosomal protein) [9,111]. This microtubule minus-end directed transport is however terminated through contact formation with the ER after binding of ORP1L or STARD3 to VAPs [8,120,121]. Rab7a is thereby freed and able to interact with the ER proteins protrudin [120,122] and PDZD8 [123,124]. This leads to the recruitment of the plus-end directed microtubule motor kinesin-1 and transport of LE/Lys to the cell periphery, where cholesterol is exported to the PM. The transport of LE/Lys towards the plasma membrane was also shown to be dependent on Rab8a and myosin, ending in the vicinity of focal adhesions (FAs) [125]. This process is governed by the focal

adhesion kinase (FAK) and ORP2 which mediates cholesterol-PI(4,5)P<sub>2</sub> exchange between lysosomes and sorting endosomes [126].

While it has become more and more evident that a large portion of lysosomal cholesterol is in fact transported to the plasma membrane first before it is further distributed to other organelles [127–130], it is still not clear to what extent this is steered via any of these Rab-mediated repositioning mechanisms of late endosomes and lysosomes.

### 1.2.5 Lysosomal cholesterol export defects

If any of the processes necessary to digest lipids and export them out of the lysosome is defective, it can lead to their accumulation in the endocytic compartments, which in many cases results in severe diseases, called lipidoses. Most of these lysosomal storage disorders (LSDs), have been attributed to simple loss-of-function mutations in a variety of lysosomal enzymes, including forty different acid hydrolases [131] and proteins involved in lipid transport such as NPC1, NPC2 and LAMP2 [132]. In patients with Niemann-Pick type C disease, which is caused by mutations in NPC1 or NPC2, cholesterol and sphingolipids [133] are heavily accumulated in late endosomes and lysosomes [134–136], leading to a cascade of downstream effects, ultimately ending in neurodegeneration [137]. NPC1 deficient cells were also observed exhibiting greatly extended membrane contact sites between lysosomes and mitochondria. These contact sites are enriched for and dependent on STARD3 [30], suggesting a role as an alternative cholesterol export route. Under NPC-disease conditions, STARD3 might also play a role in VAP-dependent tethering of LE/Lys to the ER, thereby facilitating cholesterol transport along the concentration gradient out of the lysosome [138]. Together with the fact that artificially created ER-LE/Lys contact sites can also partially rescue lysosomal cholesterol accumulation in NPC1 deficient cells [30], this again shows the importance of membrane contact sites in lysosomal cholesterol export [139]. A recently discovered additional factor in this export is the ER-resident protein SNX13, which tethers lysosomes and lipid droplets to the ER [140]. Interestingly, in NPC1-deficient cells it was shown that SNX13 depletion is able to restore cholesterol distribution to the PM, making it a negative regulator of lysosomal cholesterol export.

### 1.2.6 Plasma membrane cholesterol

Cholesterol is most abundant in the plasma membrane, where it forms sphingolipid-rich micro domains, called lipid rafts [62]. Multiple studies showed that not all cellular cholesterol is organized equally. By evaluating its accessibility to different cholesterol binding molecules, cellular cholesterol could be categorized into three distinct pools [127]. The first pool consists of a portion of cholesterol that is highly mobile and selectively depleted earliest when cells are deprived of cholesterol [141]. This distinction could be made since this pool is highly accessible and easily bound by the cholesterol binding probe PFO\*, a variant member of the class of cholesterol dependent cytolysins (CDCs) [77]. The second pool of cholesterol, is present in the form of sphingomyelin-sequestered micro domains, that only becomes accessible to PFO\* after treatment with sphingomyelinase (SMase) or when using a different CDC called Ostreolysin A [142,143]. The remaining pool of cellular cholesterol seems to be essential for cell survival and cannot be depleted or liberated by SMase treatment.

#### 1.2.6.1 Sensing of plasma membrane cholesterol by STARD4

Since the “accessible” cholesterol of the first pool becomes only present when PM-cholesterol levels surpass 30 mol %, it can serve as a readout for overall cholesterol levels. Low total levels of cholesterol result in concentrations below 5 mol % at the ER, which results in SREBP mediated upregulation of cholesterol synthesis and LDL uptake, through increased expression of HMGCR and LDLR, respectively [83]. Interestingly, SREBP activation also causes increased expression of STARD4 [144], which is the only sterol carrier protein regulated by this pathway [83]. STARD4 is a cytosolic box-like sterol transport protein, that was shown to increase cholesterol esterification by ACAT1 when overexpressed [115,145]. In cholesterol depleted cells, STARD4 overexpression was also shown to increase the response time to cholesterol repletion at the plasma membrane, while reduced STARD4 levels caused a desensitization of the SREBP response [116]. These results indicate that STARD4 is most likely involved in cholesterol transport from PM to ER, where it can downregulate its own expression levels, through the cholesterol-induced retention of SCAP. This way STARD4 plays an important role in sterol sensing at the PM and the relaying of that signal to the ER [78].

### 1.2.6.2 GRAM-domain containing proteins in cholesterol sensing and transport

Another mechanism of cholesterol sensing in the plasma membrane involves the high levels of anionic lipids like phosphatidylserine (PS) in the inner leaflet. When the accessible pool of cholesterol in the PM is expanded in response to increased total cholesterol levels, a group of three ER proteins, GRAMD1A-C, (gram domain-containing proteins 1A-C, also called Aster A-C), are able to sense the co-incidence of cholesterol and PS [146,147] via a pleckstrin homology (PH)-like GRAM domain [148,149]. Through this interaction, ER tubules are recruited to the plasma membrane, establishing membrane contact sites, where cholesterol is transported from the PM to the ER [27,146,147,150].

Structural analysis of the GRAM domains of GRAMD1B and its yeast orthologues Ltc1/Lam6 revealed the molecular basis [147,151,152] for the change in lipid specificity away from the PH-domain typical binding of phosphoinositide phosphates (PIPs), towards the sensing of PS-rich membranes that are also enriched with cholesterol. Herein it was also shown that the cholesterol binding StART-like domain of GRAMD1B is able to transport PI(4,5)P<sub>2</sub> as well, which suggests a potential function in PIP-cholesterol counter-exchange similar to OSBP [22].

Sensing of cholesterol levels in the PM by GRAMD1B impacts on contact site formation and cholesterol import to the ER, but also effects the expression levels of GRAMD1B. Upregulation of GRAMD1B levels was observed after synthetic stimulation of the liver X receptor (LXR), which is naturally activated through SREBP processing or after cytosolic accumulation of cholesterol and cholesterol-derived oxysterols [150,153]. Since elevated levels of free cholesterol have also been observed as a result of GRAMD1B depletion [30], this indicates an indirect self-regulation similar to STARD4.

Additionally, the mammalian GRAMD1B and its yeast orthologues were also shown to form contacts between the ER and other intracellular organelles [28,30,70,154–156]. At mitochondria, Ltc1/Lam6 was shown to locate to [28] or even expand [156] these contact sites and GRAMD1B was shown to be necessary for sufficient supply of cholesterol to the organelle [155]. Additionally, a predicted mitochondrial targeting sequence was identified in GRAMD1B that proved essential for cholesterol delivery to mitochondria, strongly supporting a role of GRAMD1B in ER-mitochondria contact site tethering. Whether GRAMD1B itself is transferring cholesterol molecules at these MCS is however still unclear.

Equally uncertain is the involvement in contacts of the ER with the endocytic organelles. As with mitochondria, yeast Ltc1/Lam6 locates to and expands contact sites of the ER with the vacuole [28,156] and seems to be necessary for cholesterol transport to the contacting organelle [154]. In human cells, GRAMD1B was also shown to be involved in contact site formation with lysosomes, where it interacts with the lysosomal cholesterol exporter NPC1 [30]. Depletion of GRAMD1B resulted in less NPC1 localization to ER-LE/Lys contact sites and less MCS formation between the two organelles overall, indicating a tethering function of the two proteins. Through the determination of cholesterol-esters levels, it also became apparent that if either of the two proteins was depleted, less cholesterol would be transported to the ER. However it has not been resolved yet, whether the reason for this effect is the loss of NPC1-GRAMD1B interaction and therefor loss of non-vesicular transport at membrane contact sites or whether it is simply caused by the loss of one of two individual functions that are both needed in cholesterol homeostasis. These open questions prompted me to investigate the extent to which GRAMD1B-mediated direct transport at contact sites contributes to cholesterol export from lysosomes. To be able to make these kinds of differentiations, a new set of molecular tools is needed.

### 1.3 Multifunctional lipid probes

In the last decades, our understanding of intracellular cholesterol distribution and transport has widened immensely. These advancements are largely thanks to the development of a multitude of novel tools, that allow us to trace, visualize and quantify cholesterol in living cells (reviewed in [77]). A large set of those tools consists of functionalized cholesterol analogs that can be taken up by cells and are often naturally metabolized. While fluorescently tagged cholesterol analogs have proven useful in many studies, it has become more and more apparent that, due to their bulky fluorophore, they are often mislocalized in living cells (e.g. even unesterified BODIPY cholesterol can be found in lipid droplets) [157–161]. Fluorophores were also reported to affect the binding and transport capabilities of sterol transfer proteins, such as STARD4 [162]. Radiolabeled sterol analogs on the other hand behave exactly like their endogenous equivalent, but are far less flexible in their use, since they allow no real-time detection, no option to combine the readout with other methods and only very limited in-cell imaging [77,163].

An approach that tries to combine the strengths of both these methods relies on the modification of lipid derivatives with small chemical moieties, called click-handles, that allow the lipid to be further functionalized using click chemistry [164–166]. Clickable cholesterol derivatives were shown to be taken up by living cells and successively metabolized to cholesterol esters [167] in a manner comparable to endogenous cholesterol. By attaching a fluorophore to the click-handle after cell fixation, their natural distribution throughout the cell could also be visualized [168,169].

In order to study transient lipid-protein interactions that are too weak for co-purification assays, analogs that carry a photoactivatable diazirine were developed, which allows covalent crosslinking of the two molecules via UV irradiation [97,107,170–172]. Combining these two approaches in one molecule, Hulce et al. created a bifunctional cholesterol derivative, which allowed them to crosslink and selectively purify all proteins interacting with their cholesterol in cells [167]. The toolset of these photoactivatable and clickable (pac) cholesterol probes has since been expanded [173–175] and successfully applied in multiple studies [176,177]. The ability to crosslink clickable lipids in cells to their interacting proteins also stabilizes their subcellular localization, resulting in faithful visualization of the lipids when combining it with immunofluorescence imaging [30]. Given the range of chemical moieties that can be attached via commercially available click compounds, these bifunctional pac-lipids have proven to be highly flexible and can be

combined with most biochemical assays. Pulse-chase experiments in which pac-cholesterol was administered to NPC1-deficient cells for example, were able to demonstrate delayed esterification of the probe, which was visualized in thin layer chromatography after attaching a fluorophore to the click handle in line with known lysosomal cholesterol export deficiency for this disease model.

### 1.3.1 Organelle targeted caged cholesterol

The advantage of minimally-modified lipid probes, i.e. the comparable metabolism, can also present as a challenge to the experimental setup. Especially with highly bioactive signaling lipids such as sphingosine, this leads to a rapid conversion or degradation of the functionalized lipid. In order to circumvent this issue, trifunctional lipid probes have been developed [178], which additionally include a photocleavable molecular group (“cage”) that renders the lipid biologically inactive until removed by a UV flash. This way it is possible to release a larger quantity of bioactive lipid in a temporally and spatially controlled manner [179] and track its distribution in pulse chase experiments [178]. However, since the distribution of caged lipid probes before release is somewhat arbitrary throughout the whole cell, efforts have been made to create organelle-targeted caged lipids that allow for a site specific release of active lipids [180,181]. Improving upon these advancements, Janathan Altuzar has recently successfully developed organelle targeted trifunctional lipid probes [182], including a trifunctional caged pac-cholesterol that pre-localizes to the lysosomal lumen (Lyso-pacChol, Figure 6). Simply adding this probe to the cells’ growth medium and allowing enough time for uptake and pre-localization, results in cells with Lyso-pacChol-laden lysosomes. After a short UV pulse to uncage the probe, the cholesterol transport machinery of the cell is exposed to biologically active bifunctional pac-cholesterol, which enables for a variety of assays.

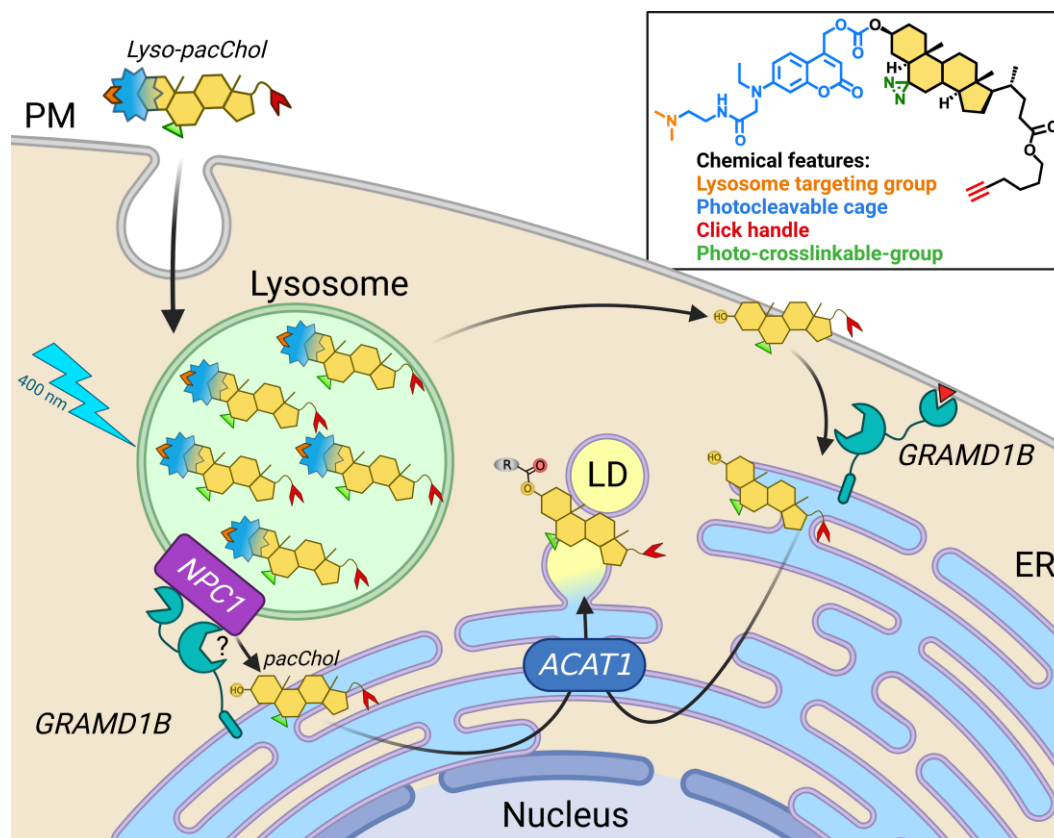


**Figure 6:** Uptake, transport and metabolism of Lyso-pacCholesterol – Lysosome targeted caged cholesterol is endocytosed by cells and accumulates in the acidic lumen of lysosomes due to the positively charged tertiary amine. UV irradiation at 400 nm cleaves off the coumarin cage group and releases biologically active pacCholesterol, which is transported and metabolized similarly as endogenous cholesterol. The uncaged probe is ultimately esterified by ACAT1 at the ER after being transported there directly or with a detour through the plasma membrane. Import to the ER from the plasma membrane is mediated by GRAMD1B, which might also facilitate direct transport from lysosomes in concert with NPC1. Created with Biorender.com. Depiction of chemical structure adapted from Altuzar et al. [182] with permission under CC BY-NC 4.0



## 2 Aim of this thesis

Studying the roles of contact sites between different organelles in detail is still a difficult task. Previous studies on their composition have largely focused on contacts between the endoplasmic reticulum and mitochondria and were often based on the purification of the interfacing membrane regions followed by mass spectrometric identification, which resulted in high amounts of unspecific hits. While the specificity of mass spectrometric identification could be greatly improved using biotin-based proximity labelling assays targeted to the membranes of interest, early studies applying this tactic simply relied on the cross-referencing of separate datasets from both organelles.

By using a split version of a bacterial biotin ligase, termed Split-BioID [51], and well-characterized tether protein pairs, this work aims to identify proteins located at specific contact sites of the ER with multiple other organelles.

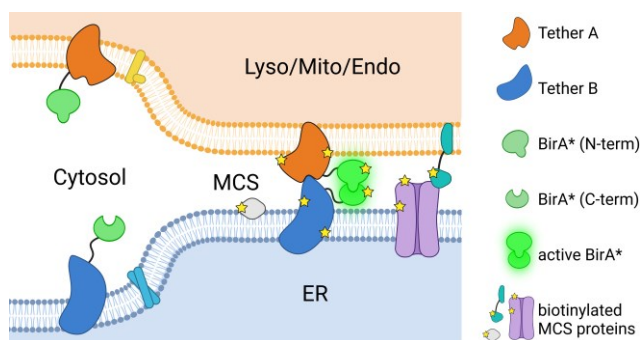


**Figure 7:** Split-BioID at membrane contact sites

Compared to other assays that use general organelle-targeting anchors, this use of specific tether proteins as baits might also offer insights into the reason behind the seemingly redundant creation of contacts between the same organelles. The main goal of this work is to establish and validate the applicability and robustness of such an approach and to further investigate the functionality of selected proteins that were identified by the proteomic screens.

Here a special focus will be put on proteins involved in cholesterol transport processes between lysosomes and the ER. To this end, I will investigate the impact of the ER-resident cholesterol transporter GRAMD1B on these processes. Curiously, this protein is well-characterized to act at ER-plasma membrane contacts, but was also shown to directly interact with the lysosomal protein NPC1. As such, studying this potential dual role at different contact sites, will further strengthen our understanding of subcellular cholesterol trafficking and might provide a basis for the development of treatment options of diseases caused by lysosomal accumulation of cholesterol.

## 3 Results and Discussion

### 3.1 Split-BioID at membrane contact sites

In order to identify proteins involved in creating and maintaining contact sites of the ER with other organelles and to eventually decipher the function of some proteins acting at these contacts, I decided to apply the Split-BioID technique to these MCS. For this I planned to identify proteins acting at ER-lysosome, ER-mitochondria as well as ER-endosome contact sites.

#### 3.1.1 Designing and testing Split-BioID bait pairs

Contact sites between two organelles can be created by multiple different tether pairs, which can result in MCS with distinct purposes and compositions. In order to be able to analyze the composition of a specific kind of MCS, I chose to use known MCS tether pairs as bait proteins instead of adding different organellar targeting sequences to the BirA\* fragments as used in previous studies [41,42,53]. For contact sites between late endosomes and the ER I decided to use STARD3 and VAP-A as bait proteins, since their interaction and function had been well described [6,118,183]. Since binding of the two proteins was shown to be unaffected by N-terminal GFP-tagging of VAP-A and C-terminal mCherry-tagging of STARD3 [6], I decided to initially test these orientations for designing the Split-BioID fusion constructs. In order to minimize the effect a bulky protein tag might have on the location of the bait proteins, I used the smaller C-terminal part of the split BirA\* (CBirA\*) for the smaller of the two bait proteins (VAP-A) (Figure 8).

In order to identify a potentially different protein composition of ER contact sites with other populations of endosomal vesicles, I decided to use the epidermal growth factor receptor (EGFR), residing in earlier endosomes and the ER-resident protein tyrosine phosphatase 1 (PTP1B) as a second set of bait proteins. It was shown that after EGF stimulation and endocytosis of the EGFR-EGF complex, EGFR is dephosphorylated by PTP1B at contact sites with the ER. This step is necessary for receptor sorting in intraluminal vesicles (ILV) and the subsequent degradation of EGFR and its ligand [56]. I designed the Split-BioID constructs in a way that the BirA\* fragments faced the cytosol, meaning N-terminal linking to PTP1B and C-terminal linking to EGFR, while again attaching the smaller CBirA\* to the smaller of the two bait proteins (PTP1B).

### 3 Results and Discussion - 3.1 Split-BioID at membrane contact sites

As a third MCS of interest I chose contacts between the ER and mitochondria, that rely on the interaction of VAP-B with the mitochondrial protein RMD3 (or PTPIP51) [184–186]. Interfacing membranes of the ER and mitochondria (also called mitochondria associated membranes, short MAMs) have been studied extensively and multiple independent tethering complexes have been identified [187]. Interaction of VAP-B and RMD3 was shown to be necessary for calcium influx into mitochondria, although neither of them is known to have a role in  $\text{Ca}^{2+}$  binding. Therefore, they likely promote contact sites that are distinct from MAMs formed by other tether pairs. Again, I designed the Split-BioID constructs such that the BirA\* fragments faced the cytosol and the smaller BirA\* fragment is linked to the smaller bait (N-terminal fusion of CBirA\* to VAP-B and C-terminal fusion of NBirA\* to RMD3).



**Figure 8:** Split-BioID constructs - Known tether protein pairs from three different membrane contact sites were cloned under a bidirectional tetracycline-controlled promoter as fusion proteins with inactive fragments of the promiscuous *E. coli* biotin ligase BirA\* (CBirA\* and NBirA\*). The shown orientation was chosen to target cytosolic localization of the BirA\* fragments and to minimize their effects on the tethers.

After cloning the Split-BioID constructs under a tetracycline-inducible promoter I transiently transfected them into a compatible HeLa cell line (11ht) [188] to test their biotinylation efficiency. As a positive control I used a Split-BioID construct created in the Béthune laboratory [51] that is comprised of the proteins FRB and FKBP as baits, which can form a strong heterodimer upon addition of rapamycin. A dish of mock transfected cells served as a negative control. Doxycycline was added to all cells to induce expression of the constructs, together with biotin and rapamycin for the positive control. To test whether the designed constructs are able to reassemble into an active form, cell lysates were subjected to immunoblot analysis using a streptavidin-reporter. The resulting western blot (Figure 9) showed for all designed tether pairs similar levels of protein biotinylation as the rapamycin-induced construct, indicating the ability to successfully reassemble, forming functional BirA\* protein *in vivo*. Protein bands that showed the highest level of biotinylation (marked by arrows) correspond to the bait constructs. In addition, the pattern of biotinylated products in each condition differed, indicating that

### 3 Results and Discussion - 3.1 Split-BioID at membrane contact sites

distinct subsets of proteins were present in the biotinylation radius. In contrast, only targets of the endogenous mammalian biotin ligases could be identified in the negative control of mock transfected cells. Together, this showed that the chosen orientation of the split BirA\* fragments with respect to the bait proteins permitted their reassembly and that the chosen combination of bait proteins marked distinct subsets of MCS-resident proteins.

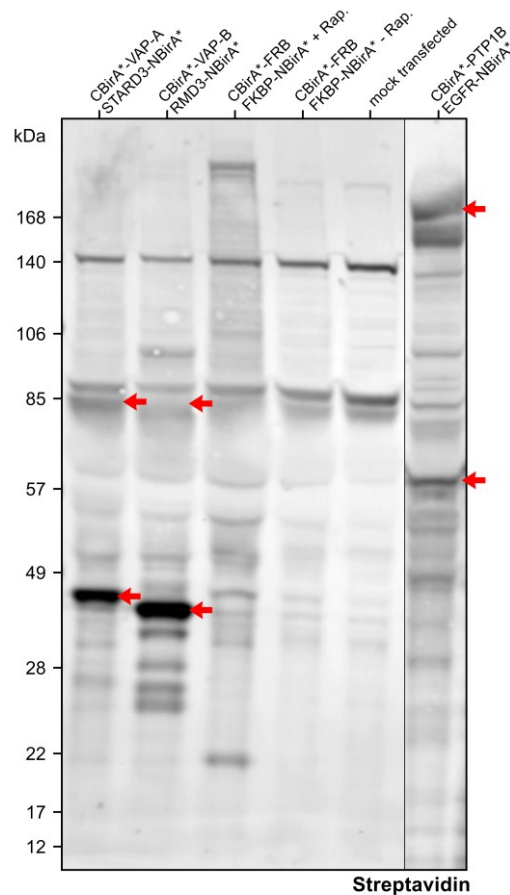


**Figure 9:** Initial test of biotinylation activity - Cloned Split-BioID constructs were transfected into HeLa 11ht cells and after 1 day expression was induced by the addition of 100 ng/ml doxycycline. After incubation with 50  $\mu$ M biotin for 24 hours, cells were harvested and subjected to immunoblotting analysis using fluorescent streptavidin as a reporter for protein biotinylation. Bands corresponding to the self-biotinylated bait proteins are marked with arrows. A split-BioID construct of the rapamycin-inducible heterodimer FRB/FKBP was used as a positive control. Each constructs shows a unique pattern of biotinylated proteins, indicating specific biotinylation that is dependent on bait location and interaction.

#### 3.1.2 Proteomic analysis of targets of Split-BioID at MCS

Next, I was curious to identify the targets of the Split-BioID assay by using protein mass spectrometry. For enrichment of the biotinylated targets, I repeated the assay on a larger scale and loaded the total cell lysates from each of the Split-BioID constructs (from here on called Lyso-ER, Mito-ER and Endo-ER) on streptavidin covered magnetic beads. Successful binding of biotinylated proteins to the beads is demonstrated by the overall loss of streptavidin signal (red signal in Figure 10) between “Input” and “Flowthrough” fractions. This effect is particularly visible at the FLAG-positive bands (Figure 10, arrows) of the CBirA\*-tagged bait proteins. To avoid the use of non-ionic detergents that could interfere with liquid chromatography, I eluted the bound proteins from the beads under relatively mild conditions, using excess biotin at boiling temperatures.

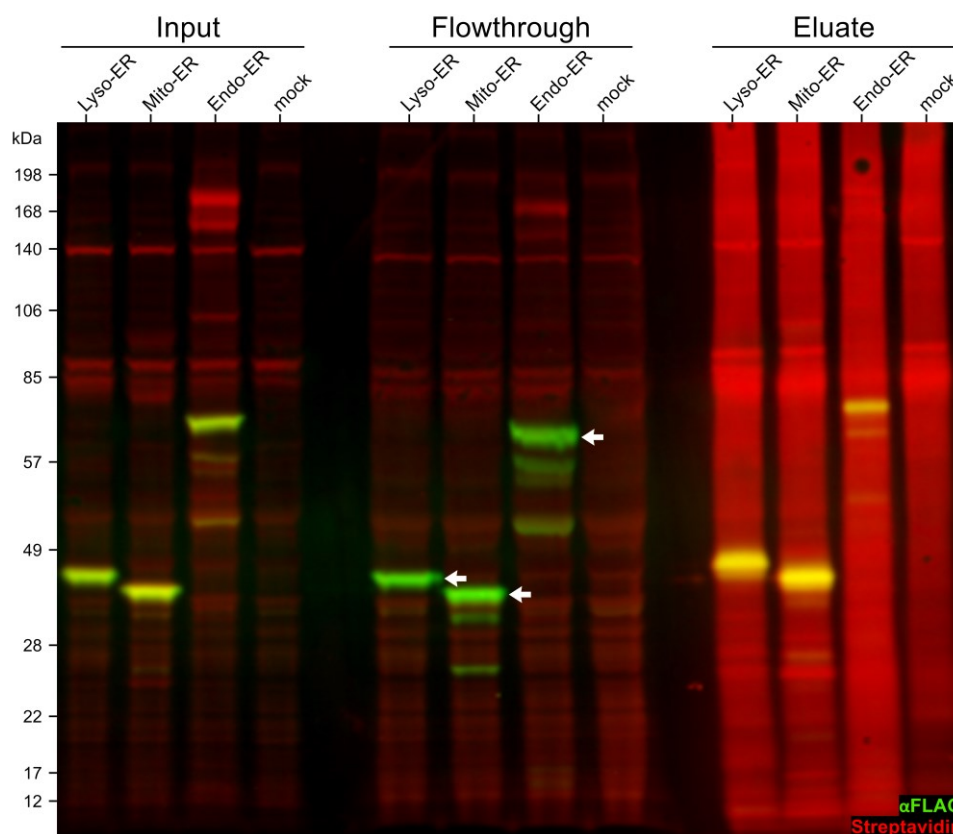


**Figure 10:** Streptavidin pulldown of biotinylated proteins – Cell lysates containing proteins that were biotinylated by the Split-BioID pairs targeted at membrane contact sites were incubated overnight with streptavidin coated magnetic beads. The supernatant was removed and the beads washed, before any bound proteins were eluted using excess biotin, reducing agents and heat. For western blot analysis ~1% of the used lysate and an equal amount of the supernatant were loaded as “Input” and “Flowthrough”. Bait proteins tagged with CBirA\* (VAP-A, VAP-B and PTP1B) were visualized using a FLAG antibody. Loss of streptavidin signal in these bands in the flowthrough (arrows) indicates selective pulldown of only biotinylated proteins.

Eluted proteins were then sent to the Mass Spectrometry (MS) Facility of Fingerprint Proteomics at the University of Dundee for analysis. As a technical replicate the whole process was repeated separately. I then analyzed the raw proteomic result files using the MaxQuant software and the in-built Andromeda peptide search engine to perform label-free quantification (LFQ) of the identified proteins. For the statistical analysis, I used the Perseus framework and included a control dataset of four different BioID assays measured at the same facility, which was kindly provided by Julien Béthune. This dataset was created by using proteins from the trans- and cis-Golgi (TGN38 and GRASP65), as well as a cytosolic protein (Ago2) as baits in conventional non-split BioID assays. By treating these results like a set of replicates in the analysis I simulated an inconsistent and unspecific biotinylation pattern. In order to identify proteins that are consistently enriched compared to the control dataset, I visualized the identified proteins in volcano plots (Figure 11) and performed a two-sample t-test based on permutation-based FDR statistics. The resulting list of significantly enriched proteins was then further filtered for hits that were also at least two-fold enriched in both replicates, compared to the negative control that did not express any BioID constructs. The resulting list of 63 proteins are shown in Table 2. The average enrichment of these hits over the negative control ranged from ~25-fold in the Endo-ER samples up to ~72-fold in Lyso-ER (Table 3). Looking at the consistency between the two replicates I found the determined quantitative values of the protein hits to differ on average around 2-fold.

Analysis of the identified proteins using gene ontology (GO) identifiers showed 87% of them to be associated with cellular membranes, 60% with the endoplasmic reticulum, 30% with any processes involving lipids and 16% with sterols. Comparison of this dataset with four other proximity labelling assays performed at membrane contact sites [41,42,52,53] (see chapter 1.1.3.1) revealed that 25 of the identified proteins were found in at least one of the other screens as well. When compared to my list of proteins, GO-term analysis of the combined results of these four screens showed that their percentage of proteins associated with sterols, lipids or transport processes in general was about 1.5-2 fold lower.

This difference could be due to the fact that I decided to use functional interacting tether pairs as bait proteins. Instead, the other screens targeted the respective membranes individually [41,42,52,53] or cross-referenced the results of separate experiments [41,42]. Potentially, this might have led to a higher rate of biotinylation at actual contact sites in my screens and less at events of random encounters of the two organelles.

### 3 Results and Discussion - 3.1 Split-BioID at membrane contact sites

These four published assays were all performed exclusively at contacts of the ER with mitochondria and their list of proteins overlapped with the 32 proteins I could identify at the same contact site by only 5-7 proteins each, which corresponds to ~16-22%. Comparing the results of these four screens amongst each other, I found overlaps to also range only between 3% and 30%, showing that a high variance between independently performed assays seems to be a common issue. The organelle specificity of my Split-BioID and all the other assays seems to be similar as well, with ~25-30% of the identified proteins being somehow connected to functions at mitochondria, according to the GO-term analysis. Some of the proteins that I identified in the Mito-ER sample in my screen (DDRGG1, EXD2, PTP1B, STIM1, VAPA and VAPB) were also found in two or even three of the other four screens, resulting in a high confidence for these hits.

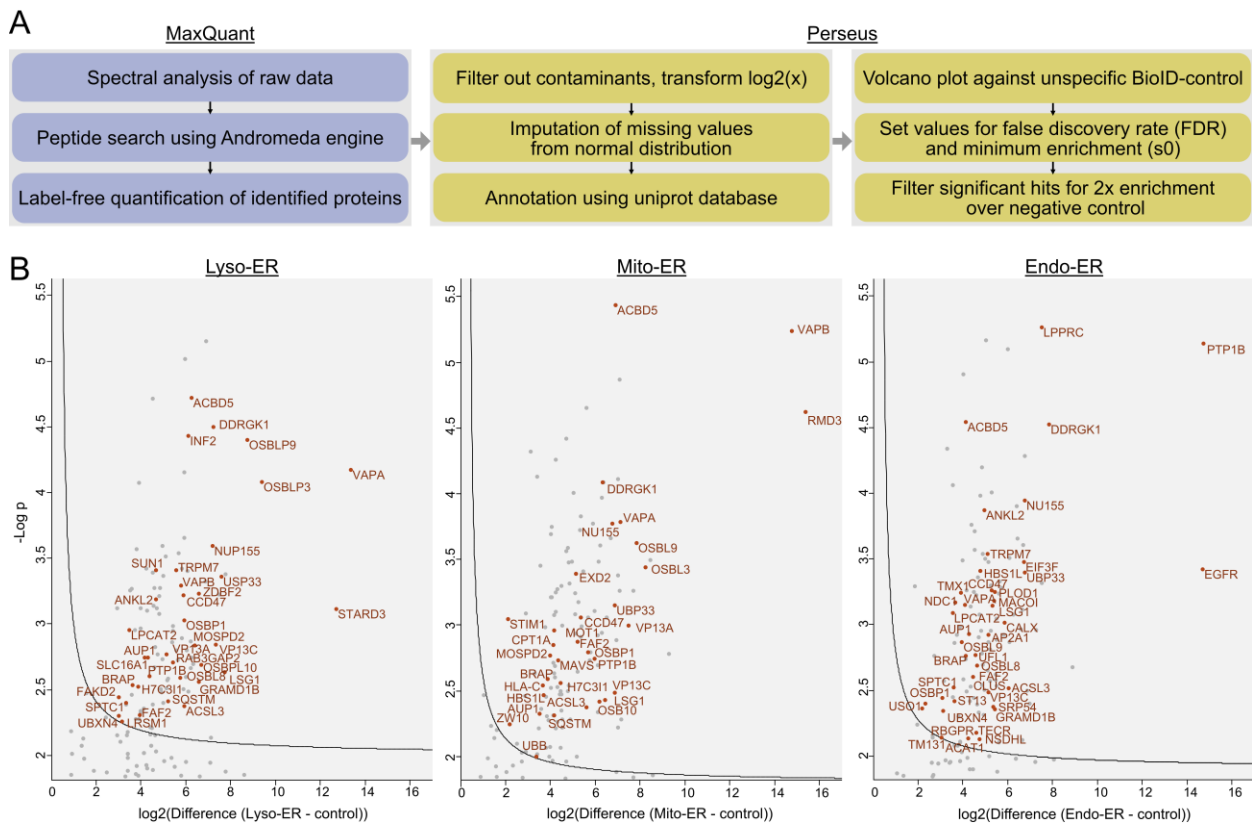


**Figure 11:** Analysis of LC-MS/MS results – Proteins biotinylated in a Split-BioID assay from transiently transfected cells were enriched in a streptavidin pulldown and sent for proteomic analysis at Fingerprint Proteomics at the University of Dundee (A) Raw data of the mass spectrometric measurements were first analyzed in MaxQuant v1.6.1. Identified peptides were annotated using Andromeda search engine and quantified using the label-free quantification method. In Perseus v1.6.1 the resulting list of proteins was filtered using a list of common contaminants. For proteins that were not identified in all of the samples, the missing values were imputed using random values from a normal distribution. For statistical analysis LFQ-values were tested against a dataset stemming from an unspecific BioID screen using permutation-based FDR statistics (two-sample t-test, 250 permutations; FDR=0.05;  $s_0=0.1$ ). Protein enrichment over the control sample was plotted against each corresponding p-value, resulting in a volcano plot (B). A sensible threshold was selected by adjusting the FDR and  $s_0$  values and all hits above it were considered significant. Hits that were not found at least 2-fold enriched over the negative control in all replicates were filtered out, resulting in the final set of proteins labelled in red.

### 3 Results and Discussion - 3.1 Split-BioID at membrane contact sites

All of these proteins, except EXD2, are known to localize to the ER-membrane, where they are involved in organellar tethering (VAPs, PTP1B), ion transport at contact sites (STIM1) [4] or act as a sensor for ER-stress (DDRGK1) [189]. EXD2 is an exonuclease, that has been shown to be involved in DNA repair but is paradoxically located in the mitochondrial outer membrane [190]. The results of these initial experiments suggest a great potential in using split proximity labeling assays for the study of membrane contact site composition. The presence of so many known MCS proteins among these results was quite promising and inspired confidence into my approach.

Further investigations, however, particularly immunofluorescence microscopy (IFM) analysis of transfected cells revealed that transfection efficiency under the used conditions was only about 10%. Therefore, in order to yield enough expression of the Split-BioID constructs I had used relatively high doxycycline concentrations of 100 ng/ml. This resulted in clustering of both the bait proteins themselves, as well as, in consequence, the biotinylation pattern in the expressing cells (Figure 12). These data cast some doubt on the physiological consequences of my approach and the resulting protein hit list.

**Table 2:** List of significant hits resulting from a proteomic screen of targets biotinylated by Split-BioID at membrane contact sites in transiently transfected cells, sorted by the samples they were identified in.

Lyso-ER	Mito-ER	Endo-ER	Lyso-ER + Mito-ER	Lyso-ER + Endo-ER	Mito-ER + Endo-ER	All three
FASTKD2	CPT1A	AP2A1	MOSPD2	ANKLE2	HBS1L	ACBD5
INF2	EXD2	CANX	OSBPL10	GRAMD1B		ACSL3
LRSAM1	HLA-C	CLU	OSBPL3	LPCAT2		AUP1
STARD3	MAVS	EGFR	SLC16A1	OSBPL8		BRAP
SUN1	RMD3	EIF3F	SQSTM1	RAB3GAP2		CCDC47
ZDBF2	STIM1	LRPPRC	VAPB	SPTLC1		DDRGK1
	UBB	MACO1	VPS13A	TRPM7		FAF2
	ZW10	NDC1		UBXN4		LSG1
		NSDHL				NUP155
		PLOD1				OSBP
		SOAT1				OSBPL9
		SRP54				PTP1B
		TECR				ST13
		TMEM131				USP33
		TMX1				VAPA
		UFL1				VPS13C
		USO1				

### 3 Results and Discussion - 3.1 Split-BioID at membrane contact sites

**Table 3:** Evaluation of the results of the first proteomic screen – 1) Average LFQ enrichment of all significant hits in the Split-BioID samples compared to the unspecific BioID control. 2) Average difference between the LFQ values in the two replicates of all significant hits.

Sample	1) Mean fold-difference of hits over control ( $\pm$ SE)	2) Mean fold-difference of hits between replicates ( $\pm$ SE)
Lyso-ER	72.3x ( $\pm$ 3.3)	2.4x ( $\pm$ 0.04)
Mito-ER	52.3x ( $\pm$ 2.2)	2.5x ( $\pm$ 0.05)
Endo-ER	25.5x ( $\pm$ 1.5)	1.5x ( $\pm$ 0.01)

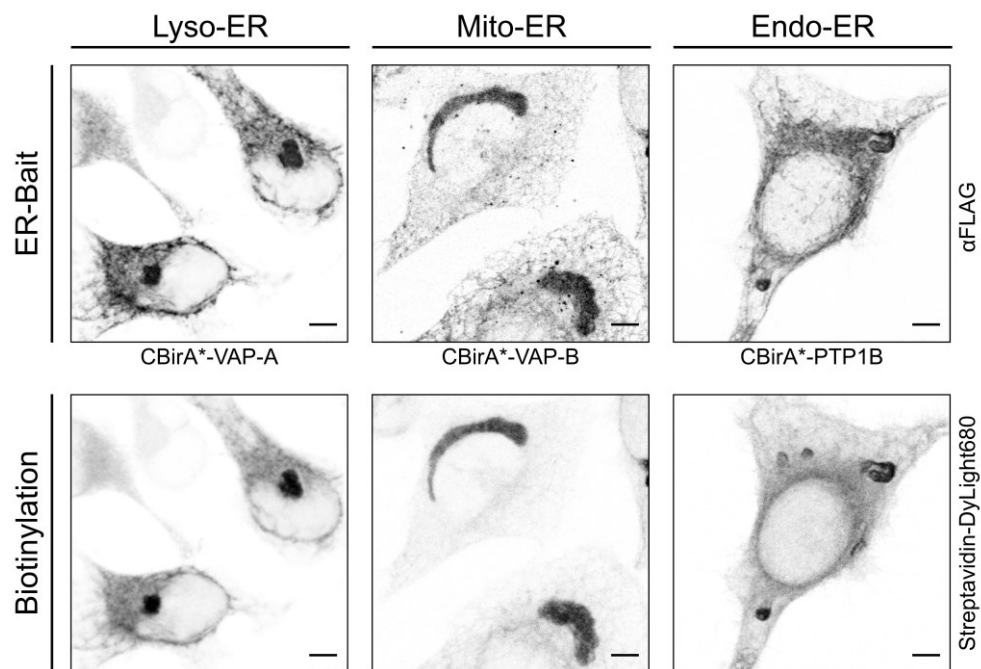


**Figure 12:** Immunofluorescence imaging of Split-BioID cells – HeLa 11ht cells were transfected with the Split-BioID constructs and after 1 day expression was induced with 100 ng/ml doxycycline. After allowing expression for 24h in the presence of 50  $\mu$ M biotin, cells were fixed using paraformaldehyde. Localization of the ER-resident bait proteins (VAP-A, VAP-B, PTP1B) was visualized using an  $\alpha$ FLAG antibody. Biotinylation was visualized using fluorescently labelled streptavidin. At these concentrations of doxycycline, most positively transfected cells showed strong aggregation of the bait proteins in unnatural looking structures that colocalize with the streptavidin signal. This indicates positive reassembly of the inactive BirA\* fragments and therefore artificial formation of contact sites by the bait proteins. Scale bar = 5  $\mu$ m.

#### 3.1.3 Correcting the localization of Split-BioID baits by stable expression

Since transient overexpression of tether proteins led to an unphysiological extension of contact sites, and since the majority of cells was not transfected, I decided to circumvent transfection issues by creating stable cell lines. This could be easily achieved using the Flp-recombinase based integration sites in the genome of HeLa 11ht cells [188] and the pSF3 expression vector. Selection for cells with successful flip recombination was enabled through the genomically integrated hygromycin/thymidine-kinase cassette of the cell line and accomplished by the addition of ganciclovir. As additional control constructs I also cloned all six bait proteins as conventional BioID fusion proteins and included them in the generation of stable cell lines (Figure 13).

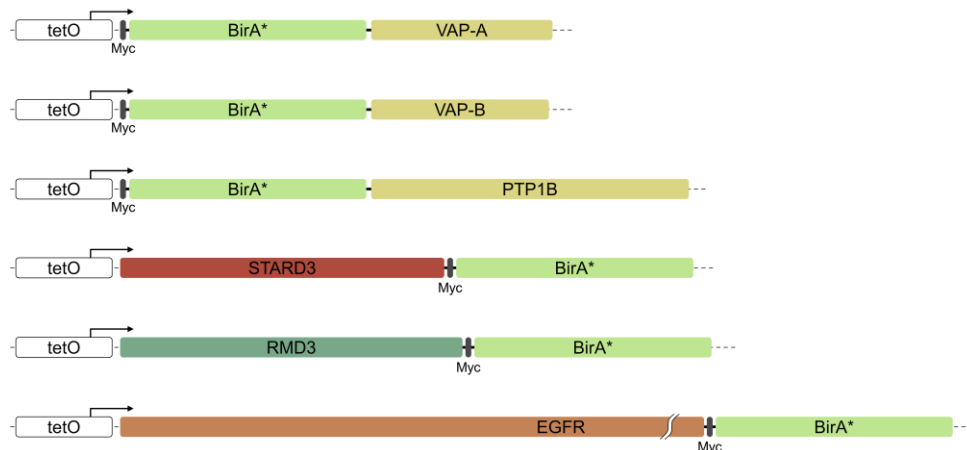


**Figure 13:** nonSplit-BioID constructs – All six previously used bait proteins were also cloned individually as nonSplit-BioID constructs under the same promoter to serve as a control for the biotinylation specificity of the split-BioID pairs.

The finished cell lines were first tested for homogenous expression of the Split-BioID constructs using immunofluorescence microscopy and then suitable expression levels were determined by titration with doxycycline. I then performed biotinylation assays as before using these new cell lines and the optimized doxycycline concentration of 25 ng/ml. I tested the biotinylation efficiency and specificity by immunoblotting, which revealed successful biotinylation and distinct band patterns for each construct (Figure 14). As expected, I could also observe a much stronger overall biotinylation by the conventional non-split BioID constructs.

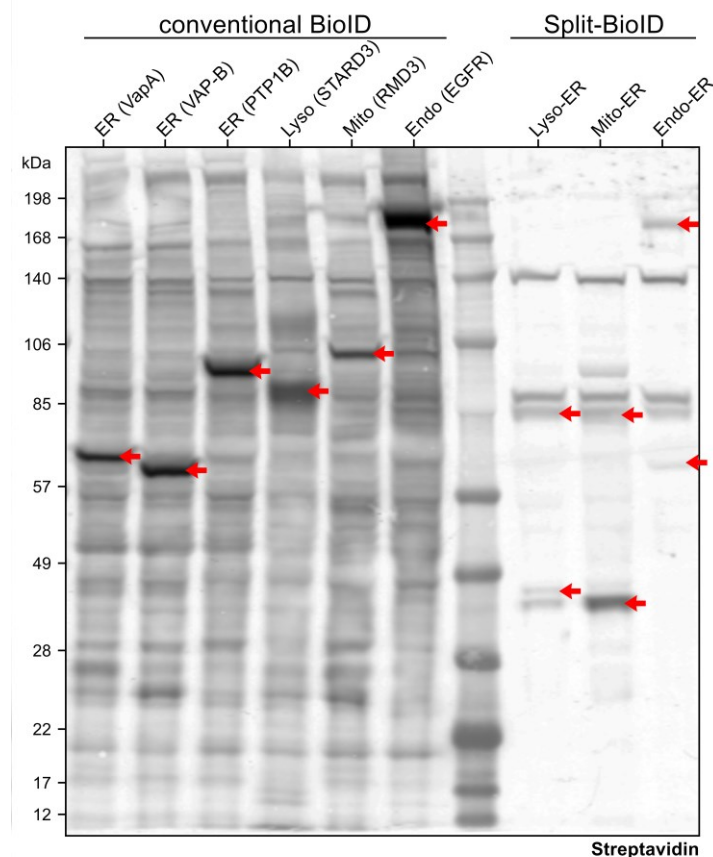


**Figure 14:** Biotinylation activity of stable BioID cell lines – All Split- and nonSplit-BioID constructs were stably integrated into the genome of HeLa 11ht cells using Flp-based recombination. The resulting cell lines were induced with 25 ng/ml doxycycline and incubated for 24 hours with 50  $\mu$ M biotin to allow expression and biotinylation. Cell lysates were subjected to western blot analysis using the same amounts of total protein for each sample. Visualization using streptavidin shows higher overall biotinylation levels and also a higher number of biotinylation targets in the cell lines expressing the conventional (nonSplit) BioID constructs. Bands marked by arrows represent the self-biotinylated bait proteins.

Using confocal IF microscopy at high resolutions and Airyscan image processing, I then further analyzed the intracellular distribution of the biotinylated proteins. When using the conventional BioID setup with only a single bait protein, the biotin signal can be easily attributed to the corresponding organelle (Figure 15, top two rows) where it is evenly distributed. In case of the Split-BioID constructs however (Figure 15, bottom row), the signal was located to distinct spots, that cannot be attributed to either of the two involved organelles alone, indicative of selective biotinylation at MCS. In summary, these experiments showed that the artificial aggregation of overexpressed Split-BioID constructs can be overcome by using stable cell lines and lowering the levels of expression. A comparison with corresponding non-split BioID constructs revealed a less efficient but more specific biotinylation of proximal proteins.

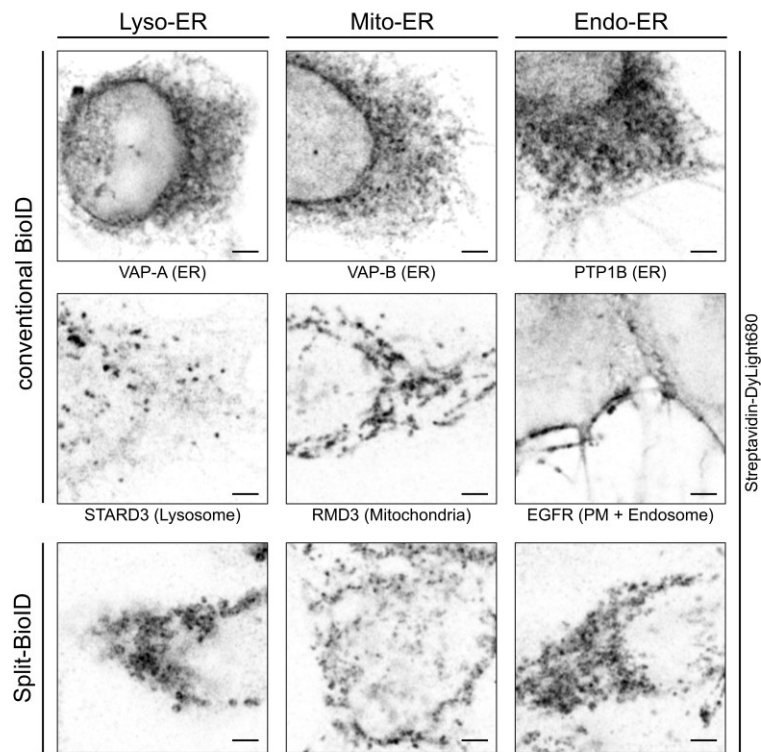


**Figure 15:** Immunofluorescence imaging of stable cell line biotinylation patterns – Stable cells expressing the conventional (non-split) and the Split-BioID constructs were induced with 25 ng/ml doxycycline and incubated with 50  $\mu$ M biotin for 24 hours to allow biotinylation before being fixed with paraformaldehyde. The proteins that were biotinylated by the BioID constructs were visualized using fluorescently labelled streptavidin. The signal pattern in cells expressing the conventional BioID constructs did mostly reflect the shape and localization of the corresponding organelles (in brackets). In Split-BioID cells the signal could not be attributed to either one of the involved organelles alone and was distributed more spot-like, suggesting more specific biotinylation at contact sites. Scale bar = 5  $\mu$ m.

#### 3.1.4 Split-BioID in stable cells produces a different list of proteins

Using the validated stable cell lines with optimized expression levels, I repeated the biotinylation assays and streptavidin-based purification for further mass spectroscopic analysis. Due to a discontinuation of the used magnetic beads by the manufacturer, I had to switch to a different brand of streptavidin beads, which required further optimization of the purification protocol. In addition, the initially used MS-facility stopped accepting external clients, such that I had to also use a different proteomics facility. The previously used control BioID dataset was acquired at the initial facility and was therefore not considered suitable for the new screen, such that I decided to add an additional control, a stable cell line expressing Ago2-BirA\* (kindly provided by Julien Béthune), in the following assays. This cytosolic protein was already included as bait in the initially used control dataset and should allow to filter for unspecifically biotinylated proteins. In this new screen, data analysis and statistical evaluation was performed the same way as before and resulted in the protein list presented in (Figure 16) and (Table 4).

Here, GO-term analysis showed that of the 55 identified proteins, 71% were found associated with membranes, 34% with the endoplasmic reticulum, 14% with lipids and 11% with sterols. The overlap of these results with first MS analysis was quite small (5 hits).

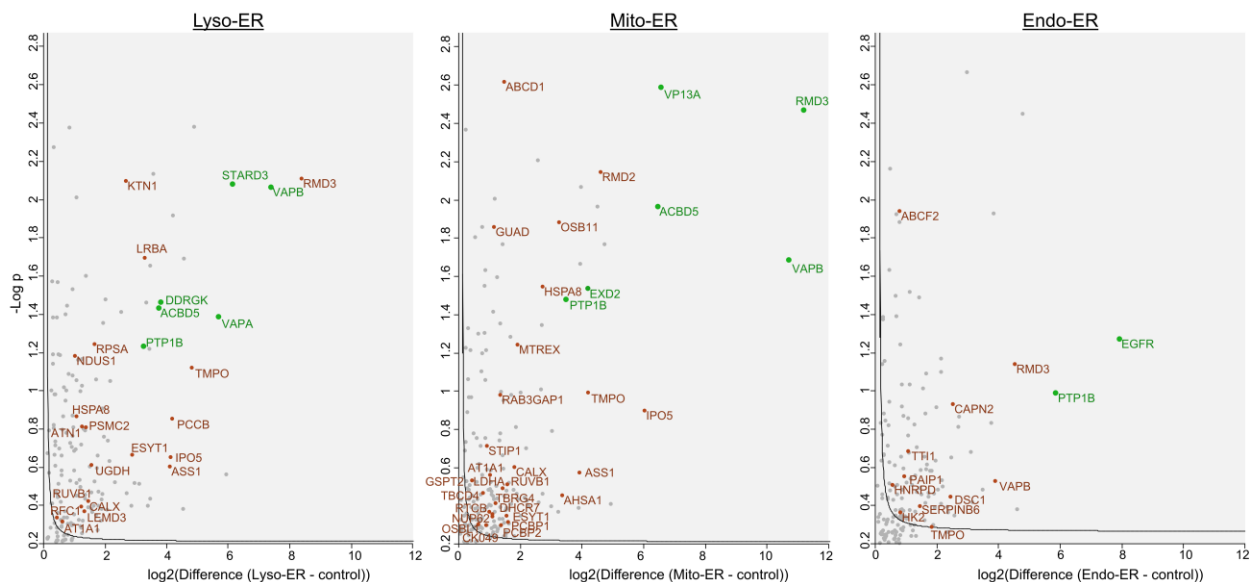


**Figure 16:** Volcano plot of MS results from Split-BioID assay in stable cells – Proteins biotinylated in a Split-BioID assay from stable transfected cells were enriched in a streptavidin pulldown and sent for proteomic analysis to the MS core facility at Heidelberg University. Resulting raw data files were analyzed and significant hits (labeled red) plotted as described in Figure 11 (FDR=0.8, s0=0.2). Hits that were identified in the same Split-BioID sample in the first screen are marked green.

### 3 Results and Discussion - 3.1 Split-BioID at membrane contact sites

Comparison of the 33 proteins identified in the Mito-ER samples with the previously mentioned four proximity labelling assays performed at ER-mitochondria contact sites [41,42,52,53] showed with 12-15% a lower overlap than the previous screen. Organelle specificity, however, was similar as before with ~28% of the proteins associated with mitochondria in the GO-term analysis. Proteins that were detected in this experiment and at least two of the other screens are CANX, DHCR7, EXD2, PTP1B, LAP2 and VAPB. The enrichment over the negative control and the consistency between the two replicates was however much lower than in the initial MS screen (Table 5), while the quality of the results varied much more between the three Split-BioID constructs this time. Reasons for this lower quality could be many. Affinity purification using the new brand of streptavidin beads, for example, seemed to enrich preferably those proteins that already showed the strongest biotinylation. This might indicate a preferential binding of multi-biotinylated proteins to the beads and could have led to the suppression of the mass spectroscopic detection of proteins that interact only transiently or weakly with the bait proteins.

**Table 4:** List of significant hits resulting from a second proteomic screen of targets biotinylated by Split-BioID at membrane contact sites in stable transfected cells, sorted by the samples they were identified in.

Lyso-ER	Mito-ER	Endo-ER	Lyso-ER + Mito-ER	Lyso-ER + Endo-ER	Mito-ER + Endo-ER	All three
ATN1	ABCD1	ABCF2	ACBD5			PTP1B RMD3 LAP2 VAPB
DDRKG1	AHSA1	CAPN2	ASS1			
KTN1	CK049	DSC1	ATP1A1			
LEMD3	DHCR7	EGFR	CANX			
LRBA	EXD2	HK2	ESYT1			
NDUFS1	GDA	HNRNPD	HSPA8			
PCCB	GSPT2	PAIP1	IPO5			
PSMC2	LDHA	SERPINB6	RUVBL1			
RFC1	MTREX	TTI1				
RPSA	NUP62					
STARD3	OSBPL11					
UGDH	OSBPL1A					
VAPA	PCBP1					
	PCBP2					
	RAB3GAP1					
	RMDN2					
	RTCB					
	STIP1					
	TBC1D4					
	TBRG4					
	VPS13A					

**Table 5:** Evaluation of the results of the second proteomic screen – 1) Average LFQ enrichment of all significant hits in the Split-BioID samples compared to the unspecific BioID control. 2) Average difference between the LFQ values in the two replicates of all significant hits.

Sample	1) Mean fold-difference of hits over control ( $\pm$ SE)	2) Mean fold-difference of hits between replicates ( $\pm$ SE)
Lyso-ER	34.5x ( $\pm$ 16.8)	1.7x ( $\pm$ 0.2)
Mito-ER	14.9x ( $\pm$ 4.7)	2.2x ( $\pm$ 0.3)
Endo-ER	7.7x ( $\pm$ 2.5)	8.1x ( $\pm$ 3.5)

Additionally, problems of the MS equipment cannot be ruled out as a contributing factor, since the facility reported multiple issues with the hardware in the previous measurements. In order to rule out the MS facility as a problem and to test the robustness of the assay, we decided to perform the Split-BioID assay a third time in collaboration with the group of Prof. Christian Freund at the FU Berlin.

Based on a new comparative study on streptavidin beads [47] and elution conditions [191] I decided on a new protocol for the affinity purification step of the assay together with Dr. Benno Kuroopka from the Freund group. More specifically, elution was changed to an even higher excess of biotin (25 mM) and now contained a non-ionic detergent. Additionally, the eluted proteins were concentrated at the interface of a stacking and running gel before being sent to Berlin. This time, the assay was performed in technical triplicates, again using the Ago2-BirA\* cell line as an internal control. Raw data analysis and statistical evaluation was performed as before and resulted in the list of proteins shown in (Figure 17) and (Table 6). For enrichment over the control I filtered for hits that showed at least an average increase of 2x over all three replicates. Average enrichment of the hits compared to the negative control was again much lower than in the screening from transfected cells (Table 7) and especially the Lyso-ER samples showed very low biotinylation levels and high variations between the replicates.

This time only 60% of the 89 identified proteins were found to be associated with membranes, only 18% with the endoplasmic reticulum, 11% with lipids and just two hits with sterols (VAPA and VAPB). Interestingly though, the overlap with the proximity labelling datasets produced by other groups was the highest for this screen. This was especially the case for the two published datasets that were also prepared using a stable expressed split version of a biotin ligase [52,53]. The overlap of the 33 proteins I could identify in the Mito-ER sample of my assay, with these two datasets was 24% and 30% with a similar organelle specificity as before (27%).

### 3 Results and Discussion - 3.1 Split-BioID at membrane contact sites

Hits that were identified in the Mito-ER sample in this third Split-BioID screen and also in one of the two published split biotin ligase screens are ACBD5, DDRGK1, MTFR1L and PGRMC2. Six proteins were even found in all three of these split ligase screens: CISD1, EMD, MAVS, OCIAD1, PGRMC1 and LAP2. Some of these are known to locate to mitochondria (CISD1, PGRMC1) or even to contact sites with the ER (MAVS= mitochondrial antiviral signaling protein, MTFR1L= mitochondrial fission regulator). ACBD5 on the other hand is a peroxisomal protein, which was also shown to induce contact formation with the ER (PX-ER) through interaction with VAP proteins [192]. Since it was identified repeatedly in all Mito-ER samples of my screens and also in one of the published screens looking at the same contacts, it might very well be involved in the creation of three way junctions of ER-PX with mitochondria [193–195]. Numbers of overlapping proteins between all datasets are shown in Table 8. More extensive lists of all identified proteins and a comparative GO-term analysis of all screens can be found in the appendix section.

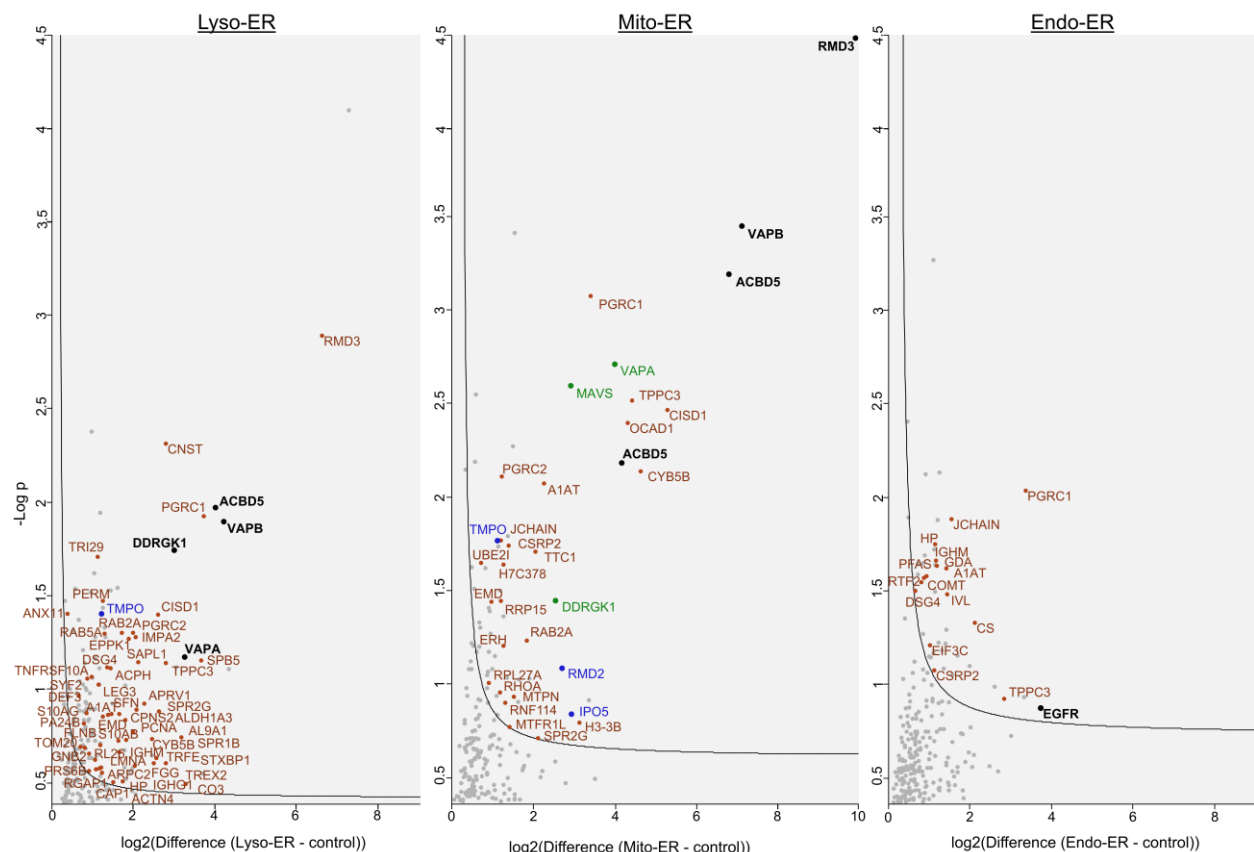


**Figure 17:** Volcano plot of MS results from Split-BioID assay in stable cells – Proteins biotinylated in a Split-BioID assay from stable transfected cells were enriched in a streptavidin pulldown and sent for proteomic analysis to the group of Prof. Christian Freund at the Freie Universität Berlin. Resulting raw data files were analyzed and significant hits (labeled red) plotted as described in Figure 11 (FDR=0.8, s0=0.2). Hits that were identified in the same Split-BioID sample in multiple screens are marked (green = 1st and 3rd, blue = 2nd and 3rd, black = 1st, 2nd and 3rd).

### 3 Results and Discussion - 3.1 Split-BioID at membrane contact sites

**Table 6:** List of significant hits resulting from a proteomic screen of targets biotinylated by Split-BioID at membrane contact sites in stable transfected cells, sorted by the samples they were identified in.

Lyso-ER	Mito-ER	Endo-ER	Lyso-ER + Mito-ER	Lyso-ER + Endo-ER	Mito-ER + Endo-ER	All three
ACTN4	ERH	COMT	ACBD5	DSG4	CSR2	PGRMC1
ALDH1A3	H3-3B	CS	CISD1	HP	JCHAIN	SERPINA1
ALDH9A1	IPO5	EGFR	CYB5B	IGHM		TRAPPC3
ANXA11	MAVS	EIF3C	DDRKG1			
APEH	MTFR1L	GDA	EMD			
ARPC2	MTPN	IVL	PGRMC2			
ASPRV1	OCIAD1	PFAS	RAB2A			
C3	RHOA	RTF2	RMD3			
CAP1	RMDN2		SPRR2G			
CAPNS2	RNF114		LAP2			
CNST	RPL27A		VAPA			
DEFA3	RRP15		VAPB			
EPPK1	TTC1					
FGG	UBE2I					
FLNB						
GNB2						
IGHG1						
IMPA2						
LGALS3						
LMNA						
MPO						
PCNA						
PLA2G4B						
PSAPL1						
PSMC4						
RAB5A						
RACGAP1						
RPL26						
S100A11						
S100A16						
SERPINB5						
SFN						
SPRR1B						
STX1B						
STXBP1						
SYF2						
TF						
TNFRSF10A						
TOMM20						
TREX2						
TRIM29						

### 3 Results and Discussion - 3.1 Split-BioID at membrane contact sites

**Table 7:** Evaluation of the results of the third proteomic screen – 1) Average LFQ enrichment of all significant hits in the Split-BioID samples compared to the unspecific BioID control. 2) Average difference between the LFQ values in the two replicates of all significant hits.

Sample	1) Mean fold-difference of hits over control ( $\pm$ SE)	2) Mean fold-difference of hits between replicates ( $\pm$ SE)
Lyso-ER	8.1 ( $\pm$ 1.8)	4.1 ( $\pm$ 1.0)
Mito-ER	20.0 ( $\pm$ 5.6)	1.9 ( $\pm$ 0.2)
Endo-ER	4.4 ( $\pm$ 1.2)	2.1 ( $\pm$ 0.5)

**Table 8:** Overlaps between proteomic datasets of published proximity labelling screens and the ones performed in this thesis. Full sizes of the complete datasets are: 88 (I.T. Cho), 68 (Hung), 100 (K.F. Cho), 115 (Kwak), 32 (1<sup>st</sup> Mito-ER), 33 (2<sup>nd</sup> Mito-ER), 31 (3<sup>rd</sup> Mito-ER), 63 (1<sup>st</sup> all samples), 55 (2<sup>nd</sup> all samples) and 87 (3<sup>rd</sup> all samples).

<b>Hung 2017</b>	3								
<b>K.F. Cho 2020</b>	12	11							
<b>Kwak 2020</b>	21	12	30						
<b>1<sup>st</sup>, Mito-ER</b>	7	5	5	7					
<b>2<sup>nd</sup>, Mito-ER</b>	4	4	5	4	6				
<b>3<sup>rd</sup>, Mito-ER</b>	4	3	8	10	6	6			
<b>1<sup>st</sup>, all samples</b>	17	7	8	12	32	7	6		
<b>2<sup>nd</sup>, all samples</b>	13	4	5	5	8	32	7	11	
<b>3<sup>rd</sup>, all samples</b>	7	3	8	11	6	7	31	7	9
	<b>I.T. Cho 2017</b>	<b>Hung 2017</b>	<b>K.F. Cho 2020</b>	<b>Kwak 2020</b>	<b>1<sup>st</sup>, Mito-ER</b>	<b>2<sup>nd</sup>, Mito-ER</b>	<b>3<sup>rd</sup>, Mito-ER</b>	<b>1<sup>st</sup>, all samples</b>	<b>2<sup>nd</sup>, all samples</b>

While the repeated identification of a small list of proteins by several independent studies inspires confidence in the validity of these proteins on the one hand, there is still a majority of proteins present in each proteomic screen that seems to be not biotinylated consistently. Interestingly, in my third Split-BioID screen, even two of the usually heavily biotinylated bait proteins (STARD3 and PTP1B) were not identified at all, potentially indicative of a loss of their expression. However, each of their corresponding tether partners was found to be heavily enriched, thus it was unlikely, that expression of the STARD3 and PTP1B BioID constructs failed. Indeed, their correct expression was later also confirmed by immunoblotting and DNA sequencing of the genomic locus of integration. On the other hand, it is worth mentioning that in other experiments, stable, doxycycline-inducible cells also showed decreased performance with higher passage numbers, hinting at a loss in doxycycline-sensitivity or other compensation mechanisms. Overall, reoccurring hits of this analysis with the previous assays were again minimal, with only two non-bait proteins (ACBD5 and DDRGK1) being identified in all three sets of experiments.

In summary, I found the first proteomic screen to result in the highest levels of biotinylation with the lowest variation of the identified hits between the replicates. It also produced the highest amount of hits, related to lipid transport processes, but due to the observed mislocalization of the baits, these results have to be treated with caution. The second screen on the other hand showed much lower biotinylation levels, the highest variation between replicates and also the lowest overlap in hits with the previously published datasets. The most overlapping protein hits were observed between the third screen and the two published datasets, which were produced using very similar split biotin ligase assays. Although overall biotinylation levels were rather low in this screen and the amount of lipid transporting proteins in the hit list were lowest, it still inspires the highest level of confidence of the three screens.

These discrepancies between the three proteomic screens suggest a very high susceptibility of the assay to any changes in the culture conditions, affinity purification or sample preparation for the mass spectrometric analysis. The fact that even the replicates of one experiment showed sometimes very high variations, although they were created under the same conditions, made it difficult to correctly interpret and follow up on the results of those experiments. A potential reduction of some of the variations might be achieved in the future by reducing the time given to allow biotinylation in the cells. To this end one should change from the Split-BioID system, which uses fragments of the full length BirA\* ligase, to a more efficient version like a Split-TurboID [50,53] where biotinylation time can be drastically reduced down to 1 hour or even less.

#### 3.1.5 Validation of proteins of interest

In order to more closely investigate several selected hit proteins, I decided to biochemically validate them via immunoblotting. First I focused on the mitochondrial antiviral signaling protein (MAVS), which has been reported to localize to MAMs [40,196] and was identified exclusively in the Mito-ER samples in two of my MS screens and also in three of the previously published datasets. Since detection of endogenous levels of MAVS could not be achieved with the available antibodies, I decided to transfect stable cells expressing the used BioID constructs with GFP-MAVS before starting the biotinylation assay through induction with doxycycline and addition of biotin. After enrichment of the biotinylated proteins via a streptavidin pulldown and western blot analysis of the eluate using an  $\alpha$ GFP antibody, I could observe selective biotinylation of GFP-MAVS in only some of the cell lines (Figure 18). As expected, strongest biotinylation occurred in the cell line expressing the mitochondrial RMD3 with a full length BirA\*, since it is located in the same membrane and is not dependent on reassembly of the biotin ligase. Surprisingly, the only other cell line that showed GFP-MAVS in the eluate of the pulldown was the one expressing the ER resident PTP1B, which could be attributed to a potential role of the phosphatase PTP1B at ER-mitochondria contact sites. This is supported by the high level of biotinylation of PTP1B in the Lyso-ER and the Mito-ER samples of the first two proteomic screens (Figure 16 and Figure 17). Contrary to expectations, however, neither the cell line expressing BirA\*-VAPB, nor the one expressing the Mito-ER Split-BioID construct led to biotinylation of GFP-MAVS, although expression of GFP-MAVS was the same for all cell lines (Figure 18, top panel) and the enrichment of biotinylated proteins was also successful (bottom panels). This is likely due to the strongly reduced level of biotinylation in the Split-BioID samples (as apparent from the streptavidin staining in Figure 14), such that a higher amount of protein would be required to detect GFP-MAVS in the eluate.

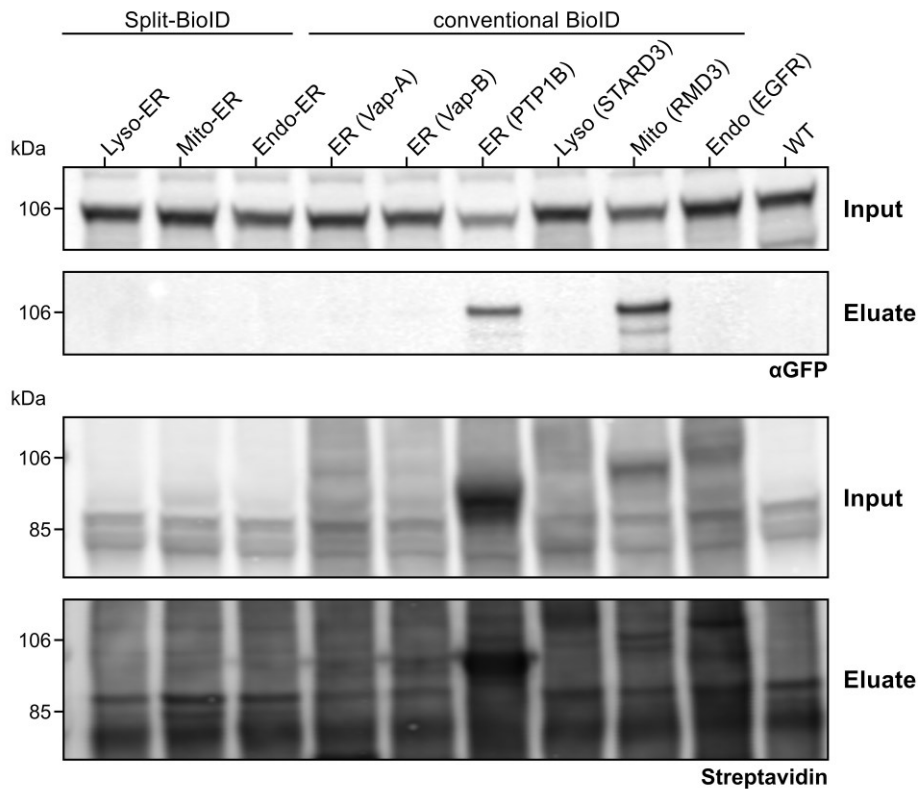


**Figure 18:** Immunoblot of MAVS biotinylated by different BioID constructs – Stable cells expressing the conventional (non-split) and the Split-BioID constructs were induced with 25 ng/ml doxycycline and transfected with GFP-MAVS under a CMV promoter. After incubation with 50  $\mu$ M biotin for 24 hours to allow biotinylation, the cells were harvested, lysed and equal amounts of total protein loaded on streptavidin beads. Eluted proteins were then subjected to western blot analysis using an  $\alpha$ GFP antibody and fluorescently labelled streptavidin.

Besides MAVS, I chose to compare biotinylation levels of the two hits that were most consistently identified in all three MS screenings and also found in the previously discussed datasets: DDRGK1 and ACBD5. To be able to compare biotinylation levels of endogenous proteins, I decided to not use overexpression as a GFP-tagged fusion as with MAVS. Instead I opted to scale up the Split-BioID assay and maximize concentrations in the eluate of the streptavidin pulldown, which would, unlike before, also allow me to compare the biotinylation levels produced by the Split-BioID constructs. For comparison with the initial biotinylation screening, I decided to include transiently transfected cells in the experiment as well. The Split-BioID assays were performed after the same protocol as the third MS screen, only with increased amounts of total protein (5 mg) as input for the streptavidin pulldown.

DDRGK1 (DDRGK domain containing protein 1) is an ER membrane protein, that recruits UFL1 (UFM1 protein ligase) in response to disturbances in ER homeostasis. The resulting UFMylation of target proteins involved in protein synthesis leads to ER-phagy, as a

proactive measure to prevent an unfolded protein response (UPR) and ultimately apoptosis [189,197].

In the mass spectrometric screening from stable cell lines, DDRGK1 was identified only in the Lyso-ER sample or in both the Lyso-ER and the Mito-ER samples, while transient transfection resulted in the identification of DDRGK1 in all three samples with much higher biotinylation. This might be explained by the fact that expression of bait proteins from plasmids at much higher doxycycline levels had led to aggregation (Figure 12), which might have triggered an ER-stress response involving increased levels of DDRGK1. In one of the three samples even its target UFL1 was identified as a significantly enriched hit, which further supports this theory.

The second reoccurring hit is the peroxisomal membrane protein ACBD5 (acyl-CoA binding-domain containing protein), which has been reported to tether ER-peroxisome contact sites, necessary for maintenance of peroxisomes and cellular cholesterol levels [192]. Tethering by ACBD5 is enabled through its binding to VAP proteins, which explains why ACBD5 was identified in all three MS screens in both the Lyso-ER and the Mito-ER sample, as they use VAP-A and VAP-B as the bait protein at the ER. Since biotinylation by the split BirA\* can only occur if both tether pairs come into proximity this might indicate a role of ACBD5 at three-way contact sites of peroxisomes with two other organelles. While this has been mostly reported for contacts of peroxisomes with ER and mitochondria [193–195], there is also evidence for three-way junctions involving late endosomes and lysosomes [124]. Together with the fact that peroxisomes have been found to contact lysosomes themselves [198], this could explain the biotinylation of ACBD5 in Lyso-ER and Endo-ER samples.

The presence of DDRGK1 and ACBD5 in the eluted samples of Split-BioID assays from transiently and stably expressing cells was analyzed by immunoblotting using endogenous antibodies (Figure 19). These experiments were conducted in triplicates and quantified (Figure 20). To a certain extent the results reflected what was observed in the MS screenings. For example, ACBD5 was biotinylated predominantly in VAP-mediated BioID samples (Lyso-ER and Mito-ER) and DDRGK1 showed more biotinylation in transiently transfected cells where high bait expression levels might again have caused more ER-stress. Despite the previously described shortcomings of the transient overexpression, the results of their biochemical biotinylation analysis reflected more accurately, what was observed in the corresponding MS screens.

### 3 Results and Discussion - 3.1 Split-BioID at membrane contact sites

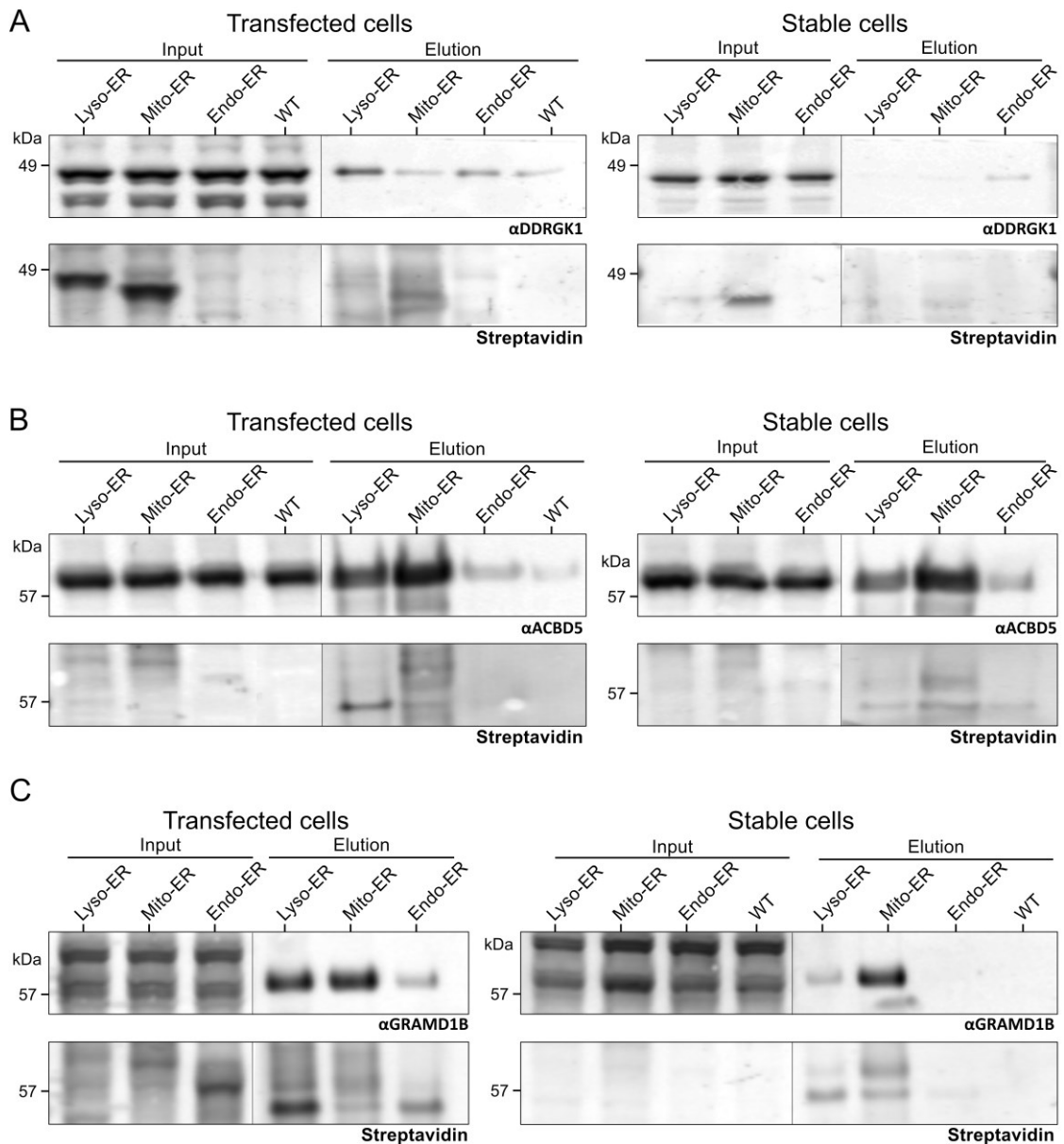


**Figure 19:** Immunoblot analysis of biotinylation levels of proteins of interest (POIs) in transient and stable transfected cells - HeLa 11ht wild type cells were transfected with the Split-BioID constructs. After 1 day, expression was induced in transient and stable transfected cells using doxycycline at concentrations of 100 ng/ml or 25 ng/ml, respectively. After incubation with 50  $\mu$ M biotin for 24 hours to allow biotinylation, the cells were harvested, lysed and equal amounts of total protein loaded on streptavidin beads. Eluted proteins were then subjected to western blot analysis using endogenous antibodies against the proteins of interest as well as fluorescently labelled streptavidin.

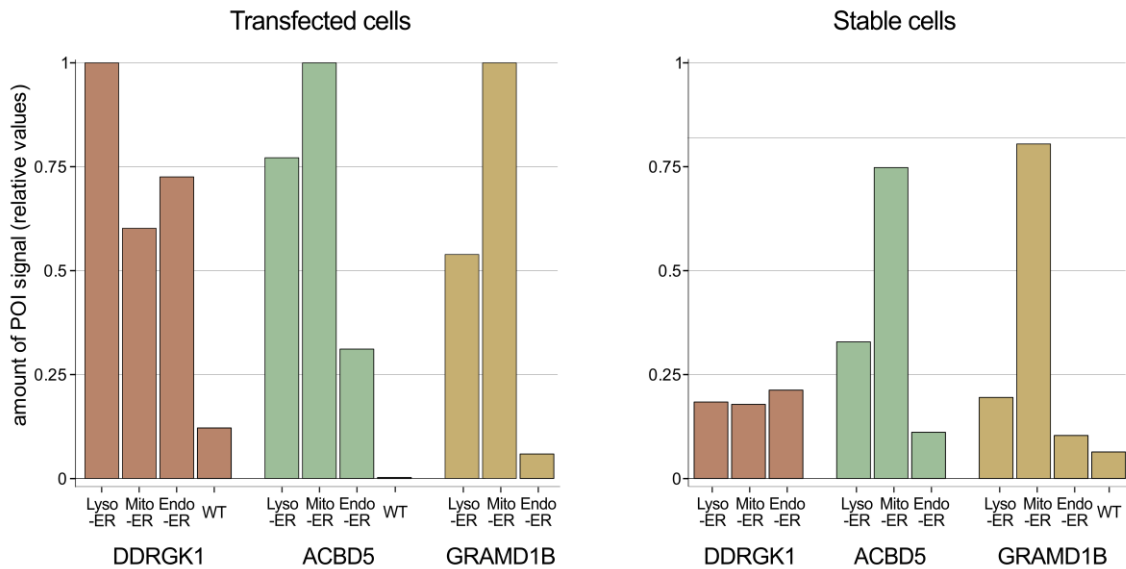


**Figure 20:** Quantification of POI levels in streptavidin pulldown – Endogenous antibody signals in the eluates of the western blots presented in **Figure 19** were quantified and divided by the corresponding total amount of streptavidin signal in the sample (DDRGK1, ACBD5: n=3, GRAMD1B: n=2).

As a third protein of interest, I looked to compare biotinylation levels of the sterol transporting protein GRAMD1B, which is known to locate to ER-LE/Lys contact sites [30] and was successfully identified in the corresponding Split-BioID samples (Lyso-ER, Endo-ER) in the first proteomic screening. Biotinylation analysis by immunoblotting was performed in transiently transfected and stable Split-BioID cells the same way as for DDRGK1 and ACBD5 (Figure 19C). In contrast to the proteomic screens, here I was able to show GRAMD1B to be reliably biotinylated not only by the Split-BioID assay in transiently transfected but also in stable cell lines. I found GRAMD1B to be consistently biotinylated in the Lyso-ER and Endo-ER samples but surprisingly, both in the transfected and the stable cells the highest biotinylation levels were observed in the Mito-ER samples. This discrepancy might be explained by different beads and elution protocols used in the two sets of experiments. Alternatively, it might be attributed to adaptations of the stable cell lines after longer periods of cultivation, since total biotinylation levels by the three Split-BioID constructs in this assay (Figure 19, streptavidin panels) were found to differ much more than in the initial screenings of the cells (Figure 14).

While the biotinylation specificity of the Split-BioID constructs in the western blot analysis differed from the results of the proteomic screens, there is also evidence to support GRAMD1B localization to contact sites with mitochondria, based on a predicted mitochondrial targeting sequence in GRAMD1B that proved essential for cholesterol delivery to mitochondria [155]. The yeast homologue of GRAMD1B (Ltc1/Lam6) was also

shown to expand the contact sites of the ER with mitochondria or with the vacuole [28,156]. This further suggests a secondary role for GRAMD1B, which takes place at these contact sites, in addition to its recently revealed function at ER-PM contacts [150]. While a potential novel role for GRAMD1B at Mito-ER contact sites is an exciting topic for future studies, I next focused on investigating the potential function of GRAMD1B at Lyso-ER contact sites. While its co-presence at this contact with the lysosomal protein NPC1 was described before [30], it was yet unclear whether the sterol trafficking ability of GRAMD1B also contributed to direct cholesterol exchange between ER and lysosomes. To better understand the mechanism for this alternative localization to contact sites with lysosomes I decided to look further into GRAMD1B's interplay with NPC and also study the timescales of the cholesterol transport processes facilitated by GRAMD1B.

## 3.2 GRAMD1B at Lysosome-ER contact sites

As described in more detail in chapter 1.2.6.2 GRAMD1B is an ER resident transmembrane protein that is able to bind cholesterol and transfer it between two adjacent membranes, potentially driven by a counter-exchange with PI(4,5)P<sub>2</sub> [152]. GRAMD1B and its yeast orthologue (Ltc1/Lam6) were also shown to form contacts between the ER and other intracellular organelles [28,30,70,154–156], where they could be found to support cholesterol transport in either direction, depending on the contacting organelle. At contacts of the ER with lysosomes, GRAMD1B was shown to co-localize with the cholesterol exporting protein NPC1 [30] and both proteins have been shown to be essential for sufficient cholesterol transport to the ER. GRAMD1B could therefore potentially act as both a tether and as a mediator of direct cholesterol import of NPC1-liberated cholesterol to the ER. Alternatively, GRAMD1B might exert its main function in cholesterol import at the plasma membrane instead, completely independent from its role at contact sites with lysosomes. For its function at the PM, GRAMD1B is able to sense and bind phosphatidylserine (PS) in cholesterol-rich membranes via its PH-like GRAM domain [146,147], which results in the recruitment of ER tubules to the plasma membrane (PM) when cellular cholesterol levels are high [150].

Here I was trying to answer the question whether GRAMD1B has a dual function as a tether and cholesterol transporter at ER-LE/Lys contact sites and whether this interaction is dependent on NPC1.

### 3.2.1 Lysosome to ER transport of Lyso-pacCholesterol is facilitated by GRAMD1B

#### 3.2.1.1 NPC1 is necessary for Lyso-pacChol import to the ER by GRAMD1B

Aiming to unravel the involvement of ER-lysosome contact sites in GRAMD1B mediated cholesterol transport, I decided to make use of a novel cholesterol analogue that was developed by Janathan Altuzar in our lab [182]. As described in more details in chapter 1.3.1, Lyso-pacChol is a trifunctional lipid probe [178], that was additionally modified for pre-localization to lysosomes.

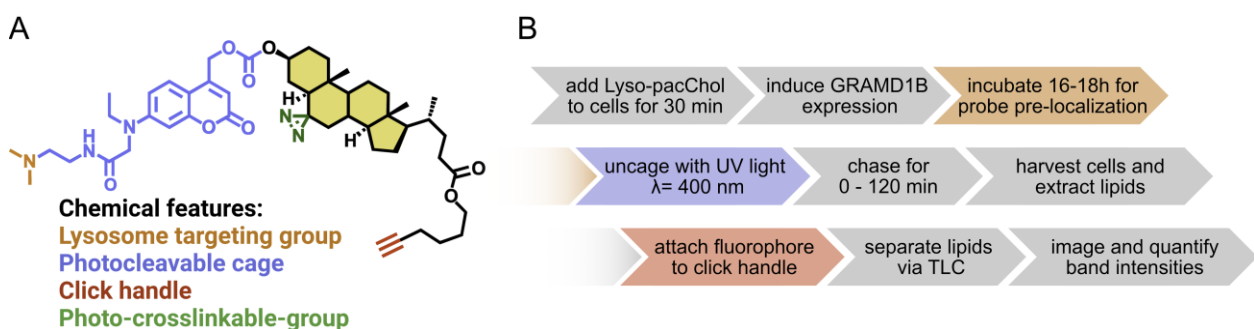


**Figure 21:** A) Structure of Lyso-pacCholesterol – This cholesterol analogue, which was developed and synthesized by J. Altuzar [182], provides a multitude of functions for the study of cholesterol homeostasis. Fed to cells it pre-localizes to lysosomes over the next 16 hours where it remains inert until the photocleavable cage group is removed by UV irradiation. The released pacCholesterol is metabolized and transported similarly to endogenous cholesterol and can be photo-crosslinked to interacting proteins via the diazirine ring. The alkyne click handle allows a variety of additional functionalization i.e. affinity purification of crosslinked lipid-protein pairs or visualization of the probe in cells or lipid extracts. B) Workflow used to analyze the conversion rate of Lyso-pacCholesterol to an ester in the presence of overexpressed GRAMD1B.

When added to the growth medium, it is readily taken up by cells and, due to a positive charge resulting from the protonation of a tertiary amine, it is retained inside the acidic lumen of late endosomes and lysosomes. After a short irradiation of the cells with UV light with wavelength of ~400 nm, the lysosome targeting group and the bulky coumarin cage group are cleaved off, which results in a timed release of bioactive cholesterol that is transported through the cell and metabolized in a similar way as endogenous cholesterol. Additional functional groups for photo-crosslinking and click-chemistry enable the visualization of the subcellular localization of the probe or the identification of its interaction partners at selected timepoints. After extraction of the cells lipidome and linking of a clickable fluorophore to the metabolites of the probe, a subsequent thin layer chromatography (TLC) analysis can be used to quantify the amount of pac-cholesteryl ester that was synthesized in the time between uncaging and cell lysis.

I used this method to analyze the effect of GRAMD1B overexpression on the efficiency of cholesterol transport from lysosomes to the ER in HeLa wild type and NPC1 deficient cells. For this I created cell lines which stably express GFP-GRAMD1B under a tetracycline-inducible promoter and an NPC1-knock out in the same background.

I pulsed the cells with Lyso-pacChol for 30 minutes and then added fresh medium with or without doxycycline and allowed GRAMD1B expression and probe pre-localization to occur for 16-18 h. Lyso-pacChol was then uncaged and allowed to distribute through the cell for 0-120 minutes before cell harvest and lysis. The results of the TLC analysis are shown in Figure 22.

The intensity of the released pacChol band decreased with ongoing chase times, while a second band migrating at higher R<sub>f</sub> values appeared over time. Since metabolism of cholesterol consists under usual conditions almost exclusively of the synthesis and hydrolysis of its corresponding esters, I was able to calculate the percentage of uncaged Lyso-pacChol that was esterified by simply building the ratio of the pacChol-ester band to the sum of the pacChol and the ester band. Here I could observe an increase in ester synthesis when expression of GFP-GRAMD1B was induced. In uninduced WT cells, the production of pacChol-esters seemed to plateau at levels of 25-30% after 30 or 60 minutes of chase. Although it is worth mentioning that the difference between replicates and hence the error bars are large. Nevertheless, overexpression of GFP-GRAMD1B led to significantly higher esterification, at the latest timepoint. Interestingly an increase in esterification as an effect of GRAMD1B overexpression could also be consistently observed at the earliest timepoint (0 min). Here it is important to note that, due to the time that is necessary for sample handling and cell harvest, a chase time of 0 minutes still resulted in about 5 minutes of cell activity between the beginning of the UV irradiation and the chilling of the harvested cells. In agreement with what was described by Altuzar et al. [182], I could observe an overall decreased esterification rate in NPC1 knock-out cells, due to a deficit in Lyso-pacChol export from the lysosomes. After longer chase times (60 - 120 min) this effect could partially be rescued by overexpression of GRAMD1B. The increase in esterification over time as a result of induced expression of GRAMD1B was however lower in NPC1 cells, which points towards a role of NPC1 in GRAMD1Bs mode of operation.



Overall, these data, in particular the increase of GRAMD1B-mediated esterification, support a role of GRAMD1B in lysosomal cholesterol export. Due to GRAMD1B's ability to detect the coincidence of PS and high levels of cholesterol, recruitment to lysosomes could also be independent of protein-protein interaction with NPC1 and rather be mediated through direct sensing of the lipid composition at the lysosome. Although the levels of PS are much lower in endosomes than in the PM and even decreases with vesicle maturation [64], an increased cholesterol concentration in the limiting membrane could be enough to trigger coincidence-sensing by GRAMD1B and recruitment of ER tubules. The difference between increased esterification at early times as well as at late times after uncaging might be explained by two distinct transports of cholesterol by GRAMD1B: a fast one that is "ready-to-go" from the beginning and a slower one that might be only induced after sensing of increased total cholesterol levels.

#### 3.2.1.2 ALOD4 reduces Lyso-pacChol transport to the ER

In the next experiments, I looked to untangle the known effects of GRAMD1B at ER-PM contact sites from my previously found potential direct effect at Lyso-ER contacts. I set out to study the two proposed modes of action of GRAMD1B separately from each other by eliminating one of the transport routes. For this I aimed to block the transport route via the PM, using domain 4 of the bacterial cholesterol dependent cytotoxin (CDC) anthrolysin O (ALOD4). This small protein is not only able to bind to the accessible pool of cholesterol in the plasma membrane [199], which allows its quantification using FACS based readouts [200], but was also shown to trap cholesterol in this pool [128]. By stopping increasing levels of cholesterol at the plasma membrane to be transported to the ER via GRAMD1B I would then be able to quantify how big the potential contribution of the direct cholesterol transport by GRAMD1B at Lyso-ER contact sites is. First I purified recombinant ALOD4 from bacteria using the multi-step clean-up protocol described by Endapally et al. [201]. The protocol uses subsequent affinity, anion exchange and size exclusion chromatography to achieve the high level of purity necessary for site-specific fluorescence labelling, which allows the evaluation of its ability to bind to the surface of living cells. The specificity of ALOD4 binding was confirmed by comparing it to a mutant variant that is unable to bind cholesterol (ALOD4-Mut).

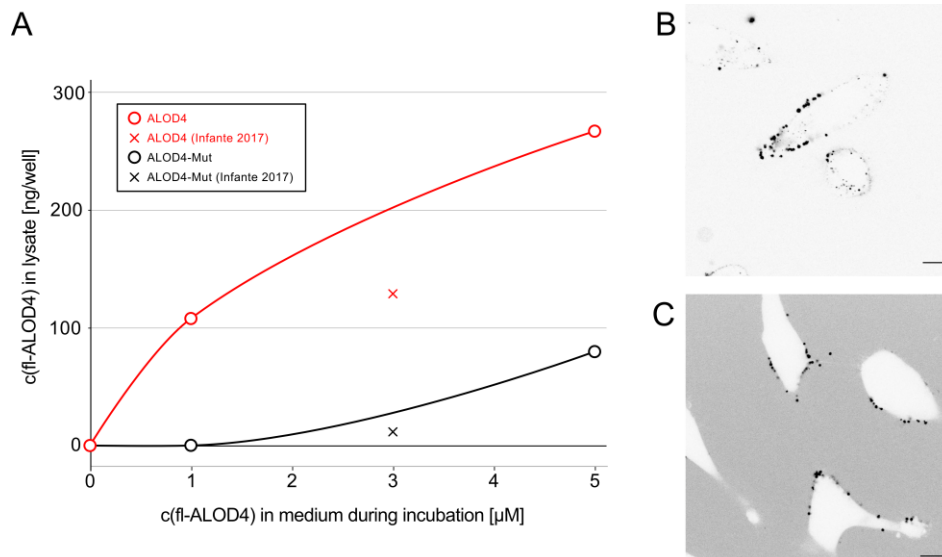


**Figure 23:** Validation of ALOD4-binding – Purified recombinant ALOD4 and cholesterol-binding mutant (ALOD4-Mut) were fluorescently labelled with Alexa 546 maleimide, added to the medium of HeLa cells for 1 hour and the amount of bound protein was measured (A). Concentrations were calculated using the fluorophore’s extinction coefficient and previously determined protein labelling efficiency. Successfully binding was also validated using live-cell imaging of cells during incubation (C) with fluorescent ALOD4 and after washing of the cells (B).

Here I was able to observe binding levels for both protein variants that were very similar to those reported by the original authors [128] (Figure 23A). Surprisingly, live cell analysis of fluorescent ALOD4 bound to cells revealed binding to occur very heterogeneously in large clusters at the cell surface (Figure 23B). Previous aggregation or even precipitation of the highly concentrated purified protein could be ruled out as cause for this, since imaging of the cells directly after the addition of ALOD4 revealed that there were no clusters present in the medium (Figure 23C). Whether this clustering might reflect an actual heterogeneous accessibility of cholesterol at the cell surface is however unclear. Curiously, no other publication using this fluorescently labelled cholesterol probe has ever mentioned its use in fluorescence microscopy.

After its binding to cells in a cholesterol-dependent manner had been verified I applied the purified ALOD4 in the previously described Lyso-pacChol assay. For this I allowed binding of ALOD4 to the cells for 1 hour before uncaging of the probe. ALOD4 was also present in the medium during the chase periods to trap Lyso-pacChol that was transported to the plasma membrane. The results of these experiments are shown in Figure 24.

When ALOD4 was added to the cells I could observe both in uninduced cells and in cells overexpressing GFP-GRAMD1B a slight, however not significant, decrease in Lyso-pacChol esterification after longer chase times (60 min, 120 min), which might suggest successful trapping of cholesterol at the plasma membrane. A significant decrease

caused by ALOD4 addition could only be observed at the latest timepoint (120 min) in cells overexpressing GRAMD1B, where the percentage of Lyso-pacChol converted to ester was reduced from 32% to 21%. More conclusive interpretation of this experiment was hampered by very high variations in the esterification of the uninduced WT cells at late timepoints. This could potentially stem from a slight difference in the handling of the cells as compared to the previous experiment: a 1 hour incubation step using fresh medium without Lyso-pacChol before uncaging, which was included to mimick the conditions of the ALOD4 addition. This could have changed the nutrient status of the cell and might have caused the high variation of the extent of cholesterol esterification. However, the increased esterification upon GRAMD1B expression at early timepoints (0 min) remained consistent, even in the presence of ALOD4, whereas the plateau of pacChol-esters at the latest timepoint (120 min) was significantly decreased in induced cells when ALOD4 was added. This points towards a role for PM cholesterol in the observed later esterification phenotype, while the direct actions of GRAMD1B likely manifest in the very early timepoints upon uncaging.

Future experiments to observe this effect further could be performed using MS-based lipidomic analysis to allow parallel quantification of endogenous cholesterol. This way some factors contributing to the high variations between replicates might be avoided.

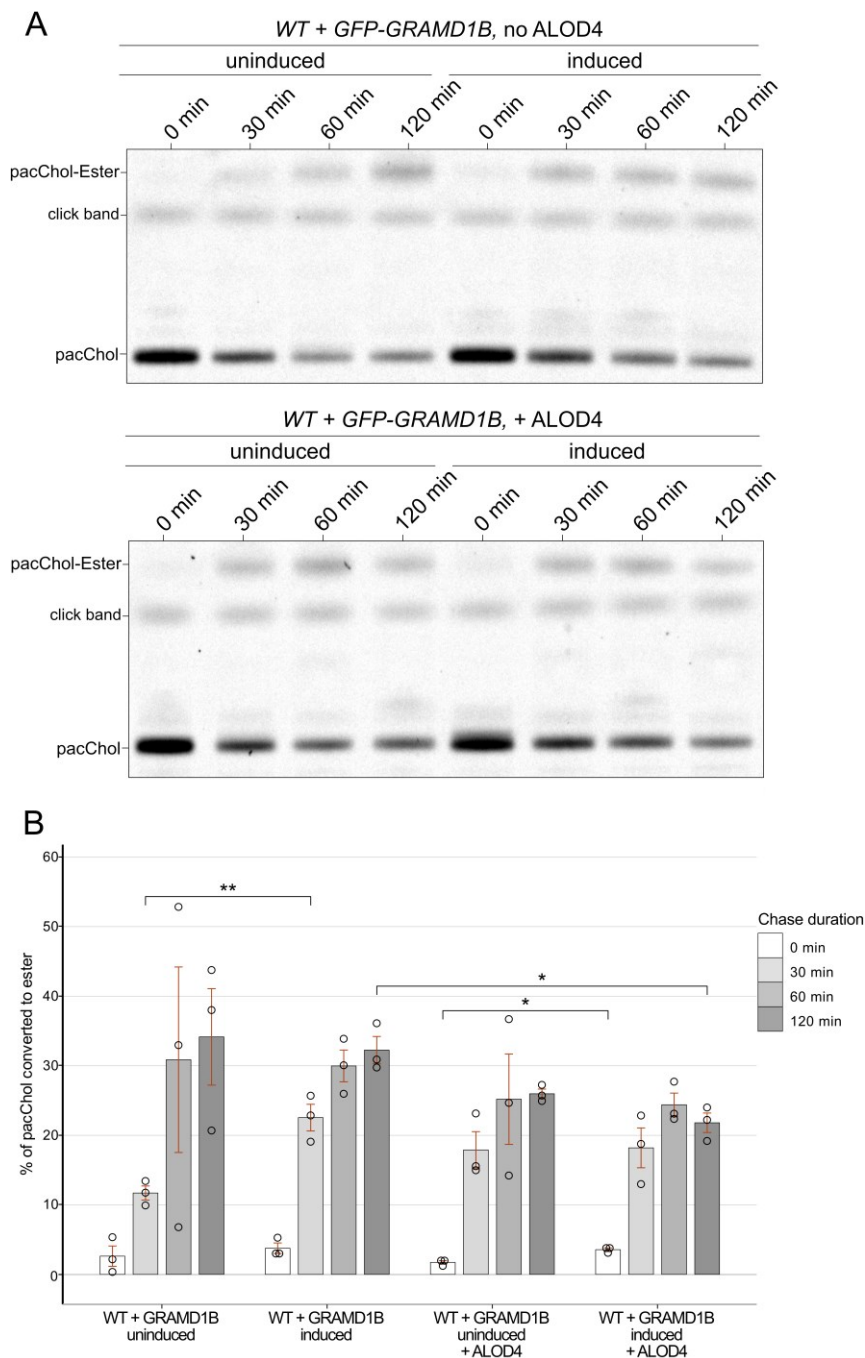


**Figure 24:** Thin layer chromatographic analysis of Lyso-pacCholesterol esterification in the presence of ALOD4 – HeLa cells stably transfected with GFP-GRAMD1B were grown in tetracycline free complete medium for 2 days before the addition of 10  $\mu$ M Lyso-pacCholesterol and 200 ng/ml doxycycline to induce expression. After incubation for 16-18 hours to allow pre-localization of Lyso-pacChol, fresh medium was added with or without 3  $\mu$ M ALOD4. After 1 hour of incubation at 37°C, the medium was taken off and cells were irradiated for 90 seconds with UV light (~400 nm) to uncage the lipid probe. ALOD4-containing medium was then added back and the cells placed in the incubator for the indicated chase durations before being harvested and subjected to lipid extraction. Extracted pacCholesterols were fluorescently labelled using copper-based click chemistry and separated via thin layer chromatography. Percentage of uncaged pacCholesterol converted to ester was calculated by dividing the signal of the pacChol-ester band by the sum of the ester and the pacChol band (n=3, two-tailed paired t-test, \*\*= p<0.01, \*= p<0.05).

To summarize, here I was able to show, using a lysosome-targeted uncageable cholesterol probe, that the esterification rate of lysosome derived cholesterol is increased by the overexpression of GRAMD1B both after a very short period of time (<5 min) and also after a plateau is reached (60-120 min). The effect at these later timepoints was reduced by the addition of ALOD4, which is capable of trapping cholesterol in the plasma membrane, while the GRAMD1B-dependent increase detected at an early time point was unaffected by ALOD4.

These results highlight the great potential of using Lyso-pacCholesterol in studying cholesterol distribution and metabolism. The possibility to release a large amount of traceable cholesterol almost instantaneously and specifically at lysosomes offers a huge benefit over other pulse chase experiments, that rely on relatively slow endocytosis of a probe by the cells or integration in the plasma membrane [30,167,168,202,203] as a starting point of the experiment. The observed increase of esterification upon GRAMD1B induction at the earliest possible timepoints also highlights the importance of a high temporal resolution especially in the study of the fast export of cholesterol from lysosomes. Due to the different effects that GRAMD1B overexpression had at early or late timepoints I suspected GRAMD1B to have a dual function in cholesterol import to the ER.

Here, the increased esterification at the earliest timepoint can most likely be attributed to a direct cholesterol import by pre-localized GRAMD1B at lysosome-ER contact sites. The GRAMD1B-mediated transport of cholesterol from the PM to the ER, however, relies on the recruitment of GRAMD1B, which is much slower and was shown to happen over a period of 15-20 min [146,147]. Lyso-pacCholesterol travelling through this route also needs to be transported from the lysosome to the PM first, which also depends on relatively slow organellar relocalization or transport through recycling endosomes [125,126]. This might explain, why a clear effect of GRAMD1B overexpression on Lyso-pacChol esterification could only be observed again at much later timepoints (60 min, 120 min) and less after 30 minutes.

Focusing on the direct actions of GRAMD1B at lysosome-ER contact sites, I decided to look further into the role of lysosomal cholesterol in the recruitment of GRAMD1B to contact sites with lysosomes and whether NPC1 is involved in it.

#### 3.2.2 GRAMD1B is recruited to LDL-rich endosomes in an NPC1 dependent manner

At the plasma membrane, recruitment of ER tubules via GRAMD1B was shown to occur in a matter of minutes in response to loading the membrane with cholesterol using cyclodextrin [150]. In order to analyze whether similar recruitment also occurs in response to increased cholesterol levels in the lysosomal limiting membrane, I incubated HeLa cells that stably express GFP-GRAMD1B under a tetracycline-controlled promoter with fluorescently labelled LDL particles (DiI-LDL). To study the influence of NPC1 presence in the lysosomal membrane I also created a NPC1-deficient cell line expressing the same construct. To improve LDL uptake and ensure rapid cholesteryl ester hydrolysis and export from lysosomes, I starved the cells for two days using charcoal stripped FBS, before inducing the expression of GRAMD1B. Endocytosed DiI-LDL was readily taken up by the cells within minutes and could be traced throughout the cell for up to one hour using live cell fluorescence microscopy equipped with an Airyscan detector for higher resolution.

To be able to track movement of LDL particles and ER tubules, the acquisition settings were optimized for short frame times, with compromises to resolution and noise reduction (Figure 25A). The deconvolutive image processing of the Airyscan raw image resulted in a greatly improved image clarity (Figure 25B) that allowed to make qualitative assessments about size, position and movement of ER tubules and enabled locating of LDL particles using maxima detection (Figure 25C). However, since endosomes and ER-tubules are highly motile, it was not as obvious whether GRAMD1B relocalization towards LDL particles occurred, as it was when cholesterol is incorporated directly into the plasma membrane [150]. For the same reason, tracing of single particles through the video was also found to be impossible at the used frame times of  $\sim 0.6 \mu\text{s}$ , hence, I decided to quantify the GFP signal around all LDL particles at any timepoint separately. Exemplary videos of the processed and unprocessed live-cell recordings can be found under the link provided in the appendix section of this work. Since the Airyscan processing is not compatible with quantitative measurements, I used the raw image to quantify the GFP-signal surrounding the endocytosed LDL particles. By measuring the GFP signal in multiple ring-shaped regions of interest (ROI) with increasing radii around the particle location, I found ER tubules in proximity to endocytic vesicles to be located predominantly

in a distance between 0.375  $\mu\text{m}$  and 0.625  $\mu\text{m}$  from the center of the LDL particles (Figure 25D).

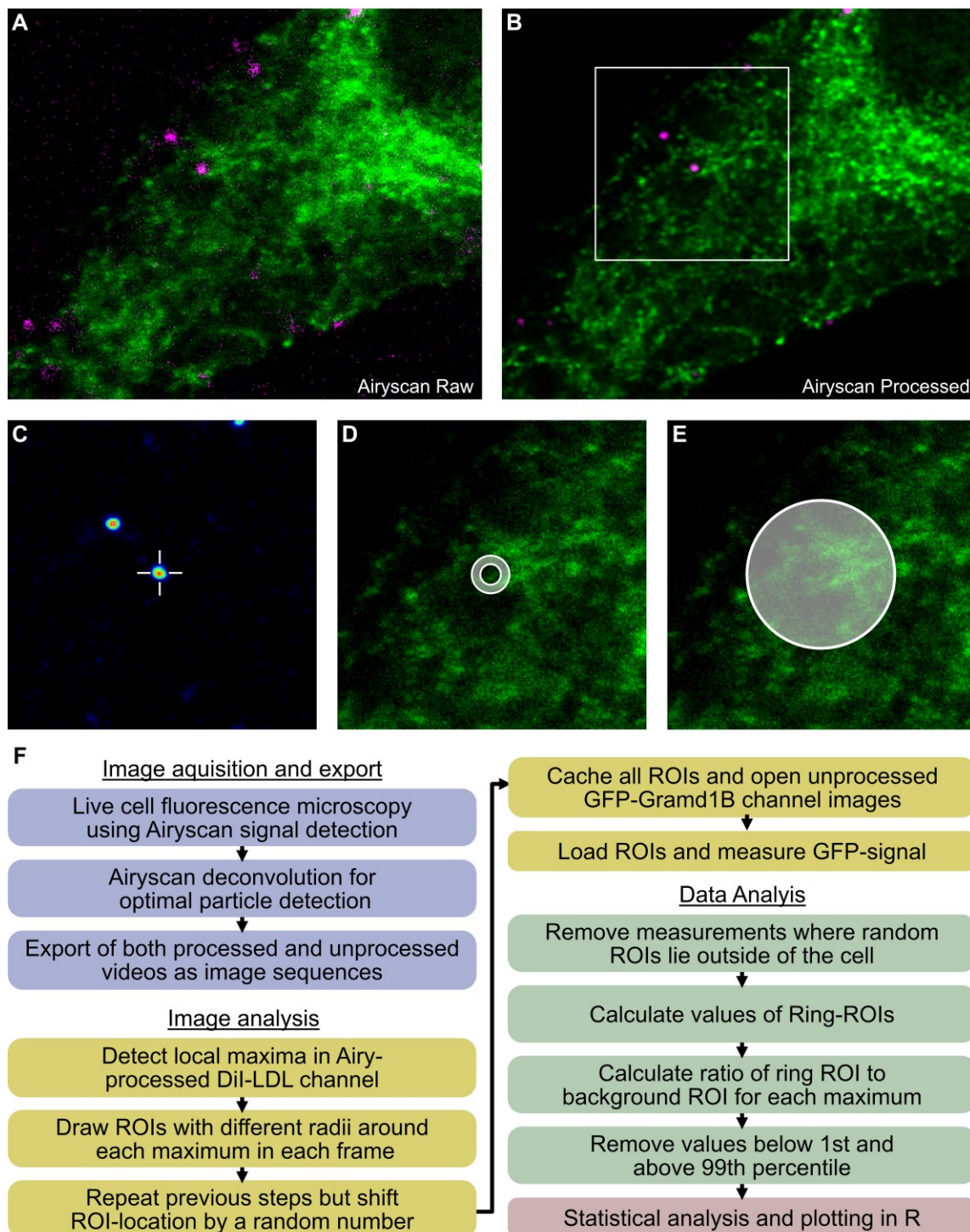


**Figure 25:** Live cell imaging and workflow to analyze GRAMD1B recruitment to LDL containing endosomes – HeLa cells stably transfected with GFP-GRAMD1B were starved for 1 day in lipoprotein deficient medium before expression was induced with 25 ng/ml doxycycline. After another 24h in lipoprotein deficient medium, the cells were incubated for 10 minutes at 37°C with 25  $\mu\text{g}/\text{ml}$  DiI-LDL, washed and imaged for 30-60 minutes at a laser scanning microscope equipped with an Airyscan detector array (A). Location of LDL particles was extracted from the deconvoluted images (B,C) and the GFP-signal around these locations measured in the unprocessed images (D,E). Panel F shows all steps involved the process.

So for each particle that was detected at any timepoint, the GFP signal was measured in a ring shaped ROI using these dimensions. As a reference value, I calculated the local background GFP level in a 2.5  $\mu\text{m}$  radius around each LDL particle (Figure 25E) and used this to calculate the enrichment of GFP signal in immediate proximity of the LDL particles compared to this reference value. The whole workflow is shown in Figure 25F and was realized as an ImageJ macro script (see appendix). To ensure that the signal intensity in the ring ROI is not just artificially enriched over the background ROI because of measurements near the cell periphery I included measurements at random locations into the script. For this the script was run a second time but each determined particle coordinate was shifted in both x- and y-direction by a random number between -5 and +5  $\mu\text{m}$  before the GFP signal was measured in the corresponding ring and background ROIs.

The ratios of GFP signal in the ring ROIs to each corresponding background measurement is shown in Figure 26. Here, I could detect on average a ~12% increase of GFP signal in the immediate vicinity of endocytosed LDL compared to the background GFP signal. This is significantly different from the result of the same analysis at random locations, pointing towards a GRAMD1B enrichment around LDL positive endocytic vesicles. This enrichment is also significantly higher than what is observed in cells that are deficient of NPC1, indicating a role of GRAMD1B-NPC1 interaction in the recruitment. Since image acquisition using the available setup resulted in a Z-resolution that is larger than the size of the LDL containing vesicles, there was also extrafocal GFP signal detected at the exact locations of the LDL particles. By measuring the signal in the center of the ring area (0.75  $\mu\text{m}$  circle diameter), I was therefore able to also determine how much GFP-GRAMD1B is present directly above and below the LDL particles.

At these positions I found GRAMD1B to be also enriched on average by ~12% over the background, although the difference to the measurements at random locations was not significant in this case. In NPC1 cells, however, presence of GRAMD1B in this region is significantly decreased, which is in line with previous findings that NPC1 deficiency leads to a strong decrease in ER-LE/Lys contact sites [30]. Since the intensity of extrafocal signal decreases rapidly with increasing distance from the focal plane, only ~2% of the GFP signal at a distance of 0.625  $\mu\text{m}$  (outer edge of ring ROI) would be captured, while GFP at a distance of 0.375  $\mu\text{m}$  (inner ring edge) still contributes ~25% of its maximum intensity to the measurement.

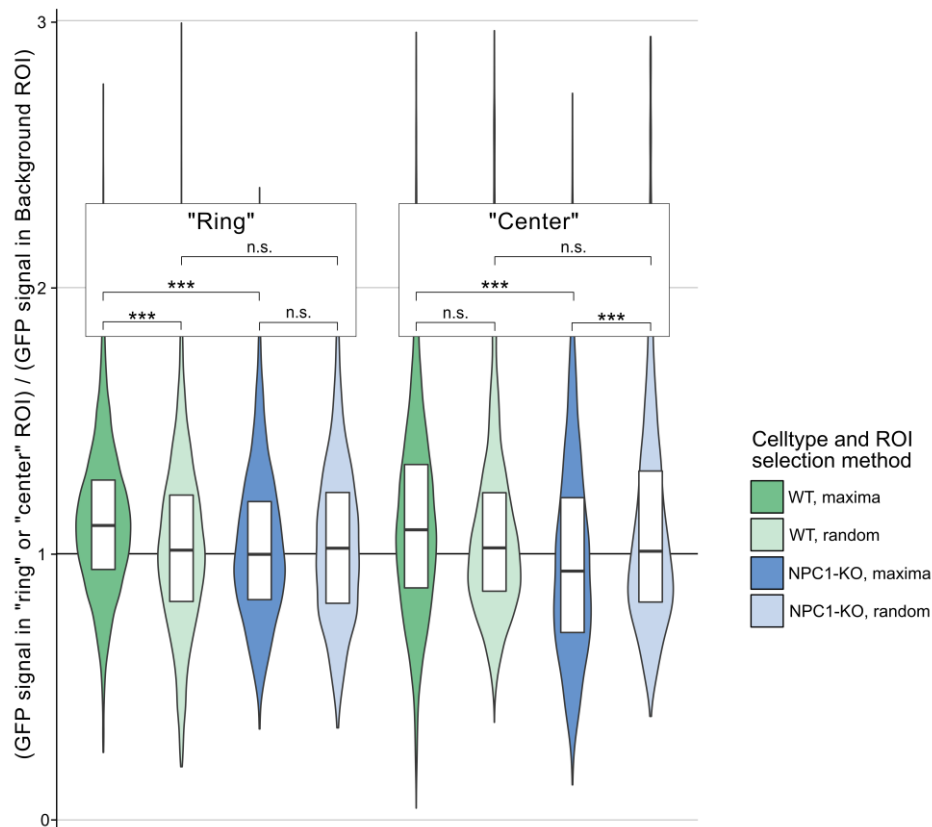


**Figure 26:** GRAMD1B enrichment around LDL particles – The GFP signal was measured at each LDL particle location in three regions of interest (ROIs): A center circle with a diameter of 0.75  $\mu\text{m}$ , a ring region with inner and outer diameters of 0.75  $\mu\text{m}$  and 1.25  $\mu\text{m}$  and a round background area with a 5  $\mu\text{m}$  diameter. Plotted are the ratios of the measurements in the center and ring ROIs, divided by each corresponding background measurement. Boxes show the median and the 25th and 75th percentile. Data groups were compared by a two-tailed heteroscedastic t-test ( $n > 5,000$ ,  $*** = p < 0.001$ ).

These values, which were estimated from a point spread function using the specifications of the imaging setup, show that GFP measurements at these center areas value closer apposition of GFP-GRAMD1B to the endosome much higher than it is in the measurements in the ring ROIs.

Altogether, these results show that GFP-GRAMD1B containing ER-tubules locate preferentially to regions that are situated in close proximity to endosomal vesicles, which contain LDL-cholesterol and that this effect is dependent on the presence of NPC1. This NPC1-dependency becomes even more apparent in measurements at the exact location of LDL particles, where GFP-signal stemming from a closely apposed or contacting ER-membrane is detected more intensely. Therefore, GRAMD1B might respond to rising levels in lysosomal cholesterol by establishing contacts through its tethering partner NPC1 in order to export lysosomal cholesterol directly to the ER.

**Table 9:** Results of the recruitment analysis of GFP-GRAMD1B to LDL particles

<b>Dataset</b>	<b>ROI</b>	<b>Median</b>	<b>25<sup>th</sup> / 75<sup>th</sup> percentile</b>	<b>Mean</b>	<b>SD</b>
WT, maxima	Ring	1.11	0.94 / 1.28	1.12	0.28
WT, random	Ring	1.01	0.82 / 1.22	1.03	0.33
NPC1-KO, maxima	Ring	0.99	0.82 / 1.20	1.02	0.28
NPC1-KO, random	Ring	1.02	0.81 / 1.23	1.03	0.30
WT, maxima	Center	1.09	0.87 / 1.33	1.12	0.37
WT, random	Center	1.02	0.86 / 1.24	1.12	0.55
NPC1-KO, maxima	Center	0.93	0.70 / 1.21	0.98	0.39
NPC1-KO, random	Center	1.01	0.82 / 1.32	1.15	0.65



### 4 Conclusion and Outlook

Proximity labelling at interfacing organellar membranes using split biotin ligases like Split-BioID, Contact-ID [52] or ideally Split-TurboID [53] provide a powerful tool to identify proteins that act at membrane contact sites. With this study it has become apparent that not only the choice of bait proteins, but also the mode of expression and the downstream processing of the biotinylated proteins has an immense impact on the specificity of the produced datasets. Therefore, additional validation of the identified hits is still necessary to verify involvement of any proteins of interest at these contact sites.

In depth analysis of the identified sterol transporter GRAMD1B and its involvement in the transport of lysosome-derived cholesterol to the ER, has revealed a potential function in lysosome-ER tethering and a direct transport of cholesterol between the contacting membranes. The results of this analysis strongly suggest that there are two different mechanisms how GRAMD1B can be recruited to cholesterol rich regions inside the cell. The first one is mediated through the sensing of PS in a cholesterol-rich environment, as it is the case for the inner leaflet of the plasma membrane when the accessible cholesterol pool is expanded [147]. Recruitment to the membrane of LDL-rich lysosomes, on the other hand, is likely facilitated through a protein-protein or protein-lipid-protein interaction with active NPC1 protein. This spatial coupling of these two major cholesterol transporters at membrane contact sites enables a potentially highly efficient route for non-vesicular cholesterol transport from lysosomes to ER. However, how much lysosomal cholesterol actually travels through this route and how much takes a detour through the plasma membrane instead is still largely unknown.

This question might be partially answered though, through a more in-depth analysis of the interaction between GRAMD1B and NPC1. To this end one might first want to identify whether the PH-like GRAM domain is also necessary for NPC1-based recruitment as it is for PS-sensing. A truncated GRAMD1B version missing its GRAM-domain was already shown to be not hampered in its sterol transport efficiency between liposomes [152] and should therefore be well suited for a comparative recruitment experiment as described here.

Additional information about the cholesterol-dependency of the observed recruitment might also be gained in a future series of follow-up experiments, by using cells with stable staining of late endosomes and lysosomes, which would allow the distinction of LDL-containing cholesterol-rich and regular endocytic vesicles. This could also shed light

## 4 Conclusion and Outlook

---

on the mechanism behind a potential pre-localization of excess GRAMD1B to Lysosome-ER contact sites, which was suggested by the results of the cholesterol esterification analysis using Lyso-pacChol. Ideally one would want to measure the recruitment of GRAMD1B to single endocytic vesicles over time, which, however, requires a more specialized imaging setup with higher temporal and spatial resolution. For this we have already gotten in contact and even run some preliminary experiments with the quantitative image processing platform hosted by the group of Prof. Helge Ewers at the Freie Universität Berlin.

Measuring a time course of GRAMD1B recruitment to lysosomes following a stimulated release of cholesterol might also be achieved using a lysosome-targeted caged cholesterol probe. This would not only allow a comparison of lysosomes with regular cholesterol levels against ones with increased levels, but could even enable imaging of the very same vesicles under both of these conditions only separated by a short flash of light to uncage the probe. While the use of these probes already provides a mean to visualize the location of lysosomes via their fluorescent coumarin cage group, it is, however, due to coumarin being prone to photo-bleaching, not possible to use this fluorescence over longer periods of time as it would be needed for recruitment studies. Yet, this might also be overcome using an alternative lysosomal staining which is compatible with this experimental setup.

Additional work is also necessary to further differentiate between the two proposed cholesterol transport mechanisms. This might be achieved using a GRAMD1B variant in the Lyso-pacCholesterol esterification assay, which is unable to be recruited to the plasma membrane because of mutations in the basic patch necessary for PS-binding [147]. In theory, this should show a similar effect as the trapping of cholesterol at the plasma membrane using ALOD4. Alternatively, the cholesterol route through the plasma membrane could be inhibited by reducing the cell's overall PS-levels via knock-down of phosphatidylserine synthase (PTDSS1), which should also result in a part of the cholesterol getting stuck in the PM due to lacking GRAMD1B recruitment [130].

The physiological purpose and the evolutionary origin of this dual function of GRAMD1B is also up for speculation. Due to the sequence homology of the START-like domain to numerous other cholesterol transporters it might be more likely that the ability to transfer cholesterol has evolved first, potentially already with a mechanism to tether to proteins in other membranes. The small group of START-like domain containing proteins with membrane tethering capabilities might have evolved only later through the addition of

## 4 Conclusion and Outlook

---

lipid-binding PH-domains. Judging from a series of mutations in the PH-domain of GRAMD1B that were shown to abolish cholesterol (R189W, conserved in yeast) or PS-sensing (K161A, R191A, only in GRAMD proteins) [147], one might argue that the ability to sense cholesterol is evolutionary conserved, while the ability to sense the coincidence of cholesterol and phosphatidylserine might have developed only in the GRAMD1 proteins of higher organisms.

Unraveling the multiple roles, which GRAMD1B seems to play in several steps of cholesterol trafficking throughout the cell and understanding how it functions in each of those roles could help us understand why this distinct function might have evolved and how big of a role it really plays in cholesterol homeostasis.



## 5 Materials and Methods

### 5.1 Reagents, Buffers and Media

Buffer or Medium	Composition
TAE	40 mM Tris, 20 mM acetic acid, 1 mM EDTA
RIPA+M	150 mM NaCl, 5 mM EDTA, pH 8.0, 50 mM Tris, pH 8.0, 1% NP-40, 0.5% sodium deoxycholate, 0.1% SDS, 1x Protease-Inhibitor Mix M (Serva)
4x Lämmli loading buffer	250 mM Tris pH 6.8, 2% SDS, 40% glycerol, 0.2% Bromphenol blue
PBS(-T)	137 mM NaCl, 2.7 mM KCl, 10 mM Na <sub>2</sub> HPO <sub>4</sub> , 1.8 mM KH <sub>2</sub> PO <sub>4</sub> (0.1% Tween)
WB transfer buffer	25 mM Tris, 192 mM glycine, pH 8.3, 20% methanol, 0.1% SDS
Streptavidin beads wash buffers 1	2% SDS
Streptavidin beads wash buffers 2	50 mM HEPES pH 7.4, 1 mM EDTA, 500 mM NaCl, 1% Triton X-100, 0.1% Na-deoxycholate
Streptavidin beads wash buffers 3	10 mM Tris pH 8, 250 mM LiCl, 1 mM EDTA, 0.5% NP-40, 0.5% Na-deoxycholate
Streptavidin beads wash buffers 4	50 mM Tris pH 7.4, 50 mM NaCl, 0.1% NP-40
Streptavidin magnetic bead elution buffer	10 mM Tris pH 7.4, 2% SDS, 5% beta-mercaptoethanol, 2 mM biotin.
TBS Buffer	50 mM Tris pH 7.6, 150 mM NaCl
Streptavidin sepharose bead elution buffer	0.4% SDS, 1% NP-40, 25 mM biotin
Colloidal Coomassie	0.02% CBB G-250, 5% (Al <sub>3</sub> SO <sub>4</sub> ) <sub>3</sub> ·18H <sub>2</sub> O, 10% EtOH, 2% H <sub>3</sub> PO <sub>4</sub> (85%)
AP-Buffer A	50 mM Tris-HCl, pH 7.5, 1mM TCEP
AP-Buffer B	AP-Buffer A + 150 mM NaCl
AP-Buffer C	AP-Buffer B + 500 mM imidazol
AP-Buffer D	AP-Buffer A with 500 mM NaCl
AP-Buffer E	AP-Buffer B + 400 µg/mL PMSF and 1x c0mplete, 1x Prot.M, DNase
SDS-lysis buffer	10 mM Tris pH 6.8, 100 mM NaCl, 1% SDS, 1 mM EDTA, 1 mM EGTA, 20 mg/ml PMSF)
Imaging medium	DMEM-D1145 (Sigma) supplemented with 4 mM L-Glutamine, 10 mM HEPES, 1 mM Sodium pyruvate
Imaging Buffer	20 mM HEPES, 115 mM NaCl, 1.2 mM MgCl <sub>2</sub> , 1.2 mM K <sub>2</sub> HPO <sub>4</sub> , 11 mM glucose, 1.8 mM CaCl <sub>2</sub> pH 7.4

## 5.2 Plasmids and Primers

### 5.2.1 Plasmids

Internal Number	Vector and Insert Name	Origin
p002	pSF3_CBir-linker-FRB_FKBP-linker-NBir	J. Béthune
p012	p_myc-PTN1	E. Eden
p014	p_EGFR	E. Eden
p019	pEGFPC1-hVAP-A	F. Alpy
p021	pEGFPC1-hVAP-B	F. Alpy
p023	pCl-neo-RMD3-HA	C. Miller
p046	p_STARD3-GFP_R117Q	D. Höglinger
p034	pSF3_CBir-linker-VapA_STARD3-R117Q-linker-NBir	V. Schoop
p035	pSF3_CBir-linker-VapB_RMD3-linker-NBir	V. Schoop
p049	pSF3_CBir-linker-PTP1B_EGFR-linker-NBir	V. Schoop
p053	pSF3_myc-BioID-Rab11a+Luciferase	J. Béthune
p058	pSF3_STARD3_R117Q-BirA	V. Schoop
p059	pSF3_RMD3-BirA	V. Schoop
p060	pSF3_BirA-VapA	V. Schoop
p061	pSF3_BirA-VapB	V. Schoop
p062	pSF3_BirA-PTP1B	V. Schoop
p066	pSF3_EGFR-BirA	V. Schoop
p056	pPGK_FLP-obpA	J. Béthune
p087	pcDNA6.2-N-V5-Lumio_MAVS	R. Bartschlager
p089	pEGFP_MAVS	V. Schoop
p072	pSpCas9(BB)-2A-GFP(PX458)	J. Béthune
p109	pSpCas9(BB)-2A-GFP(PX458)_NPC1-ex2	V. Schoop
p048	pEGFP_GRAMD1B	D. Höglinger
p140	pSF3_GFP-GRAMD1B	V. Schoop
p198	pRSET-B_His-FLAG-ALOD4	A. Radhakrishnan
p199	pRSET-B_His-FLAG-ALOD4-Mut	A. Radhakrishnan

Plasmid maps are available under the link provided in the Appendix section.

### 5.2.2 DNA oligonucleotides

Cloning PCR Primers			
Internal Number	Target	Feature overhang	Sequence
#04	PTPIP_fwd	Clal	agctaatacgatATGTCTAGACTGGGAGCCCTGG
#05	PTPIP_rev	Mlul	ccgccacgcgtGTCTCGTAAAATGACTTCCAGTTCTTCCAGG
#06	VAPA_fwd	PmeI	cgtttgtttaaacATGGCGTCCGCCCTCAGG
#07	VAPA_rev	Pacl	gctatттаattaactgCTACAAGATGAATTTCCCTAGAAAAGAATC CAATGAAAATGGC
#08	PTP1B_fwd	PmeI	cgtttgtttaaacATGGAGATGGAAAAGGAGTTCGAGC
#09	PTP1B_rev	Pacl	gctatттаattaactgCTATGTGTTGCTGTTGAACAGGAACC
#10	EGFR_fwd	AclI	agctaaacgttATGCGACCTCCGGGAC
#12	STARD3_fwd	Clal	agctaatacgatATGAGCAAGCTGCCCAGG
#13	STARD3_rev	Mlul	ccgccacgcgtCGCCCGGGCCCC
#14	EGFR_rev	Mlul	ccgccacgcgtTGCTCCAATAAATTCACTGCTTTGTGGC
#15	VAPB_fwd	PmeI	cgtttgtttaaacATGGCGAAGGTGGAGCAGG
#16	VAPB_rev	Pacl	gctatттаattaactgCTACAAGGCAATCTTCCAATAATTACACCAA C
#60	PTP1B_fwd	Mlul-3xGS	agaagACGCGTggtagcggcagcggtagcATGGAGATGGAAAAG GAGTTCGAGCagatc
#61	PTP1B_rev	NotI	cttttGCGGCCGCCTATGTGTTGCTGTTGAACAGGAACCTG TAGC
#62	VapA_fwd	Mlul-3xGS	agaagACGCGTggtagcggcagcggtagcGCGTCCGCCTCAGGg gccaatggcgaagcac
#63	VapA_rev	NotI	cttttGCGGCCGCCTACAAGATGAATTTCCCTAGAAAAGAAT CCAATG
#64	VapB_fwd	Mlu-3xGS-	agaagACGCGTggtagcggcagcggtagcATGGCGAAGGTGGA GCAGGTCCCTGAGCCTCG
#65	VapB_rev	NotI	cttttGCGGCCGCCTACAAGGCAATCTTCCAATAATTACA CCAAC
#66	Myc-BirA*_fwd	Mlul	gggcgACGCGTggtagcggcagcggtagcGAACAAAACTCAT CTCAGAAGAGGATCTCGAC
#67	BirA*_rev	BamHI	ggtctGGATCctcaCTTCTCTGCGCTTCTCAGGGAGATTTTC TC

Guide RNA template		
Internal Number	Genomic Target	Sequence
AT01	NPC1_ex2_aa36-42_fwd	CACCgAGGTACAATTGCGAATATTC
AT02	NPC1_ex2_aa36-42_rev	AAACGAATATTCGCAATTGTACCTC

## 5 Materials and Methods - 5.3 Antibodies

Genomic PCR primers		
Internal Number	Genomic Target	Sequence
cr39	Chr18_NPC1_ex2_fwd	CAGGGGACAAGGACGTCAAA
cr40	Chr18_NPC1_ex2_rev	CCTCCCCTCCGCTGAATTTT
#248	11ht-integration-site_fwd	TCCTGCTCGAACAGCTCC
#249	11ht-integration-site_rev	AGATCCTCGTTATTAATCGC

qPCR primers		
Internal Number	mRNA Target	Sequence
#151	NPC1_ex2_aa36-42_fwd	ggggacaagaggtacaattgcg
#152	NPC1_ex2_aa83-89_rev	gcagctgcaggttgtcttttag
#333	GAPDH_fwd	GTCTCCTCTGACTTCAACAGCG
#334	GAPDH_rev	ACCACCCTGTTGCTGTAGCCAA

### 5.3 Antibodies

Antigen	Host / Class	Manufacturer	Dilution
GRAMD1B	Rabbit / Polyclonal	Proteintech, 24905	WB) 1:500
FLAG	Mouse / Monoclonal	Sigma, F3165	WB) 1:1,000, IF) 1:100
DDRGK1	Rabbit / Polyclonal	Sigma, HPA013705	WB) 1:1,000
ACBD5	Rabbit / Polyclonal	Sigma, HPA012145	WB) 1:1,000
GFP	Rabbit / Polyclonal	Proteintech, 66002	WB) 1:1,000, IF) 1:100
Biotin (Streptavidin)	- / -	Thermofisher, 21848	WB) 1:15,000, IF) 1:1,500

### 5.4 DNA extraction, amplification and cloning

Plasmid DNA was purified from 5 ml or 100 ml bacterial cultures in LB medium supplemented with antibiotics (100 µg/ml Ampicillin or 50 µg/ml Kanamycin) using a Miniprep or Midiprep DNA extraction kit (GenElute, Sigma) according to the manufacturer's guidelines. Genomic DNA was extracted using a DNeasy Blood & Tissue Kit (Qiagen) according to the manufacturer's guidelines.

DNA amplification using polymerase chain reaction was performed using Q5 HF-DNA Polymerase (NEB), with concentrations and thermocycler (Applied Biosystems Veriti) protocols according to the manufacturer's guidelines. Annealing temperatures were calculated using [tmcalculator.neb.com](http://tmcalculator.neb.com). PCR products were run on 1% agarose gels in TAE buffer containing MidoriGreen DNA stain at 120V (PEQLAB chamber 40-0708). DNA bands were visualized using UV light in a BioRad Gel Doc XR+ system, excised and purified using an extraction kit (FastGene Gel/PCR Extraction Kit, Nippon Genetics). Concentrations were measured at a NanoDrop ND-1000 spectrophotometer.

Cloning of PCR products into plasmids was done using restriction enzymes (NEB) to produce sticky ends in PCR products and plasmid backbones. Digest was done according to the manufacturer's guidelines of the used enzymes. Plasmid backbones were separated from inserts and purified via band extraction from agarose gels. Reaction mixes for ligation of digested PCR products into the plasmid backbones was calculated using [nebiocalculator.neb.com/#!/ligation](http://nebiocalculator.neb.com/#!/ligation) with a standard ratio of 3:1. Ligation reactions were performed using T4 DNA ligase (NEB) at 16°C over night, followed by heat inactivation for 20 min at 65°C.

Standard transformation was performed by mixing 50 µl of chemically competent *E. coli* cells (NEB, DH5α/10β/BL21) with 1 µl of plasmid DNA or 10 µl of ligation mix and incubated on ice for 20 minutes before a 45 second heat shock at 42°C. Cells were then immediately cooled on ice for 5 minutes before rescued by the addition of 950 µl warmed SOC medium (NEB) and incubation at 37°C for 1 hour. Cells were then pelleted at 13,000 x g, streaked onto LB plates containing antibiotics for selection (100 µg/ml Ampicillin or 50 µg/ml Kanamycin) and grown over night at 37°C.

### 5.5 Quantitative RT-PCR

Primers for qPCR were designed using [ncbi.nlm.nih.gov/tools/primer-blast/](http://ncbi.nlm.nih.gov/tools/primer-blast/) against the human Refseq mRNA database with a target length of 70-200 bp and an optimal melting

temperature of 60°C. RNA was extracted from HeLa cells grown in 6-well plates, using TRI reagent (Sigma T9424) and Direct-zol RNA MiniPrep kit (Zymo research) as described in the manufacturer's guidelines. RNA concentrations were measured at a NanoDrop ND-1000 photometer and 500-100 ng used for cDNA synthesis with the RevertAid First Strand cDNA Synthesis Kit (ThermoFisher) as described in the user guide. PCR reaction mixes using a SYBR green containing reaction mastermix (NEB, M3003S) and GAPDH primers (#333 and #334) as internal standard were prepared as described in the manufacturers guidelines. Reaction was run in a StepOnePlus Real-Time PCR thermocycler (Applied Biosystems) using the preset standard reaction protocol (~2h). Measured Ct values were first standardized to the corresponding GAPDH sample and then to the experimental control condition.

### 5.6 Cultivation of human cell lines

All human cells were grown in Dulbecco's Modified Eagle's Medium (DMEM) - high glucose (D6429, Sigma), supplemented with 10% fetal bovine serum (Sigma or Bio&Cell) and 170 µM penicillin and 137 µM streptomycin (Biowest, L0022) at 37°C with 5% CO<sub>2</sub> (hereinafter referred to as complete medium and standard conditions). Used culture vessels included 25/75 mL canted neck flasks, 10/15 cm vented round dishes and 6/12/24/48/96-well plates made of polystyrene with tissue culture treated surface by Greiner or Sarstedt. Dissociation of adherent cells for propagation or harvest was performed by incubation for 3-5 minutes with trypsin solution (Gibco, 25300-054), followed by resuspension in fresh FBS supplemented DMEM to quench protease activity.

### 5.7 Generation of stable cell lines

Knock-in cell lines were generated using the protocol described in Schopp et al. HeLa 11ht wt cells containing a stably integrated Hygromycin-TK cassette, flanked by flippase recognition target sites (FRT) were generated by I. Weidenfeld allowing for easy targeted knock-ins. This cell line also constitutively expresses the tetracycline controlled transcription activator rtTA-M2 necessary for doxycycline-inducible gene expression (Tet-On system). All constructs for genomic integration (p34, p35, p49, p58, p59, p60, p61, p62, p66, p140) were cloned into the pSF3 vector backbone containing the FRT sites necessary for FLP-recombinase mediated cassette exchange as well as a bidirectional tetracycline-responsive promoter [204].

HeLa 11ht wt cells were grown in complete medium, as described above, supplemented with 200 µg/mL HygromycinB (Sigma). For stable cell line generation, cells were seeded in medium without HygromycinB at a concentration of  $10^5$  cells per well in a six-well plate. After 20-24h polyethylenimine (PEI 25K, Polysciences Inc.) was used to co-transfect the cells with the pSF3 plasmid of choice and the Flp coding plasmid pPGK-FLP-obpA (p056, addgene 13793). Per 1 ml of culture medium, 1 µg of DNA was mixed with 2 µg of PEI (1 mg/mL stock) in 100 µl OptiMEM (Gibco), incubated at room temperature for 15 min and added dropwise to the cells. Day 1 after transfection the cells were transferred to a 10 cm dish and after another 2 days, 50 µM Ganciclovir (Sigma) was added to the medium to start selection. If necessary, the cells were further diluted to allow formation of single colonies, which were picked after one week in selection medium using 3.2 mm cloning discs (Sigma). Picked cells were propagated in ganciclovir containing medium for 3 weeks total before being tested for successful genomic integration via western blotting or (immuno-) fluorescence microscopy.

### 5.8 Generation of NPC1-KO cell line

Knock-out of NPC1 in HeLa 11ht cells was performed using the CRISPR/Cas9 and a guide RNA targeted at exon 2, which had been used previously by Tharkeshwar et al. [205]. This target was chosen to match this cell line to a second NPC1<sup>-/-</sup> cell line that had already been used in our laboratory.

The template for the guide RNA was ordered as two complementary DNA oligonucleotides (AT01, AT02) with 5' extensions for cloning into a plasmid containing a GFP-tagged Cas9 and the necessary gRNA scaffold under a U6 promoter (plasmid was a gift from J. Béthune, p072). Oligonucleotides were end-phosphorylated for 30 minutes at 37°C using polynucleotidkinase (NEB) in T4 ligase buffer and then annealed by heating to 95°C and slowly decreasing the temperature by 5°C/min down to 25°C.

The Cas9 plasmid was digested using BbsI (NEB) to create matching 5' overhangs and then dephosphorylated for 30 min at 37°C by the addition of Shrimp Alkaline Phosphatase (rSAP, NEB). The plasmid backbone was then purified from an agarose gel, mixed with the phosphorylated oligonucleotide duplex (50 ng plasmid, molar excess of insert ~5:1) and ligated using T4 DNA ligase (NEB). After transformation in *E. coli* and plasmid purification, correct insertion was checked by DNA sequencing.

HeLa 11ht were first seeded in a T75 flask and when growth had reached exponential phase the medium was removed, sterile filtered and stored as quorum sensing medium. Cells were then seeded into a 6-well plate and transfected the next day with the GFP-Cas9 plasmid containing the NPC1 gRNA sequence (p109). After 3 days, the cells were harvested, pelleted, resuspended in serum free DMEM without antibiotics and pipetted into a flow cytometry tube through a strainer cap to catch cell clumps. Flow cytometry was performed by Monika Langlotz at the Heidelberg University core facility. Positively transfected cells were identified based on GFP signal intensity and sorted as single cells into a 96-well plate containing the previously collected quorum sensing medium. Clonal cell lines were then grown and expanded until successful knock-outs could be verified by sequencing of the targeted genomic locus (amplification using primers cr39 + cr40, sequencing with cr39), western blot analysis and qPCR (primers #151 + #152).

### 5.9 Cell lysis

Unless stated otherwise human cells were always lysed by resuspension in cold RIPA+M buffer, followed by 20 minutes incubation on ice. Residual cell clumps were then dissolved using an ultrasonic bath (Bandelin Sonorex) for three times 3 seconds, cooling on ice in between intervals. After another 20 minutes incubation on ice, insoluble cell debris was pelleted at 21,000 x g, 4°C for 5 minutes and the supernatant transferred to a new tube.

### 5.10 Protein concentration measurements

For protein concentration measurements using the Amido Black assay, 100 µL of diluted cell lysate or protein solution was mixed with 400 µL of Amido Black solution (1g/L in MeOH:AcOH 9:1, Serva) and incubated at room temperature for 15 minutes. After centrifugation for 5 minutes at 21,000 x g and removal of the supernatant, the precipitate was washed two times with 500 µl of wash solution (MeOH:AcOH, 9:1), centrifuging 5 minutes at 21,000 x g in between. The washed pellets were then dissolved in 300 µl NaOH (0.1 M) and 150 µL of it added to a clear bottom 96-well plate to measure the absorbance at 550 nm in a platereader (Spectramax M5, Molecular Devices). Concentrations were calculated by including dilute BSA solutions at concentrations up to 100 µg/ml for the generation of a standard curve.

### 5.11 Western blot analysis

Protein samples were boiled for 5 minutes at 98°C in 1x Lämmli sample buffer, centrifuged for 1 minute at 21,000 x g and loaded on Invitrogen NuPAGE 4 to 12%, Bis-Tris, 1.0 mm, Mini Protein Gels (Thermo Scientific, NP0321/NP0323). Gels were run in an Invitrogen XCell SureLock Mini-Cell Electrophoresis System (Thermo Scientific, EI0001) in NuPAGE MOPS SDS-Running Buffer (Thermo Scientific, NP000102) for 5 minutes at 100 V to concentrate the sample and then 45 min at 200 V for separation. Gels were briefly rinsed in water and sandwiched between Whatman blotting paper and a PVDF membrane (Immobilon) soaked in 1x WB transfer buffer. Protein transfer was achieved using an XCell II Blot Module (Thermo Scientific, EI9051) according to the manufacturer's guidelines and blotting at 30V for 90 min at room temperature. The membrane was washed for 5 min in PBST and blocked for 30 min in 5% milk powder (Roth) dissolved in PBST. After washing 3 times for 5 minutes, the membrane was incubated over night at 4°C with the primary antibody diluted in 2% BSA (Sigma) in PBST. The membrane was then washed 3 times for 5 minutes before incubated with the fluorescent secondary antibody (IRDye 680/800 (LICOR), diluted in 2% BSA in PBST) for 30 minutes at room temperature. Blots were then washed 3 times with PBST and once with PBS and imaged on a LICOR Odyssey 9120 infrared imaging system.

### 5.12 Immunofluorescence staining

Cells were grown in 24-well plates on round glass coverslips. For immunological staining, the adherent cells were washed 3 times for 5 minutes on a rocking plate with PBS at room temperature before fixation in freshly thawed 4% paraformaldehyde (PFA, Electron Microscopy Sciences) in PBS for 1 hour. Cells were then washed 3 times for 5 minutes with PBS and remaining PFA quenched with 1.5 mg/ml glycine in PBS for 15 minutes. After washing with PBS, the primary antibody (diluted in 1% BSA, 0.3% Triton in PBS) was added to the cells for 1-2 hours. Primary antibody was then washed out 3 times with PBS and the fluorescent secondary antibodies added (Cell Signalling, diluted 1:1000 in 1% BSA, 0.3% Triton in PBS). After incubation for 30 minutes at room temperature, the secondary antibody was washed out 3 times for 5 min with PBS and the coverslips carefully blotted dry. The coverslips were then mounted on Menzel glass slides (Thermo Scientific) using Prolong Gold Antifade medium (Thermo Scientific, P10144) and allowed to cure overnight.

### 5.13 Fluorescence microscopy

Fixed and live cells were imaged on a confocal laser scanning microscope (Zeiss LSM 800), equipped with excitation lasers at 405/488/561/640 nm, Colibri LEDs, a Zeiss Airyscan detector array and a definite focus module. Images and videos were acquired using a Plan-Apochromat 63x/1,4 Oil DIC M27 objective.

### 5.14 SplitBioID experiments

#### 5.14.1 Cloning of BioID constructs

Tetracycline inducible pSF3 plasmids containing Split-BioID constructs of FRB and FKBP (p001-p004) were a gift from Isabel Schopp and Julien Béthune. VAP-A and VAP-B plasmids were a gift from Fabien Alpy. STARD3, EGFR and PTP1B plasmids were a Gift from Emily Eden. RMD3 plasmid was a gift from Christopher Miller. All proteins were tagged with the BirA\* fragments at the cytosolic terminus, with the smaller fragment (CBirA\*) on the smaller protein of the tether pair. Insertion of the constructs into p002 was achieved by classical restriction cloning using primer pairs #4/#5, #6/#7, #8/#9, #10/#14, #12/13 and #15/#16.

This resulted in the constructs CBirA\*-VAPA+STARD3-NBirA\*, CBirA\*-VAPB+RMD3-NBirA\* and CBirA\*-PTP1B+EGFR-NBirA\* (p34, p35, p49).

Non-split BioID constructs of the N-terminally tagged proteins (VAPA, VAPB, PTP1B) were cloned by first removing the luciferase gene from p053 (pSF3\_myc-BioID-Rab11a+Luciferase), followed by replacement of Rab11a with VAP-A (#62/#63), VAP-B (#64/#65) or PTP1B (#60/#61) resulting in the plasmids p060-062. For C-terminal tagging of STARD3, RMD3 and EGFR, first the CBirA\*- tagged protein sequences were removed from p34, p35 and p49, followed by replacement of NBirA\* by full length BirA\* from p053 (#66/#67).

#### 5.14.2 Biotinylation screening

Initially the ability of the constructs to successfully reassemble and release active biotin-AMP was tested. Therefore HeLa 11ht wt cells were seeded into the wells of a six-well plate the day before transfection with the Split-BioID plasmids (p002, p034, p035, p049). Transfection was performed using ViromerRed according to manufacturer's instructions at a final concentration of 1 µg DNA per 1 mL medium. After 20-24h

Doxycycline was added at a concentration of 200 ng/mL (10 mg/mL stock in 70% EtOH) to induce expression alongside with 50  $\mu$ M biotin (50 mM stock in DMSO). For the positive control containing FRB and FKBP (p002), 100 nM rapamycin was also added in order to induce dimerization. Cells were harvested after 24 h, lysed in RIPA buffer, subjected to western blot analysis and visualized on a LI-COR Odyssey imager using DyLight680-Streptavidin at a dilution of 1:15,000.

### 5.14.3 Split-BioID assay for proteomic analysis

For large scale expression and biotinylation HeLa 11ht wt cells or previously generated stable cells were seeded in 15 cm dishes at a density of  $10^6$  cells in complete medium prepared with tetracycline-free FBS (Biowest). For transient expression of BioID constructs, cells were transfected after two days using PEI. Expression was induced by the addition of doxycycline in all cells three days after seeding using 25 ng/ml for stable cell lines and 100 ng/ml for transfected cells. After allowing expression and biotinylation for 24h, cells were harvested using 1.5 ml trypsin solution per dish and resuspended in 5 ml medium. Cells were pelleted at 500 x g for 5 min, lysed in 1 ml RIPA+M buffer per 15 cm dish and the protein concentration determined using the Amido Black assay. Pulldown samples for proteomic analysis were initially generated using magnetic beads coupled to streptavidin (hyBeads by Hyglos GmbH, discontinued) and were measured at FingerPrint Proteomics at the University of Dundee. Due to discontinuation of the beads and changes in the sample handling policies of the proteomics facility in Dundee, further biotin pull down assays were performed using a different brand of magnetic streptavidin coupled beads (NEB, cat# S1420S) and measured at the mass spectrometry core facility of the University of Heidelberg. For Split-BioID experiments in collaboration with the lab of Christian Freund at Freie Universität Berlin, streptavidin coupled to sepharose beads (GE, cat# 17-5113-01) was used and samples measured at their facility in Berlin.

For the pulldown, streptavidin beads (70  $\mu$ l of magnetic or 17  $\mu$ l of sepharose beads per 1 mg of protein) were washed two times for 5 min and equilibrated for 1h in RIPA Buffer, before 3.5-5 mg of protein, diluted to 1.5 ml, was added to the beads. Beads and cell lysates were incubated on a rotary wheel over night at 4°C to allow binding. The supernatant was removed from the beads, stored and labelled as flowthrough. Beads were taken up and washed two times with 1 ml of wash buffer for 10 minutes on a rotary wheel. This was repeated with four different wash buffers to minimize unspecific binding.

For measurements at the HD core facility, NP-40 was omitted from all wash buffers. Biotinylated proteins were then eluted by boiling the beads for 15 min at 98°C in 30 µl of their respective elution buffer (see section 5.1). Eluted samples were loaded on SDS-gels and run until migrated into the gel for 1-2 cm. After staining overnight with colloidal Coomassie solution [206], the whole lane was cut from the gel, excluding the strong Streptavidin band at ~17kDa. Excised gel pieces were then sent for proteomic analysis.

### 5.14.4 Immunoblot analysis of proteins of interest

Split-BioID cell lysates were produced as described in the previous paragraph. Biotin pulldown was performed by incubating 5 mg of total protein lysate with 350 mg streptavidin coupled sepharose beads (GE, cat# 17-5113-01, equilibrated in TBS) overnight on a rotary wheel. The supernatant was removed and the beads washed 4 times for 5 minutes with TBS at room temperature, centrifuging for 1 minute at 500 x g in between washes. Proteins were eluted in 30 µl Streptavidin sepharose bead elution buffer (0.4% SDS, 1% NP-40, 25 mM biotin) by incubation at 95°C for 15 minutes. Supernatant was taken off the beads, mixed with 4x Lämmli sample buffer, concentrated down to <20 µl at 95°C in a tube with open lid and subjected to western blot analysis.

### 5.14.5 LC-MS/MS measurements

First MS screening was performed by Fingerprint proteomics at the University of Dundee. The samples were loaded (15 ml injection volume) on an Ultimate 3000 RSLCnano liquid chromatography system (Thermo Scientific, running dual column set-up) coupled to a LTQ Orbitrap Velos Pro (Thermo Scientific). The peptides were initially trapped on an Acclaim PepMap 100 (C18, 100 mM x 2 cm) trap column, and then separated on an Acclaim PepMap RSLC C18 column (75 mM x 50 cm) followed.

The second mass spectroscopic measurement was performed at the Core Facility for Mass Spectrometry and Proteomics (CFMP) in the Zentrum für Molekulare Biologie at Heidelberg University. Here peptides were separated on an in-house packed C18 reversed-phase column of 25 cm length using a 60 min gradient from 3% to 36% ACN and directly injected to an Q-Exactive HF mass spectrometer.

The third screening was performed by Benno Kuroepka in the group of Prof. Christian Freund at Freie Universität Berlin. The samples were loaded on an Ultimate 3000 NCS-3500RS Nano liquid chromatography system coupled to a Orbitrap Q Exactive HF.

The peptides were initially trapped on an Acclaim PepMap 100 (C18, 3  $\mu\text{m}$ , 100 $\text{\AA}$ , nanoViper, Thermo #164535) trap column, and then separated on an Acclaim PepMap RSL C18 column 2  $\mu\text{m}$ , 100 $\text{\AA}$ , nanoViper (Thermo #164941).

### 5.14.6 Analysis of mass spectrometric data

Raw data provided by the proteomic facilities were analyzed in MaxQuant v1.6.1. Identified masses were searched against the Uniprot-human database (downloaded March 2018) using the built-in Andromeda search engine. The protein database was extended by a list of common contaminants and reverse sequences of all entries.

Variable modifications to include in the search were lysine biotinylation, N-terminal acetylation and methionine oxidation. Carbamidomethyl cysteine modification was included as a fixed modification. Minimal peptide length required for identification was set to 7, the maximum amount of missed cleavages to 2 and the false discovery rate to 0.01. Quantification of proteins was done without labels (label-free quantification, LFQ) with a minimum ratio count of two and the “match between run” option enabled.

The resulting list of proteins was then processed using Perseus v1.6.1 where common contaminants were removed alongside proteins, which were only identified by their reverse sequence or via a modification. LFQ values were logarithmized (base2) and for proteins that were not identified in all of the samples, the missing values were imputed using random values from a normal distribution to simulate low abundance values. Samples were searched for significant enrichment over an unspecific BioID dataset. In the first proteomic screen the control dataset stemmed from previous BioID assays performed by Isabel Schopp and Julien Béthune [51] which used GRASP65, TGN38 and Ago2 as bait proteins and were measured at the same facility. In the second and third screen measured at Heidelberg and Berlin, the control sample was using Ago2 as bait protein and created in parallel to the Split-BioID samples. For statistical analysis LFQ-values were tested against the control using permutation-based FDR statistics (two-sample t-test, 250 permutations; FDR=0.05;  $s_0=0.1$ ). Protein enrichment over the control sample was plotted against each corresponding p-value, in a volcano plot. A sensible threshold was selected by adjusting the FDR and  $s_0$  values and all hits above it were considered significant. Additionally, hits that were not found at least 2-fold enriched over the negative control were filtered out (>2-fold enriched in both replicates for screen 1 and 2, average of three replicates >2-fold enriched for screen 3). GO-term annotation

and comparison with other proteomic datasets was performed using the software FunRich v3.1.3.

### 5.15 Lyso-pacCholesterol esterification assays

HeLa 11ht cells were seeded into 12-well plates, grown for 1 day until 80-90% confluent. Cells were then incubated for 30 minutes with 300  $\mu$ L of 10  $\mu$ M Lyso-pacChol (10 mM stock in DMSO) in warmed DMEM high glucose complete medium. After washing two times with PBS, fresh medium was added to the wells. For overexpression of GFP-GRAMD1B 200 ng/mL Doxycycline (10  $\mu$ M stock in 70% EtOH) was added to the fresh medium. After 16-18h the medium was replaced with 350  $\mu$ L imaging buffer and cells were illuminated for 60 seconds under a UV lamp (nailstar professional, NS-02B-EU) to uncage the Lyso-pacChol. Imaging buffer was replaced with fresh medium and the cells placed back into the incubator. After 0-120 minutes of chase durations the cells were harvested using trypsination for 2 minutes and quickly taken up with ice-cold PBS to reduce prolonging of the chase durations. The cells were then pelleted for 5 minutes at 500 x g, resuspended in 300  $\mu$ L cold PBS and lysed by the addition of 600  $\mu$ L MeOH and 150  $\mu$ L CHCl<sub>3</sub>. For lipid extraction, all insoluble cell fragments were pelleted for 5 minutes at 21,000 x g and the supernatant mixed with 600  $\mu$ L NaCl (0.9% w/v) and 300  $\mu$ L CHCl<sub>3</sub> in a new tube. After 10 seconds of vigorous mixing using a vortexer the aqueous and organic phases were separated by centrifuging for 5 minutes at 21,000 x g. After discarding the upper aqueous phase, the organic phase was transferred to a new tube and dried in a vacuum concentrator at 30°C for 20 minutes.

In order to allow visualization on a TLC plate, a hydroxycoumarin click handle was attached to the extracted Lyso-pacChol. For the click reaction mixture 500  $\mu$ L EtOH was mixed with 125  $\mu$ L of CuBF<sub>4</sub> solution (10 mM in ACN) and 0.6  $\mu$ L 3-azido-7-hydroxycoumarin (44.5 mM in EtOH, Carl Roth). The extracted and dried lipids were dissolved in 30  $\mu$ L click mixture and allowed to react at 45°C in a speed vac for 20 minutes until dry, taken up in 15  $\mu$ L EtOH/CAN (5:1) and spotted on an Silica Aluminum plate (Supelco, Silica Gel 60). After letting the spots dry for 15 min, the TLC was run in solvent 1 (CHCl<sub>3</sub>/MeOH/H<sub>2</sub>O/AcOH, 65:25:4:1) until 2 cm above the start line, dried for 30 minutes and then run in solvent 2 (cyclohexane/ethylacetate, 60:40) to a height of 12 cm. The plates were then dried and imaged on a BioRad GelDoc XR+ using the built-in bottom UV illumination and mirrors at a <45° angle to redirect the light onto the plate.

### 5.15.1 Lyso-pacCholesterol esterification assays in the presence of ALOD4

Prior to uncaging under the UV lamp, cells were incubated for 60 minutes at 37°C with 3 µM ALOD4 in fresh DMEM. The ALOD4 containing medium was then replaced with imaging buffer for the uncaging step and added back afterwards for the chase periods. Lipid extraction and analysis was performed as previously described.

## 5.16 Expression, purification and evaluation of ALOD4

Expression and purification of recombinant ALOD4 and the cholesterol binding mutant ALOD4-Mut was performed mostly as described in Endapally et al. 2019 [201]. Expression plasmids were kindly gifted by Arun Radhakrishna (p198, p199, Addgene plasmids #111026 and #111027) [76]. The plasmids contain the sequences for domain 4 of Anthrolysin O (amino acids 404–512) with mutations that enable site specific maleimide labelling (S404C and C472A) and in case of ALOD4-Mut additional mutations that abolish cholesterol binding (G501A, T502A, T503A, L504A, Y505A, P506A). Sequences are controlled by an inducible T7 promoter and are preceded by a hexahistidine-tag for purification and a FLAG antigen sequence (DYKDDDDK).

### 5.16.1 Expression of ALOD4

Expression pre-cultures in 5 ml LB-Amp were inoculated from colonies or glycerol stocks (pAR1 or pAR2 in *E. coli* BL21) and incubated over night at 37°C. From this culture a second pre-culture in 50 ml LB-Amp was inoculated in a 200 ml baffled flask at an OD<sub>600</sub>= 0.2. The culture was grown at 37°C at 180 rpm shaking to OD<sub>600</sub>= 0.8-1.0 and used to inoculate the main expression culture in 2 L warmed LB-Amp (2x 1L in 5 L baffled flasks) to an OD<sub>600</sub> of 0.01. Cells were grown at 37°C, 180 rpm shaking until OD<sub>600</sub>= 0.4-0.6 before the incubator temperature was shifted to 18°C. After 1h of cooling (OD<sub>600</sub>= 0.8-1.0) the expression was induced by the addition of 1mM IPTG (Sigma, 1M stock in water) and the culture incubated overnight at 18°C, 180 rpm shaking. Bacteria were harvested by centrifugation (30 min at 6,000 rpm, 4°C, Sorvall Evolution RC, SLC 6000), resuspended in 80 ml ALOD4-Purification Buffer B (AP-BufferB), transferred to two 50 ml tubes, pelleted and frozen in liquid nitrogen until needed.

### 5.16.2 Purification of ALOD4

Cell pellets were thawed on ice, resuspended in 40 ml cold AP-Buffer E and lysed on a French press (Microfluidics-110L) at 15,000 psi. Lysates were cleared by centrifugation (40 min at 40,000 x g, 4°C, Beckmann Optima LE-80K, 50.2 TI), passed through a 0.22 µm filter and incubated with 5 ml Ni-NTA beads (10 ml slurry, column volume = 5 ml, PureCube Ni-NTA Agarose, equilibrated with 2x 25 ml AB-Buffer B) over night at 4°C rolling. Supernatant (labelled as “FT”) was removed after centrifuging at 100 x g for 1 min and the beads washed with 5 column volumes (CV) low salt buffer (AP-Buffer B), followed by a high salt wash (5 CV of AP-Buffer D) and three washes with 3 CV each of low imidazole buffer (50 mM = 10% AP-Buffer C in AP-Buffer B). The beads were then loaded onto a gravity column (Thermo Scientific, 29924) with a flow rate of ~ 0.5 ml/min for the following elution steps. Elution was realized with a makeshift imidazole gradient with a range of 75 – 300 mM over 12 column volumes (15/20/30/40/50/60% AP-Buffer C in AP-Buffer B) and sample collection in 2 ml fractions. Collected samples from all steps (Lysate, FT, washes and elution fractions) were analyzed by SDS-PAGE and coomassie staining. Fractions with the highest concentrations of a band at the correct height (15,6 kDa, peak elution at ~100-150 mM imidazole) were pooled. The sample was then concentrated to a volume of less than 5 ml (Amicon Ultra-15, 10 kDa cutoff, 4000 x g) and diluted with salt-free AP-Buffer A to a volume of 50 ml to reduce NaCl concentration to ~15 mM.

Diluted protein was filled into a 50 ml Superloop and connected to a Cytiva ÄKTAprime plus FPLC system equipped with 1 ml anion exchange column (HiTrap Q). The column was washed with H<sub>2</sub>O and equilibrated with 10 CV of AP-Buffer A. Protein sample was loaded from the Superloop to the column (flow rate 0.5 ml/min), followed by a 10 CV wash with AP-Buffer A and elution with a 0-500 mM NaCl gradient over 5 CV. Eluted protein was collected in 1 ml fractions and subjected to SDS-PAGE analysis. The best three fractions were pooled and further purified by size exclusion chromatography (SEC) using a dextran-agarose column with a volume of 120 ml (16/600 Superdex 75). The column was washed with H<sub>2</sub>O and equilibrated in 1 CV of AP-Buffer B (flowrate 1 ml/min). The pooled protein sample was loaded onto the column from a 5 ml loop and separated by running the column with 1 CV of AP-Buffer B and sample collection in 2 ml fractions. After SDS-PAGE analysis, protein rich fractions were pooled and concentrated to a concentration of 1-2 mg/ml (Amicon Ultra-4, 10 kDa cutoff, 4000 x g). Concentrations

were determined using a Nanodrop ND-1000 photometer and extinction coefficients ( $\epsilon_{280}$ ) that were calculated using the “ProtParam” tool ([expasy.org/resources/protparam](http://expasy.org/resources/protparam)) as described in Endapally et al. 2019 [201]. Concentrated protein was either stored at 4°C for direct use or supplemented with 20% (v/v) glycerol for long term storage at -80°C.

### 5.16.3 Fluorescence labelling of ALOD4

Fluorescence labelling of purified ALOD4 was done by mixing 20 nanomoles or ALOD4 (320  $\mu$ g) with a 9-fold molar excess of Alexa Fluor 546 C5 maleimide (ThermoFisher, 8.8 mM stock in DMSO) in a total volume of 300  $\mu$ l. The reaction of the maleimide with the cysteine residue that was introduced for this purpose (S404C) was allowed to occur over night at 4°C. The reaction was then quenched by the addition of 10 mM DTT (1M stock in water) and unreacted dye removed. This was achieved by adding the quenched reaction mix to a desalting column (ZebaSpin, 2ml, 7 kDa cutoff). After centrifugation for 2 min at 1000 x g, unreacted dye mostly remained in the column, while labelled protein was eluted. The desalting step was repeated using the same column, which was first regenerated by eluting the remaining dye with AP-Buffer B until full removal from the column was confirmed by measurement of the absorbance at 546 nm in the flowthrough. The labelling efficiency was determined by measuring the absorbance at 280 nm and 546 nm and calculating the concentrations of the protein and the dye using the corresponding extinction coefficients. Labelled protein (90-100% efficiency) was stored at 4°C for further use.

### 5.16.4 ALOD4 binding assay

HeLa cells were seeded in a 48-well plate, grown for 24 hours, washed with 500  $\mu$ l PBS and incubated for 1 hour in 100  $\mu$ l fresh medium with fluorescently labelled ALOD4 or ALOD4-Mut (0, 1 or 5  $\mu$ M). Unbound ALOD4 was then washed off with 500  $\mu$ l PBS and lysed in 200  $\mu$ l SDS-lysis buffer to eliminate fluorescence quenching that reportedly occurs after binding to cholesterol-containing membranes [207]. Cells were incubated at room temperature for 20 minutes on a rocking plate, the lysates then transferred to a 96-well plate which was placed in a freezer for 2 hours to remove any bubbles. Fluorescent ALOD4 was diluted in SDS-lysis buffer to concentrations between 0 ng/ml and 500 ng/ml and added to the thawed 96-well plate as a standard curve. Fluorescence was measured at a plate reader (Molecular Devices, Spectramax M5) at

excitation/emission wavelengths of 554/570 nm and the concentrations of bound protein calculated from the standard curve and the labelling efficiency.

### 5.17 GRAMD1B relocalization analysis

#### 5.17.1 Image acquisition

HeLa 11ht wt and NPC1-KO cells stably transfected with GFP-GRAMD1B were seeded into 12-well ibidi slides and grown in lipoprotein deficient medium (charcoal stripped FBS) for 1 days before expression was induced with 25 ng/ml doxycycline. Medium was removed after 24 hours and replaced with HEPES buffered imaging medium containing 25 µg/ml Dil-LDL. After incubation for 10 minutes at 37°C, the medium was removed and the cells washed 3 times with imaging medium. Videos were captured for 30-60 minutes at room temperature at a ZEISS LSM800 microscope equipped with an Airyscan detector array. Fluorophores were excited in separate tracks (switch after each frame) with lasers at 488 nm and 561 nm, both at 1% intensity. Detection wavelengths of the two channels were 490-545 nm (GFP) and 450-700 nm (Dil) with detector gains set to 800 V and 900 V, respectively. Image resolution was 512x512 px at a scanning zoom of 4.0x, resulting in an image size of 25.35 µm. Images were scanned in serpentine without multi-scan averaging in order to minimize frame times to 0.63 s/frame. Z-resolutions and point spread functions were calculated using [svi.nl/NyquistCalculator](http://svi.nl/NyquistCalculator). Image series were deconvoluted using the Airyscan Processing method included in the ZEN software and the resulting Dil channel exported as a greyscale image series. Unprocessed images were first cropped to 488x488 px to match the dimensions of the processed images. Additional channels which contain the raw signals of all 32 Airy detectors as separate phases were not included in the export. For this purpose only phase 1 of the GFP#-channel was exported as greyscale image series. All images were also cropped to minimize the extracellular area and if cells migrated during the observed timeframe only time periods where the cell filled most of this area were further analyzed.

### 5.17.2 Data analysis

Image series were analysed using an ImageJ script developed for this purpose (see appendix). First the processed Dil-LDL image series is loaded and searched for local maxima in each frame and the amount of maxima per frame saved in a list. Then starting again at frame 1 circular regions with a previously defined radius are drawn at the coordinates of the maxima and saved in the region of interest (ROI) manager. The image is advanced to the next frame according to the number of maxima per frame that have been saved in the list. This is repeated for all other predefined radii resulting in a single list of ROIs for all frames and all circle sizes. Next, the unprocessed GFP channel image series was loaded and the previously saved ROIs selected and measured automatically. The exported result file then contained the quantified GFP signal around all LDL particles that were detected in all image frames and was measured in multiple circles with different radii for each detected maximum. The whole process was then repeated with an additional randomization step when the circular regions were drawn. For this the x- and y-coordinates of the detected maxima were shifted by a random value between -100 and +100 px (= 5  $\mu\text{m}$ ). This resulted in a second set of results with exactly the same amount of measurements for each frame.

Analysis of the data was done in MS Excel, where first all measurements were excluded where the random shift of the ROI had moved to a location outside of the frame. This was done by filtering for values where the area of the measurement with the largest radius (= background) was less than half of its intended value. Next, measurements outside the cells were excluded by removing data points where the background measurement was much lower than the average. Mean GFP signal in ring shaped regions of interest was calculated from the measurements ( $\Delta\text{integrated\_density}/\Delta\text{area}$ ) of the two circular ROIs. Enrichment of GFP in the center circle and the surrounding ring with 25 px diameter was calculated by the division of their main values by each corresponding GFP background value. Artifacts with unnaturally high or low enrichment values (1<sup>st</sup> and 99<sup>th</sup> percentile) were then excluded and the remaining datasets statistically compared using a two-tailed Student's t-test for samples with homoscedastic distribution.

## List of Abbreviations

aa	amino acids
ABCA1	ATP-binding cassette sub-family A member 1
ABCG1	ATP-binding cassette sub-family G member 1
ACAT1	Acyl-coenzyme A:cholesterol acyltransferase 1
ACBD5	Acyl-CoA-binding domain-containing protein 5
ALOD4	Anthrolysin O domain 4
AMP	Adenosine monophosphate
APEX	Ascorbate peroxidase
AU	Airy Unit
BirA*	Bifunctional ligase/repressor
BODIPY	Boron-dipyrromethene
BSA	Bovine serum albumine
CC	Creative Commons
CDC	Cholesterol dependent cytolysins
CRISPR/Cas9	Clustered Regularly Interspaced Short Palindromic Repeats
DDRKG1	DDRKG domain-containing protein 1
DMEM	Dulbecco's Modified Eagle Medium
DNA	Deoxyribonucleic acid
EGF	Epidermal growth factor
EGFR	Epidermal growth factor receptor
EM	Electron microscopy
ER	Endoplasmic reticulum
ERM	Endoplasmic reticulum membrane
FAK	Focal adhesion kinase
FDR	False discovery rate
FFAT	Two phenylalanines in an acidic track
FKBP	FK506-binding protein
FLAG	Affinity tag peptide (DYKDDDDK)
FRB	FKBP-rapamycin binding domain of mTOR
FRT	Flipase recognition target site
GAPDH	Glyceraldehyd-3-phosphat-Dehydrogenase
GFP	Green fluorescent protein
GRAM	Glucosyltransferases, Rab-like GTPase activators and Myotubularins
GRAMD1A-C	GRAM-domain containing protein
GRASP65	Golgi reassembly-stacking protein of 65 kDa
HDL	High-density lipoprotein
HMG	3-Hydroxy-3-Methylglutaryl
HMGCR	HMG-CoA reductase
IFM	Immunofluorescence microscopy

ILV	Intraluminal vesicle
INSIG	Insulin-induced gene 1 protein
KO	Knock-out
Lam6	Lipid transfer proteins anchored at membrane contact sites protein 6
LAMP1/2	Lysosome-associated membrane glycoprotein 1/2
LB	lysogeny broth
LC-MS/MS	Liquid chromatography coupled tandem mass spectroscopy
LD	Lipid droplet
LDL	Low-density lipoprotein
LDLR	LDL-receptor
LE	Late endosome
LFQ	Label-free quantification
LIMP-2	Lysosomal integral membrane protein 2
LPC	Lysosome targeted caged pacCholesterol
Ltc1	Lipid transfer at contact site protein 1
LTP	Lipid transport protein
LXR	Liver X receptor
Lys	Lysosome
Lyso-pacChol	Lysosome targeted caged pacCholesterol
MAM	Mitochondria associated membrane
MAVS	Mitochondrial antiviral signaling protein
MCS	Membrane contact site
MENTAL	MLN64 N-terminal domain
MLN64	Metastatic lymph node 64
MOSPD2	Motile sperm domain-containing protein 2
MSP-domain	Motile sperm domain
NPC1/2	Niemann-Pick type C protein 1/2
OMM	Outer mitochondrial membrane
ORAI	Calcium release-activated calcium channel protein 1
ORD	OSBP-related ligand-binding domain
ORP1L/2/5	OSBP-related protein 1/2/5
OSBP	Oxysterol-binding protein
pacChol	Photoactivatable and clickable Cholesterol
PBS	Phosphate buffered saline
PCR	Polymerase chain reaction
PDZD8	PDZ domain-containing protein 8
PEI	Polyethylenimine
PFA	Paraformaldehyde
PFO*	Perfringolysin O mutant Y181A and C459A
PH-domain	Pleckstrin homology domain

PI(4)P	Phosphatidylinositol-4-phosphate
PI(4,5)P2	Phosphatidylinositol-4,5-bisphosphate
PM	Plasma membrane
PTP1B	Tyrosine-protein phosphatase 1
RMD3	Protein tyrosine phosphatase interacting protein 51
Rab7/8	Ras-related protein Rab-7a
RILP	Rab-interacting lysosomal protein
RIPA	Radioimmunoprecipitation Assay Puffer
RMD3	Regulator of microtubule dynamics protein 3
ROI	Region of interes
SCAP	SREBP cleavage activating protein
SD	Standard deviation
SDS-PAGE	Sodium dodecylsulfate polyacrylamide gel electrophoresis
SSD	Sterol sensing domain
SE	Standard error
SEC	Size exclusion chromatography
SNX13	Sorting nexin-13
SREBP	Sterol regulatory element binding protein
START	StAR-related lipid transfer
STARD3/4	START-domain containing protein 3/4
STIM	Stromal interaction molecule 1
TBS	Tris buffered saline
TGN38	Trans-Golgi network integral membrane protein
TLC	Thin layer chromatogrpahy
UFM1	Ubiquitin-fold modifier 1
UFL1	E3 UFM1-protein ligase 1
UPR	Unfolded protein response
UV	Ultraviolet
VAMP	Vesicle-associated membrane protein
VAP-A/B	VAMP-associated protein A/B
WT	Wild type



## Bibliography

- [1] W.A. Prinz, A. Toulmay, T. Balla, The functional universe of membrane contact sites, *Nat. Rev. Mol. Cell Biol.* 21 (2020) 7–24. <https://doi.org/10.1038/s41580-019-0180-9>.
- [2] J.C.M. Holthuis, C. Ungermann, Cellular microcompartments constitute general suborganellar functional units in cells, *Biol. Chem.* 394 (2013) 151–161. <https://doi.org/10.1515/hsz-2012-0265>.
- [3] M.G. Farquhar, G.E. Palade, The Golgi apparatus (complex) (1954-1981) from artifact to center stage, *J. Cell Biol.* 91 (1981). <https://doi.org/10.1083/jcb.91.3.77s>.
- [4] R. Fernández-Busnadiego, Y. Saheki, P. De Camilli, Three-dimensional architecture of extended synaptotagmin-mediated endoplasmic reticulum-plasma membrane contact sites, *Proc. Natl. Acad. Sci. U. S. A.* 112 (2015) E2004–E2013. <https://doi.org/10.1073/pnas.1503191112>.
- [5] M. West, N. Zurek, A. Hoenger, G.K. Voeltz, A 3D analysis of yeast ER structure reveals how ER domains are organized by membrane curvature, *J. Cell Biol.* 193 (2011) 333–346. <https://doi.org/10.1083/jcb.201011039>.
- [6] F. Alpy, A. Rousseau, Y. Schwab, F. Legueux, I. Stoll, C. Wendling, C. Spiegelhalter, P. Kessler, C. Mathelin, M.C. Rio, T.P. Levine, C. Tomasetto, STARD3 or STARD3NL and VAP form a novel molecular tether between late endosomes and the ER, *J. Cell Sci.* 126 (2013) 5500–5512. <https://doi.org/10.1242/jcs.139295>.
- [7] S. Schuck, W.A. Prinz, K.S. Thorn, C. Voss, P. Walter, Membrane expansion alleviates endoplasmic reticulum stress independently of the unfolded protein response, *J. Cell Biol.* 187 (2009) 525–536. <https://doi.org/10.1083/jcb.200907074>.
- [8] N. Rocha, C. Kuijl, R. Van Der Kant, L. Janssen, D. Houben, H. Janssen, W. Zwart, J. Neefjes, Cholesterol sensor ORP1L contacts the ER protein VAP to control Rab7-RILP-p150Glued and late endosome positioning, *J. Cell Biol.* 185 (2009) 1209–1225. <https://doi.org/10.1083/jcb.200811005>.
- [9] M. Johansson, N. Rocha, W. Zwart, I. Jordens, L. Janssen, C. Kuijl, V.M. Olkkonen, J. Neefjes, Activation of endosomal dynein motors by stepwise assembly of Rab7-RILP-p150Glued, ORP1L, and the receptor  $\beta$ III spectrin, *J. Cell Biol.* 176 (2007) 459–471. <https://doi.org/10.1083/jcb.200606077>.
- [10] T.T. Nguyen, A. Lewandowska, J.Y. Choi, D.F. Markgraf, M. Junker, M. Bilgin, C.S. Ejsing, D.R. Voelker, T.A. Rapoport, J.M. Shaw, Gem1 and ERMES Do Not Directly Affect Phosphatidylserine Transport from ER to Mitochondria or Mitochondrial Inheritance, *Traffic.* 13 (2012) 880–890. <https://doi.org/10.1111/j.1600-0854.2012.01352.x>.
- [11] J.R. Friedman, L.L. Lackner, M. West, J.R. DiBenedetto, J. Nunnari, G.K. Voeltz, ER tubules mark sites of mitochondrial division, *Science* (80-. ). 334 (2011) 358–362. <https://doi.org/10.1126/science.1207385>.
- [12] S.C.J. Helle, G. Kanfer, K. Kolar, A. Lang, A.H. Michel, B. Kornmann, Organization and function of membrane contact sites, *Biochim. Biophys. Acta - Mol. Cell Res.* 1833 (2013) 2526–2541. <https://doi.org/10.1016/j.bbamcr.2013.01.028>.
- [13] W. Bernhard, C. Rouiller, Close topographical relationship between mitochondria and ergastoplasm of liver cells in a definite phase of cellular activity, *J. Biophys. Biochem. Cytol.* 2 (1956) 73–78. <https://doi.org/10.1083/jcb.2.4.73>.
- [14] D.E. Copeland, A.J. Dalton, An Association between Mitochondria and the Endoplasmic Reticulum in Cells of the Pseudobranch Gland of a Teleost, *J. Biophys. Biochem. Cytol.* 5 (1959) 393–396. <https://doi.org/10.1083/jcb.5.3.393>.

- [15] A.M. Valm, S. Cohen, W.R. Legant, J. Melunis, U. Hershberg, E. Wait, A.R. Cohen, M.W. Davidson, E. Betzig, J. Lippincott-Schwartz, Applying systems-level spectral imaging and analysis to reveal the organelle interactome, *Nature*. 546 (2017) 162–167. <https://doi.org/10.1038/nature22369>.
- [16] N. Shai, E. Yifrach, C.W.T. Van Roermund, N. Cohen, C. Bibi, L. Ijlst, L. Cavellini, J. Meurisse, R. Schuster, L. Zada, M.C. Mari, F.M. Reggiori, A.L. Hughes, M. Escobar-Henriques, M.M. Cohen, H.R. Waterham, R.J.A. Wanders, M. Schuldiner, E. Zalckvar, Systematic mapping of contact sites reveals tethers and a function for the peroxisome-mitochondria contact, *Nat. Commun.* 9 (2018) 1761. <https://doi.org/10.1038/s41467-018-03957-8>.
- [17] J. Jing, G. Liu, Y. Huang, Y. Zhou, A molecular toolbox for interrogation of membrane contact sites, *J. Physiol.* 598 (2020) 1725–1739. <https://doi.org/10.1113/JP277761>.
- [18] M. Eisenberg-Bord, N. Shai, M. Schuldiner, M. Bohnert, A Tether Is a Tether Is a Tether: Tethering at Membrane Contact Sites, 2016. <https://doi.org/10.1016/j.devcel.2016.10.022>.
- [19] C.J.R. Loewen, A. Roy, T.P. Levine, A conserved ER targeting motif in three families of lipid binding proteins and in Opi1p binds VAP, *EMBO J.* 22 (2003) 2025–2035. <https://doi.org/10.1093/emboj/cdg201>.
- [20] V. Mikitova, T.P. Levine, Analysis of the key elements of FFAT-like motifs identifies new proteins that potentially bind VAP on the ER, including two AKAPs and FAPP2, *PLoS One*. 7 (2012) e30455. <https://doi.org/10.1371/journal.pone.0030455>.
- [21] S.E. Kaiser, J.H. Brickner, A.R. Reilein, T.D. Fenn, P. Walter, A.T. Brunger, Structural basis of FFAT motif-mediated ER targeting, *Structure*. 13 (2005) 1035–1045. <https://doi.org/10.1016/j.str.2005.04.010>.
- [22] B. Mesmin, J. Bigay, J. Moser Von Filseck, S. Lacas-Gervais, G. Drin, B. Antonny, A four-step cycle driven by PI(4)P hydrolysis directs sterol/PI(4)P exchange by the ER-Golgi Tether OSBP, *Cell*. 155 (2013) 830. <https://doi.org/10.1016/j.cell.2013.09.056>.
- [23] J. Liou, M. Fivaz, T. Inoue, T. Meyer, Live-cell imaging reveals sequential oligomerization and local plasma membrane targeting of stromal interaction molecule 1 after Ca<sup>2+</sup> store depletion, *Proc. Natl. Acad. Sci. U. S. A.* 104 (2007) 9301–9306. <https://doi.org/10.1073/pnas.0702866104>.
- [24] R. Van Der Kant, I. Zondervan, L. Janssen, J. Neefjes, Cholesterol-binding molecules MLN64 and ORP1L mark distinct late endosomes with transporters ABCA3 and NPC1, *J. Lipid Res.* 54 (2013) 2153–2165. <https://doi.org/10.1194/jlr.M037325>.
- [25] E. Quon, Y.Y. Sere, N. Chauhan, J. Johansen, D.P. Sullivan, J.S. Dittman, W.J. Rice, R.B. Chan, G. Di Paolo, C.T. Beh, A.K. Menon, Endoplasmic reticulum-plasma membrane contact sites integrate sterol and phospholipid regulation, *PLoS Biol.* 16 (2018) e2003864. <https://doi.org/10.1371/journal.pbio.2003864>.
- [26] M.J. Hoyer, P.J. Chitwood, C.C. Ebmeier, J.F. Striepen, R.Z. Qi, W.M. Old, G.K. Voeltz, A Novel Class of ER Membrane Proteins Regulates ER-Associated Endosome Fission, *Cell*. 175 (2018) 254–265.e14. <https://doi.org/10.1016/j.cell.2018.08.030>.
- [27] M. Besprozvannaya, E. Dickson, H. Li, K.S. Ginburg, D.M. Bers, J. Auwerx, J. Nunnari, GRAM domain proteins specialize functionally distinct ER-PM contact sites in human cells, *Elife*. 7 (2018) 1–25. <https://doi.org/10.7554/eLife.31019>.
- [28] A. Murley, R.D. Sarsam, A. Toulmay, J. Yamada, W.A. Prinz, J. Nunnari, Ltc1 is an ER-localized sterol transporter and a component of ER-mitochondria and ER-vacuole contacts, *J. Cell Biol.* 209 (2015) 539–548. <https://doi.org/10.1083/jcb.201502033>.

- [29] A.T. Gatta, L.H. Wong, Y.Y. Sere, D.M. Calderón-Noreña, S. Cockcroft, A.K. Menon, T.P. Levine, A new family of StART domain proteins at membrane contact sites has a role in ER-PM sterol transport, *Elife*. 4 (2015) 1–46. <https://doi.org/10.7554/eLife.07253>.
- [30] Höglinger, T. Burgoyne, E. Sanchez-Heras, P. Hartwig, A. Colaco, J. Newton, C.E. Futter, S. Spiegel, F.M. Platt, E.R. Eden, NPC1 regulates ER contacts with endocytic organelles to mediate cholesterol egress, *Nat. Commun.* 10 (2019) 4276. <https://doi.org/10.1038/s41467-019-12152-2>.
- [31] L.K. Liu, V. Choudhary, A. Toulmay, W.A. Prinz, An inducible ER-Golgi tether facilitates ceramide transport to alleviate lipotoxicity, *J. Cell Biol.* 216 (2017) 131–147. <https://doi.org/10.1083/jcb.201606059>.
- [32] L. Scorrano, M.A. De Matteis, S. Emr, F. Giordano, G. Hajnóczky, B. Kornmann, L.L. Lackner, T.P. Levine, L. Pellegrini, K. Reinisch, R. Rizzuto, T. Simmen, H. Stenmark, C. Ungermann, M. Schuldiner, Coming together to define membrane contact sites, *Nat. Commun.* 10 (2019) 1–11. <https://doi.org/10.1038/s41467-019-09253-3>.
- [33] G. Csordás, P. Várnai, T. Golenár, S. Roy, G. Purkins, T.G. Schneider, T. Balla, G. Hajnóczky, Imaging Interorganelle Contacts and Local Calcium Dynamics at the ER-Mitochondrial Interface, *Mol. Cell.* 39 (2010) 121–132. <https://doi.org/10.1016/j.molcel.2010.06.029>.
- [34] R. Galmes, A. Houcine, A.R. Vliet, P. Agostinis, C.L. Jackson, F. Giordano, ORP5/ORP8 localize to endoplasmic reticulum–mitochondria contacts and are involved in mitochondrial function, *EMBO Rep.* 17 (2016) 800–810. <https://doi.org/10.15252/embr.201541108>.
- [35] G. Csordás, C. Renken, P. Várnai, L. Walter, D. Weaver, K.F. Buttle, T. Balla, C.A. Mannella, G. Hajnóczky, Structural and functional features and significance of the physical linkage between ER and mitochondria, *J. Cell Biol.* 174 (2006) 915–921. <https://doi.org/10.1083/jcb.200604016>.
- [36] F. Giordano, Y. Saheki, O. Idevall-Hagren, S.F. Colombo, M. Pirruccello, I. Milosevic, E.O. Gracheva, S.N. Bagriantsev, N. Borgese, P. De Camilli, PI(4,5)P<sub>2</sub>-Dependent and Ca<sup>2+</sup>-Regulated ER-PM Interactions Mediated by the Extended Synaptotagmins, *Cell.* 153 (2013) 1494–1509. <https://doi.org/10.1016/j.cell.2013.05.026>.
- [37] M. Fujimoto, T. Hayashi, T.P. Su, The role of cholesterol in the association of endoplasmic reticulum membranes with mitochondria, *Biochem. Biophys. Res. Commun.* 417 (2012) 635–639. <https://doi.org/10.1016/j.bbrc.2011.12.022>.
- [38] A.E. Rusiñol, Z. Cui, M.H. Chen, J.E. Vance, A unique mitochondria-associated membrane fraction from rat liver has a high capacity for lipid synthesis and contains pre-Golgi secretory proteins including nascent lipoproteins, *J. Biol. Chem.* 269 (1994) 27494–27502.
- [39] X. Wang, Y. Wen, J. Dong, C. Cao, S. Yuan, Systematic In-Depth Proteomic Analysis of Mitochondria-Associated Endoplasmic Reticulum Membranes in Mouse and Human Testes, *Proteomics.* 18 (2018) 1700478. <https://doi.org/10.1002/pmic.201700478>.
- [40] C.N. Poston, Mass Spectrometry-Based Global Proteomic Analysis of Endoplasmic Reticulum and Mitochondria Contact Sites, Dissertation. (2013). <https://repository.library.brown.edu/storage/bdr:320610/PDF/>.
- [41] V. Hung, S.S. Lam, N.D. Udeshi, T. Svinkina, G. Guzman, V.K. Mootha, S.A. Carr, A.Y. Ting, Proteomic mapping of cytosol-facing outer mitochondrial and ER membranes in living human cells by proximity biotinylation, *Elife*. 6 (2017) 1–38. <https://doi.org/10.7554/eLife.24463>.

- [42] I.-T. Cho, G. Adelmant, Y. Lim, J.A. Marto, G. Cho, J.A. Golden, Ascorbate peroxidase proximity labeling coupled with biochemical fractionation identifies promoters of endoplasmic reticulum–mitochondrial contacts, *J. Biol. Chem.* 292 (2017) 16382–16392. <https://doi.org/10.1074/jbc.M117.795286>.
- [43] K.J. Roux, D.I. Kim, M. Raida, B. Burke, A promiscuous biotin ligase fusion protein identifies proximal and interacting proteins in mammalian cells, *J. Cell Biol.* 196 (2012) 801–810. <https://doi.org/10.1083/jcb.201112098>.
- [44] B.E. Burke, K.J. Roux, D.I. Kim, B. Burke, BioID : A Screen for Protein-Protein Interactions BioID : A Screen for Protein-Protein Interactions, (2015) 1–20. <https://doi.org/10.1002/cpps.51.BioID>.
- [45] R. Varnaité, S.A. MacNeill, Meet the neighbors: Mapping local protein interactomes by proximity-dependent labeling with BioID, *Proteomics.* 16 (2016) 2503–2518. <https://doi.org/10.1002/pmic.201600123>.
- [46] P. Li, J. Li, L. Wang, L.J. Di, Proximity Labeling of Interacting Proteins: Application of BioID as a Discovery Tool, *Proteomics.* 17 (2017) 1700002. <https://doi.org/10.1002/pmic.201700002>.
- [47] C.D. Go, J.D.R. Knight, A. Rajasekharan, B. Rathod, G.G. Hesketh, K.T. Abe, J.Y. Youn, P. Samavarchi-Tehrani, H. Zhang, L.Y. Zhu, E. Popiel, J.P. Lambert, É. Coyaud, S.W.T. Cheung, D. Rajendran, C.J. Wong, H. Antonicka, L. Pelletier, A.F. Palazzo, E.A. Shoubridge, B. Raught, A.C. Gingras, A proximity-dependent biotinylation map of a human cell, *Nature.* 595 (2021) 120–124. <https://doi.org/10.1038/s41586-021-03592-2>.
- [48] B. Cabukusta, I. Berlin, D.M. van Elsland, I. Forkink, M. Spits, A.W.M. de Jong, J.J.L.L. Akkermans, R.H.M. Wijdeven, G.M.C. Janssen, P.A. van Veelen, J. Neefjes, Human VAPome Analysis Reveals MOSPD1 and MOSPD3 as Membrane Contact Site Proteins Interacting with FFAT-Related FFNT Motifs, *Cell Rep.* 33 (2020) 108475. <https://doi.org/10.1016/j.celrep.2020.108475>.
- [49] D.I. Kim, S.C. Jensen, K.A. Noble, B. Kc, K.H. Roux, K. Motamedchaboki, K.J. Roux, An improved smaller biotin ligase for BioID proximity labeling, *Mol. Biol. Cell.* 27 (2016) 1188–1196. <https://doi.org/10.1091/mbc.E15-12-0844>.
- [50] T.C. Branon, J.A. Bosch, A.D. Sanchez, N.D. Udeshi, T. Svinkina, S.A. Carr, J.L. Feldman, N. Perrimon, A.Y. Ting, Directed evolution of TurboID for efficient proximity labeling in living cells and organisms, *BioRxiv.* (2017) 196980. <https://doi.org/10.1101/196980>.
- [51] I.M. Schopp, C.C. Amaya Ramirez, J. Debeljak, E. Kreibich, M. Skribbe, K. Wild, J. Béthune, Split-BioID a conditional proteomics approach to monitor the composition of spatiotemporally defined protein complexes, *Nat. Commun.* 8 (2017) 15690. <https://doi.org/10.1038/ncomms15690>.
- [52] C. Kwak, S. Shin, J.-S. Park, M. Jung, T.T.M. Nhung, M.-G. Kang, C. Lee, T.-H. Kwon, S.K. Park, J.Y. Mun, J.-S. Kim, H.-W. Rhee, Contact-ID, a tool for profiling organelle contact sites, reveals regulatory proteins of mitochondrial-associated membrane formation, *Proc. Natl. Acad. Sci.* 117 (2020) 12109–12120. <https://doi.org/10.1073/pnas.1916584117>.
- [53] K.F. Cho, T.C. Branon, S. Rajeev, T. Svinkina, N.D. Udeshi, T. Thoudam, C. Kwak, H.-W. Rhee, I.-K. Lee, S.A. Carr, A.Y. Ting, Split-TurboID enables contact-dependent proximity labeling in cells, *Proc. Natl. Acad. Sci.* 117 (2020) 12143–12154. <https://doi.org/10.1073/pnas.1919528117>.

- [54] S. De Munter, J. Görnemann, R. Derua, B. Lesage, J. Qian, E. Heroes, E. Waelkens, A. Van Eynde, M. Beullens, M. Bollen, Split-BioID: a proximity biotinylation assay for dimerization-dependent protein interactions, *FEBS Lett.* 591 (2017) 415–424. <https://doi.org/10.1002/1873-3468.12548>.
- [55] A. Martello, F.M. Platt, E.R. Eden, Staying in touch with the endocytic network: The importance of contacts for cholesterol transport, *Traffic.* 21 (2020) 354–363. <https://doi.org/10.1111/tra.12726>.
- [56] E.R. Eden, I.J. White, A. Tsapara, C.E. Futter, Membrane contacts between endosomes and ER provide sites for PTP1B-epidermal growth factor receptor interaction, *Nat. Cell Biol.* 12 (2010) 267–272. <https://doi.org/10.1038/ncb2026>.
- [57] S. Feske, Calcium signalling in lymphocyte activation and disease, *Nat. Rev. Immunol.* 7 (2007) 690–702. <https://doi.org/10.1038/nri2152>.
- [58] D.A. Baum, B. Baum, An inside-out origin for the eukaryotic cell, *BMC Biol.* 12 (2014) 1–22. <https://doi.org/10.1186/s12915-014-0076-2>.
- [59] M.J. Berridge, M.D. Bootman, H.L. Roderick, Calcium signalling: Dynamics, homeostasis and remodelling, *Nat. Rev. Mol. Cell Biol.* 4 (2003) 517–529. <https://doi.org/10.1038/nrm1155>.
- [60] J.D. Jones, T.E. Thompson, Spontaneous Phosphatidylcholine Transfer by Collision between Vesicles at High Lipid Concentration, *Biochemistry.* 28 (1989) 129–134. <https://doi.org/10.1021/bi00427a019>.
- [61] J.R. Rogers, G. Espinoza Garcia, P.L. Geissler, Membrane hydrophobicity determines the activation free energy of passive lipid transport, *Biophys. J.* 120 (2021) 3718–3731. <https://doi.org/10.1016/j.bpj.2021.07.016>.
- [62] K. Simons, J.L. Sampaio, Membrane Organization and Lipid Rafts, *Cold Spring Harb. Perspect. Biol.* 3 (2011) a004697–a004697. <https://doi.org/10.1101/cshperspect.a004697>.
- [63] P. Cicutta, S.L. Keller, S.L. Veatch, Diffusion of liquid domains in lipid bilayer membranes, *J. Phys. Chem. B.* 111 (2007) 3328–3331. <https://doi.org/10.1021/jp0702088>.
- [64] G. van Meer, D.R. Voelker, G.W. Feigenson, Membrane lipids: where they are and how they behave, *Nat. Rev. Mol. Cell Biol.* 9 (2008) 112–124. <https://doi.org/10.1038/nrm2330>.
- [65] S. Lev, Non-vesicular lipid transport by lipid-transfer proteins and beyond, *Nat. Rev. Mol. Cell Biol.* 11 (2010) 739–750. <https://doi.org/10.1038/nrm2971>.
- [66] J.E. Vance, E.J. Aasman, R. Szarka, Brefeldin A does not inhibit the movement of phosphatidylethanolamine from its sites of synthesis to the cell surface, *J. Biol. Chem.* 266 (1991) 8241–8247. [https://doi.org/10.1016/s0021-9258\(18\)92968-6](https://doi.org/10.1016/s0021-9258(18)92968-6).
- [67] T. Levine, Short-range intracellular trafficking of small molecules across endoplasmic reticulum junctions, *Trends Cell Biol.* 14 (2004) 483–490. <https://doi.org/10.1016/j.tcb.2004.07.017>.
- [68] S. Lahiri, A. Toulmay, W.A. Prinz, Membrane contact sites, gateways for lipid homeostasis, *Curr. Opin. Cell Biol.* 33 (2015) 82–87. <https://doi.org/10.1016/j.ceb.2014.12.004>.
- [69] K.W. Wirtz, D.B. Zilversmit, Exchange of phospholipids between liver mitochondria and microsomes in vitro., *J. Biol. Chem.* 243 (1968) 3596–3602. [https://doi.org/10.1016/s0021-9258\(19\)34182-1](https://doi.org/10.1016/s0021-9258(19)34182-1).
- [70] L.H. Wong, T.P. Levine, Lipid transfer proteins do their thing anchored at membrane contact sites . . . but what is their thing?, *Biochem. Soc. Trans.* 44 (2016) 517–527. <https://doi.org/10.1042/BST20150275>.

- [71] J.S. Dittman, A.K. Menon, Speed Limits for Nonvesicular Intracellular Sterol Transport, *Trends Biochem. Sci.* 42 (2017) 90–97. <https://doi.org/10.1016/j.tibs.2016.11.004>.
- [72] L.H. Wong, A.T. Gatta, T.P. Levine, Lipid transfer proteins: the lipid commute via shuttles, bridges and tubes, *Nat. Rev. Mol. Cell Biol.* 20 (2019) 85–101. <https://doi.org/10.1038/s41580-018-0071-5>.
- [73] M. de Saint-Jean, V. Delfosse, D. Douguet, G. Chicanne, B. Payraastre, W. Bourguet, B. Antonny, G. Drin, Osh4p exchanges sterols for phosphatidylinositol 4-phosphate between lipid bilayers, *J. Cell Biol.* 195 (2011) 965–978. <https://doi.org/10.1083/jcb.201104062>.
- [74] B. Mesmin, B. Antonny, The counterflow transport of sterols and PI4P, *Biochim. Biophys. Acta - Mol. Cell Biol. Lipids.* 1861 (2016) 940–951. <https://doi.org/10.1016/j.bbalip.2016.02.024>.
- [75] Y. Lange, M.H. Swaisgood, B. V. Ramos, T.L. Steck, Plasma Membranes Contain Half the Phospholipid and 90% of the Cholesterol and Sphingomyelin in Cultured Human Fibroblasts, *J. Biol. Chem.* 264 (1989) 3786–3793. [https://doi.org/10.1016/S0021-9258\(19\)84918-9](https://doi.org/10.1016/S0021-9258(19)84918-9).
- [76] A. Radhakrishnan, J.L. Goldstein, J.G. McDonald, M.S. Brown, Switch-like Control of SREBP-2 Transport Triggered by Small Changes in ER Cholesterol: A Delicate Balance, *Cell Metab.* 8 (2008) 512–521. <https://doi.org/10.1016/j.cmet.2008.10.008>.
- [77] V. Schoop, A. Martello, E.R. Eden, D. Höglinger, Cellular cholesterol and how to find it, *Biochim. Biophys. Acta - Mol. Cell Biol. Lipids.* 1866 (2021). <https://doi.org/10.1016/j.bbalip.2021.158989>.
- [78] B. Mesmin, B. Antonny, G. Drin, Insights into the mechanisms of sterol transport between organelles, *Cell. Mol. Life Sci.* 70 (2013) 3405–3421. <https://doi.org/10.1007/s00018-012-1247-3>.
- [79] M.R. Kaplan, R.D. Simoni, Transport of cholesterol from the endoplasmic reticulum to the plasma membrane, 1985. <https://doi.org/10.1083/jcb.101.2.446>.
- [80] N.A. Baumann, D.P. Sullivan, H. Ohvo-Rekilä, C. Simonot, A. Pottekat, Z. Klaassen, C.T. Beh, A.K. Menon, Transport of newly synthesized sterol to the sterol-enriched plasma membrane occurs via nonvesicular equilibration, *Biochemistry.* 44 (2005) 5816–5826. <https://doi.org/10.1021/bi048296z>.
- [81] S. Heino, S. Lusa, P. Somerharju, C. Ehnholm, V.M. Oikkonen, E. Ikonen, Dissecting the role of the Golgi complex and lipid rafts in biosynthetic transport of cholesterol to the cell surface, *Proc. Natl. Acad. Sci. U. S. A.* 97 (2000) 8375–8380. <https://doi.org/10.1073/pnas.140218797>.
- [82] E. Ikonen, Cellular cholesterol trafficking and compartmentalization, *Nat. Rev. Mol. Cell Biol.* 9 (2008) 125–138. <https://doi.org/10.1038/nrm2336>.
- [83] J.D. Horton, N.A. Shah, J.A. Warrington, N.N. Anderson, S.W. Park, M.S. Brown, J.L. Goldstein, Combined analysis of oligonucleotide microarray data from transgenic and knockout mice identifies direct SREBP target genes, *Proc. Natl. Acad. Sci. U. S. A.* 100 (2003) 12027–12032. <https://doi.org/10.1073/pnas.1534923100>.
- [84] D.J.H. van den Boomen, A. Sienkiewicz, I. Berlin, M.L.M. Jongsma, D.M. van Elsland, J.P. Luzio, J.J.C. Neefjes, P.J. Lehner, A trimeric Rab7 GEF controls NPC1-dependent lysosomal cholesterol export, *Nat. Commun.* 11 (2020) 1–18. <https://doi.org/10.1038/s41467-020-19032-0>.
- [85] T. Yang, P.J. Espenshade, M.E. Wright, D. Yabe, Y. Gong, R. Aebersold, J.L. Goldstein, M.S. Brown, Crucial step in cholesterol homeostasis: Sterols promote binding of SCAP to INSIG-1, a membrane protein that facilitates retention of SREBPs in ER, *Cell.* 110 (2002) 489–500. [https://doi.org/10.1016/S0092-8674\(02\)00872-3](https://doi.org/10.1016/S0092-8674(02)00872-3).

- [86] M.S. Brown, J.L. Goldstein, The SREBP pathway: Regulation of cholesterol metabolism by proteolysis of a membrane-bound transcription factor, *Cell*. 89 (1997) 331–340. [https://doi.org/10.1016/S0092-8674\(00\)80213-5](https://doi.org/10.1016/S0092-8674(00)80213-5).
- [87] T.Y. Chang, C.C.Y. Chang, N. Ohgami, Y. Yamauchi, Cholesterol sensing, trafficking, and esterification, *Annu. Rev. Cell Dev. Biol.* 22 (2006) 129–157. <https://doi.org/10.1146/annurev.cellbio.22.010305.104656>.
- [88] N. Sever, T. Yang, M.S. Brown, J.L. Goldstein, R.A. DeBose-Boyd, Accelerated degradation of HMG CoA reductase mediated by binding of insig-1 to its sterol-sensing domain, *Mol. Cell*. 11 (2003) 25–33. [https://doi.org/10.1016/S1097-2765\(02\)00822-5](https://doi.org/10.1016/S1097-2765(02)00822-5).
- [89] S.M. Grundy, Absorption and metabolism of dietary cholesterol., *Annu. Rev. Nutr.* 3 (1983) 71–96. <https://doi.org/10.1146/annurev.nu.03.070183.000443>.
- [90] M.B.L. Winkler, R.T. Kidmose, M. Szomek, K. Thaysen, S. Rawson, S.P. Muench, D. Wüstner, B.P. Pedersen, Structural Insight into Eukaryotic Sterol Transport through Niemann-Pick Type C Proteins, *Cell*. 179 (2019) 485–497.e18. <https://doi.org/10.1016/j.cell.2019.08.038>.
- [91] R.E. Infante, M.L. Wang, A. Radhakrishnan, J.K. Hyock, M.S. Brown, J.L. Goldstein, NPC2 facilitates bidirectional transfer of cholesterol between NPC1 and lipid bilayers, a step in cholesterol egress from lysosomes, *Proc. Natl. Acad. Sci. U. S. A.* 105 (2008) 15287–15292. <https://doi.org/10.1073/pnas.0807328105>.
- [92] S. Xu, B. Benoff, H.L. Liou, P. Lobel, A.M. Stock, Structural basis of sterol binding by NPC2, a lysosomal protein deficient in Niemann-Pick type C2 disease, *J. Biol. Chem.* 282 (2007) 23525–23531. <https://doi.org/10.1074/jbc.M703848200>.
- [93] J. Li, S.R. Pfeffer, Lysosomal membrane glycoproteins bind cholesterol and contribute to lysosomal cholesterol export, *Elife*. 5 (2016) 1–16. <https://doi.org/10.7554/eLife.21635>.
- [94] C.S. Huang, X. Yu, P. Fordstrom, K. Choi, B.C. Chung, S.H. Roh, W. Chiu, M. Zhou, X. Min, Z. Wang, Cryo-EM structures of NPC1L1 reveal mechanisms of cholesterol transport and ezetimibe inhibition, *Sci. Adv.* 6 (2020) 1–12. <https://doi.org/10.1126/sciadv.abb1989>.
- [95] R.E. Infante, L. Abi-Mosleh, A. Radhakrishnan, J.D. Dale, M.S. Brown, J.L. Goldstein, Purified NPC1 protein: I. Binding of cholesterol and oxysterols to a 1278-amino acid membrane protein, *J. Biol. Chem.* 283 (2008) 1052–1063. <https://doi.org/10.1074/jbc.M707943200>.
- [96] R.E. Infante, A. Radhakrishnan, L. Abi-Mosleh, L.N. Kinch, M.L. Wang, N. V. Grishin, J.L. Goldstein, M.S. Brown, Purified NPC1 protein II. Localization of sterol binding to a 240-amino acid soluble luminal loop, *J. Biol. Chem.* 283 (2008) 1064–1075. <https://doi.org/10.1074/jbc.M707944200>.
- [97] N. Ohgami, D.C. Kot, M. Thomas, M.P. Scott, C.C.Y. Chang, T.Y. Chang, Binding between the Niemann-Pick C1 protein and a photoactivatable cholesterol analog requires a functional sterol-sensing domain, *Proc. Natl. Acad. Sci. U. S. A.* 101 (2004) 12473–12478. <https://doi.org/10.1073/pnas.0405255101>.
- [98] K.S. Conrad, T.W. Cheng, D. Ysselstein, S. Heybrock, L.R. Hoth, B.A. Chrnyk, C.W. Am Ende, D. Krainc, M. Schwake, P. Saftig, S. Liu, X. Qiu, M.D. Ehlers, Lysosomal integral membrane protein-2 as a phospholipid receptor revealed by biophysical and cellular studies, *Nat. Commun.* 8 (2017). <https://doi.org/10.1038/s41467-017-02044-8>.
- [99] S. Heybrock, K. Kanerva, Y. Meng, C. Ing, A. Liang, Z.J. Xiong, X. Weng, Y. Ah Kim, R. Collins, W. Trimble, R. Pomès, G.G. Privé, W. Annaert, M. Schwake, J. Heeren, R. Lüllmann-Rauch, S. Grinstein, E. Ikonen, P. Saftig, D. Neculai, Lysosomal integral membrane protein-2 (LIMP-2/SCARB2) is involved in lysosomal cholesterol export, *Nat. Commun.* 10 (2019) 1–12. <https://doi.org/10.1038/s41467-019-11425-0>.

- [100] Y. Meng, S. Heybrock, D. Neculai, P. Saftig, Cholesterol Handling in Lysosomes and Beyond, *Trends Cell Biol.* 30 (2020) 452–466. <https://doi.org/10.1016/j.tcb.2020.02.007>.
- [101] W. Möbius, Y. Ohno-Iwashita, E.G. Van Donselaar, V.M.J. Oorschot, Y. Shimada, T. Fujimoto, H.F.G. Heijnen, H.J. Geuze, J.W. Slot, Immunoelectron microscopic localization of cholesterol using biotinylated and non-cytolytic perfringolysin O, *J. Histochem. Cytochem.* 50 (2002) 43–55. <https://doi.org/10.1177/002215540205000105>.
- [102] E.B. Neufeld, A.M. Cooney, J. Pitha, E.A. Dawidowicz, N.K. Dwyer, P.G. Pentchev, E. Joan Blanchette-Mackie, Intracellular trafficking of cholesterol monitored with a cyclodextrin, *J. Biol. Chem.* 271 (1996) 21604–21613. <https://doi.org/10.1074/jbc.271.35.21604>.
- [103] K.W. Underwood, N.L. Jacobs, A. Howley, L. Liscum, Evidence for a cholesterol transport pathway from lysosomes to endoplasmic reticulum that is independent of the plasma membrane, *J. Biol. Chem.* 273 (1998) 4266–4274. <https://doi.org/10.1074/jbc.273.7.4266>.
- [104] X. Du, J. Kumar, C. Ferguson, T.A. Schulz, Y.S. Ong, W. Hong, W.A. Prinz, R.G. Parton, A.J. Brown, H. Yang, A role for oxysterol-binding protein-related protein 5 in endosomal cholesterol trafficking, *J. Cell Biol.* 192 (2011) 121–135. <https://doi.org/10.1083/jcb.201004142>.
- [105] K. Zhao, N.D. Ridgway, Oxysterol-Binding Protein-Related Protein 1L Regulates Cholesterol Egress from the Endo-Lysosomal System, *Cell Rep.* 19 (2017) 1807–1818. <https://doi.org/10.1016/j.celrep.2017.05.028>.
- [106] Y.J. Im, S. Raychaudhuri, W.A. Prinz, J.H. Hurley, Structural mechanism for sterol sensing and transport by OSBP-related proteins, *Science* (80-. ). 437 (2006) 154–158.
- [107] M. Suchanek, R. Hynynen, G. Wohlfahrt, M. Lehto, M. Johansson, H. Saarinen, A. Radzikowska, C. Thiele, V.M. Olkkonen, The mammalian oxysterol-binding protein-related proteins (ORPs) bind 25-hydroxycholesterol in an evolutionary conserved pocket, *Biochem. J.* 405 (2007) 473–480. <https://doi.org/10.1042/BJ20070176>.
- [108] G. Drin, J. Moser Von Filseck, A. Čopič, New molecular mechanisms of inter-organelle lipid transport, *Biochem. Soc. Trans.* 44 (2016) 486–492. <https://doi.org/10.1042/BST20150265>.
- [109] M. Charman, B.E. Kennedy, N. Osborne, B. Karten, MLN64 mediates egress of cholesterol from endosomes to mitochondria in the absence of functional Niemann-Pick Type C1 protein, *J. Lipid Res.* 51 (2010) 1023–1034. <https://doi.org/10.1194/jlr.M002345>.
- [110] E. Balboa, J. Castro, M.J. Pinochet, G.I. Cancino, N. Matías, P. José Sáez, A. Martínez, A.R. Álvarez, C. Garcia-Ruiz, J.C. Fernandez-Checa, S. Zanlungo, MLN64 induces mitochondrial dysfunction associated with increased mitochondrial cholesterol content, *Redox Biol.* 12 (2017) 274–284. <https://doi.org/10.1016/j.redox.2017.02.024>.
- [111] M. Hölttä-Vuori, F. Alpy, K. Tanhuanpää, E. Jokitalo, A.L. Mutka, E. Ikonen, MLN64 is involved in actin-mediated dynamics of late endocytic organelles, *Mol. Biol. Cell.* 16 (2005) 3873–3886. <https://doi.org/10.1091/mbc.E04-12-1105>.
- [112] M. Zhang, P. Liu, N.K. Dwyer, L.K. Christenson, T. Fujimoto, F. Martinez, M. Comly, J.A. Hanover, E. Joan Blanchette-Mackie, J.F. Strauss, MLN64 mediates mobilization of lysosomal cholesterol to steroidogenic mitochondria, *J. Biol. Chem.* 277 (2002) 33300–33310. <https://doi.org/10.1074/jbc.M200003200>.
- [113] C.P. Ponting, L. Aravind, START: a lipid-binding domain in StAR, HD-ZIP and signalling proteins, *Trends Biochem. Sci.* 24 (1999) 130–132. [https://doi.org/10.1016/S0968-0004\(99\)01362-6](https://doi.org/10.1016/S0968-0004(99)01362-6).

- [114] F. Alpy, C. Tomasetto, Give lipids a START: The StAR-related lipid transfer (START) domain in mammals, *J. Cell Sci.* 118 (2005) 2791–2801. <https://doi.org/10.1242/jcs.02485>.
- [115] D.B. Iaea, S. Mao, F.W. Lund, F.R. Maxfield, Role of STARD4 in sterol transport between the endocytic recycling compartment and the plasma membrane, *Mol. Biol. Cell.* 28 (2017) 1111–1122. <https://doi.org/10.1091/mbc.E16-07-0499>.
- [116] B. Mesmin, N.H. Pipalia, F.W. Lund, T.F. Ramlall, A. Sokolov, D. Eliezer, F.R. Maxfield, STARD4 abundance regulates sterol transport and sensing, *Mol. Biol. Cell.* 22 (2011) 4004–4015. <https://doi.org/10.1091/mbc.E11-04-0372>.
- [117] F. Alpy, C. Tomasetto, MLN64 and MENTHO, two mediators of endosomal cholesterol transport, *Biochem. Soc. Trans.* 34 (2006) 343–345. <https://doi.org/10.1042/BST0340343>.
- [118] L.P. Wilhelm, C. Wendling, B. Védie, T. Kobayashi, M. Chenard, C. Tomasetto, G. Drin, F. Alpy, STARD 3 mediates endoplasmic reticulum-to-endosome cholesterol transport at membrane contact sites, *EMBO J.* 36 (2017) 1412–1433. <https://doi.org/10.15252/emj.201695917>.
- [119] F. Borthwick, A.M. Allen, J.M. Taylor, A. Graham, Overexpression of STARD3 in human monocyte/macrophages induces an anti-atherogenic lipid phenotype, *Clin. Sci.* 119 (2010) 265–272. <https://doi.org/10.1042/CS20100266>.
- [120] E.R. Eden, The formation and function of ER-endosome membrane contact sites, *Biochim. Biophys. Acta - Mol. Cell Biol. Lipids.* 1861 (2016) 874–879. <https://doi.org/10.1016/j.bbalip.2016.01.020>.
- [121] C. Raiborg, E.M. Wenzel, H. Stenmark, ER–endosome contact sites: molecular compositions and functions, *EMBO J.* 34 (2015) 1848–1858. <https://doi.org/10.15252/emj.201591481>.
- [122] C. Raiborg, E.M. Wenzel, N.M. Pedersen, H. Olsvik, K.O. Schink, S.W. Schultz, M. Vietri, V. Nisi, C. Bucci, A. Brech, T. Johansen, H. Stenmark, Repeated ER-endosome contacts promote endosome translocation and neurite outgrowth, *Nature.* 520 (2015) 234–238. <https://doi.org/10.1038/nature14359>.
- [123] Y. Elbaz-Alon, Y. Guo, N. Segev, M. Harel, D.E. Quinnell, T. Geiger, O. Avinoam, D. Li, J. Nunnari, PDZD8 interacts with Protrudin and Rab7 at ER-late endosome membrane contact sites associated with mitochondria, *Nat. Commun.* 11 (2020) 1–14. <https://doi.org/10.1038/s41467-020-17451-7>.
- [124] Y. Gao, J. Xiong, Q.-Z. Chu, W.-K. Ji, PDZD8 mediated lipid transfer at ER-LE/lys contacts is required for LE/lys positioning and neurite outgrowth, 2021.
- [125] K. Kanerva, R.L. Uronen, T. Blom, S. Li, R. Bittman, P. Lappalainen, J. Peränen, G. Raposo, E. Ikonen, LDL Cholesterol Recycles to the Plasma Membrane via a Rab8a-Myosin5b-Actin-Dependent Membrane Transport Route, *Dev. Cell.* 27 (2013) 249–262. <https://doi.org/10.1016/j.devcel.2013.09.016>.
- [126] K. Takahashi, K. Kanerva, L. Vanharanta, L. Almeida-Souza, D. Lietha, V.M. Olkkonen, E. Ikonen, ORP2 couples LDL-cholesterol transport to FAK activation by endosomal cholesterol/PI(4,5)P<sub>2</sub> exchange, *EMBO J.* 40 (2021). <https://doi.org/10.15252/EMBJ.2020106871>.
- [127] A. Das, M.S. Brown, D.D. Anderson, J.L. Goldstein, A. Radhakrishnan, Three pools of plasma membrane cholesterol and their relation to cholesterol homeostasis, *Elife.* 2014 (2014). <https://doi.org/10.7554/eLife.02882>.
- [128] R.E. Infante, A. Radhakrishnan, Continuous transport of a small fraction of plasma membrane cholesterol to endoplasmic reticulum regulates total cellular cholesterol, *Elife.* 6 (2017). <https://doi.org/10.7554/eLife.25466>.

- [129] Y. Lange, T.L. Steck, Quantitation of the pool of cholesterol associated with Acyl-CoA. Cholesterol acyltransferase in human fibroblasts, *J. Biol. Chem.* 272 (1997) 13103–13108. <https://doi.org/10.1074/jbc.272.20.13103>.
- [130] M.N. Trinh, M.S. Brown, J.L. Goldstein, J. Han, G. Vale, J.G. McDonald, J. Seemann, J.T. Mendell, F. Lu, Last step in the path of LDL cholesterol from lysosome to plasma membrane to ER is governed by phosphatidylserine, *Proc. Natl. Acad. Sci. U. S. A.* 117 (2020) 18521–18529. <https://doi.org/10.1073/pnas.2010682117>.
- [131] D. V. Rajkumar V, C.R. Ferreira, W.A. Gahl, Lysosomal Storage Disease, *Metab. Dis. Found. Clin. Manag. Genet. Pathol.* (2021) 367–440. <https://doi.org/10.3233/978-1-61499-718-4-367>.
- [132] A.H. Futerman, G. Van Meer, The cell biology of lysosomal storage disorders, *Nat. Rev. Mol. Cell Biol.* 5 (2004) 554–565. <https://doi.org/10.1038/nrm1423>.
- [133] E. Lloyd-Evans, A.J. Morgan, X. He, D.A. Smith, E. Elliot-Smith, D.J. Silience, G.C. Churchill, E.H. Schuchman, A. Galione, F.M. Platt, Niemann-Pick disease type C1 is a sphingosine storage disease that causes deregulation of lysosomal calcium, *Nat. Med.* 14 (2008) 1247–1255. <https://doi.org/10.1038/nm.1876>.
- [134] P.G. Pentchev, M.E. Comly, H.S. Kruth, M.T. Vanier, D.A. Wenger, S. Patel, R.O. Brady, A defect in cholesterol esterification in Niemann-Pick disease (type C) patients, *Proc. Natl. Acad. Sci. U. S. A.* 82 (1985) 8247–8251. <https://doi.org/10.1073/pnas.82.23.8247>.
- [135] E.D. Carstea, J.A. Morris, K.G. Coleman, S.K. Loftus, D. Zhang, C. Cummings, J. Gu, M.A. Rosenfeld, W.J. Pavan, D.B. Krizman, J. Nagle, M.H. Polymeropoulos, S.L. Sturley, Y.A. Ioannou, M.E. Higgins, M. Comly, A. Cooney, A. Brown, C.R. Kaneski, E.J. Blanchette-Mackie, N.K. Dwyer, E.B. Neufeld, T.Y. Chang, L. Liscum, J.F. Strauss, K. Ohno, M. Zeigler, R. Carmi, J. Sokol, D. Markie, R.R. O'Neill, O.P. Van Diggelen, M. Elleder, M.C. Patterson, R.O. Brady, M.T. Vanier, P.G. Pentchev, D.A. Tagle, Niemann-Pick C1 disease gene: Homology to mediators of cholesterol homeostasis, *Science* (80-. ). 277 (1997) 228–231. <https://doi.org/10.1126/science.277.5323.228>.
- [136] E.J. Blanchette-Mackie, N.K. Dwyer, L.M. Amende, H.S. Kruth, J.D. Butler, J. Sokol, M.E. Comly, M.T. Vanier, J.T. August, R.O. Brady, P.G. Pentchev, Type-C Niemann-Pick disease: Low density lipoprotein uptake is associated with premature cholesterol accumulation in the Golgi complex and excessive cholesterol storage in lysosomes, *Proc. Natl. Acad. Sci. U. S. A.* 85 (1988) 8022–8026. <https://doi.org/10.1073/pnas.85.21.8022>.
- [137] J.E. Vance, Dysregulation of cholesterol balance in the brain: Contribution to neurodegenerative diseases, *DMM Dis. Model. Mech.* 5 (2012) 746–755. <https://doi.org/10.1242/dmm.010124>.
- [138] E. Meneses-Salas, A. García-Melero, K. Kanerva, P. Blanco-Muñoz, F. Morales-Paytuy, J. Bonjoch, J. Casas, A. Egert, S.S. Beevi, J. Jose, V. Llorente-Cortés, K.A. Rye, J. Heeren, A. Lu, A. Pol, F. Tebar, E. Ikonen, T. Grewal, C. Enrich, C. Rentero, Annexin A6 modulates TBC1D15/Rab7/StARD3 axis to control endosomal cholesterol export in NPC1 cells, *Cell. Mol. Life Sci.* 77 (2020) 2839–2857. <https://doi.org/10.1007/s00018-019-03330-y>.
- [139] C. Enrich, C. Rentero, T. Grewal, C.E. Futter, E.R. Eden, Cholesterol Overload: Contact Sites to the Rescue!, *Contact.* 2 (2019) 251525641989350. <https://doi.org/10.1177/2515256419893507>.
- [140] A. Lu, F. Hsieh, B.R. Sharma, S.R. Vaughn, C. Enrich, S.R. Pfeffer, CRISPR screens for lipid regulators reveal a role for ER-bound SNX13 in lysosomal cholesterol export, *J. Cell Biol.* 221 (2022). <https://doi.org/10.1083/jcb.202105060>.

- [141] A. Das, J.L. Goldstein, D.D. Anderson, M.S. Brown, A. Radhakrishnan, Use of mutant 125I-Perfringolysin O to probe transport and organization of cholesterol in membranes of animal cells, *Proc. Natl. Acad. Sci. U. S. A.* 110 (2013) 10580–10585. <https://doi.org/10.1073/pnas.1309273110>.
- [142] M. Skočaj, N. Resnik, M. Grundner, K. Ota, N. Rojko, V. Hodnik, G. Anderluh, A. Sobota, P. Maček, P. Veranič, K. Sepčić, Tracking cholesterol/sphingomyelin-rich membrane domains with the ostreolysin A-mCherry protein, *PLoS One.* 9 (2014) 92783. <https://doi.org/10.1371/journal.pone.0092783>.
- [143] K.A. Johnson, S. Endapally, D.C. Vazquez, R.E. Infante, A. Radhakrishnan, Ostreolysin A and anthrolysin O use different mechanisms to control movement of cholesterol from the plasma membrane to the endoplasmic reticulum, *J. Biol. Chem.* 294 (2019) 17289–17300. <https://doi.org/10.1074/jbc.RA119.010393>.
- [144] R.E. Soccio, R.M. Adams, K.N. Maxwell, J.L. Breslow, Differential gene regulation of StarD4 and StarD5 cholesterol transfer proteins: Activation of StarD4 by sterol regulatory element-binding protein-2 and StarD5 by endoplasmic reticulum stress, *J. Biol. Chem.* 280 (2005) 19410–19418. <https://doi.org/10.1074/jbc.M501778200>.
- [145] D. Rodriguez-Agudo, S. Ren, E. Wong, D. Marques, K. Redford, G. Gil, P. Hylemon, W.M. Pandak, Intracellular cholesterol transporter starD4 binds free cholesterol and increases cholesteryl ester formation, *J. Lipid Res.* 49 (2008) 1409–1419. <https://doi.org/10.1194/jlr.M700537-JLR200>.
- [146] T. Naito, B. Ercan, L. Krshnan, A. Triebel, D.H.Z. Koh, F.Y. Wei, K. Tomizawa, F.T. Torta, M.R. Wenk, Y. Saheki, Movement of accessible plasma membrane cholesterol by GRAMD1 lipid transfer protein complex, *Elife.* 8 (2019). <https://doi.org/10.7554/eLife.51401>.
- [147] B. Ercan, T. Naito, Y. Saheki, D. Hong, Z. Koh, D. Dharmawan, Molecular basis of accessible plasma membrane cholesterol recognition by the GRAM domain of GRAMD1b, (2021) 1–26. <https://doi.org/10.15252/embj.2020106524>.
- [148] M.J. Begley, G.S. Taylor, S.A. Kim, D.M. Veine, J.E. Dixon, J.A. Stuckey, Crystal Structure of a Phosphoinositide Phosphatase, MTMR2: Insights into Myotubular Myopathy and Charcot-Marie-Tooth Syndrome, *Mol. Cell.* 12 (2003) 1391–1402. [https://doi.org/10.1016/S1097-2765\(03\)00486-6](https://doi.org/10.1016/S1097-2765(03)00486-6).
- [149] T. Doerks, M. Strauss, M. Brendel, P. Bork, GRAM, a novel domain in glucosyltransferases, myotubularins and other putative membrane-associated proteins, *Trends Biochem. Sci.* 25 (2000) 483–485. [https://doi.org/10.1016/S0968-0004\(00\)01664-9](https://doi.org/10.1016/S0968-0004(00)01664-9).
- [150] J. Sandhu, S. Li, L. Fairall, S.G. Pfisterer, J.E. Gurnett, X. Xiao, T.A. Weston, D. Vashi, A. Ferrari, J.L. Orozco, C.L. Hartman, D. Strugatsky, S.D. Lee, C. He, C. Hong, H. Jiang, L.A. Bentolila, A.T. Gatta, T.P. Levine, A. Ferng, R. Lee, D.A. Ford, S.G. Young, E. Ikonen, J.W.R. Schwabe, P. Tontonoz, Aster Proteins Facilitate Nonvesicular Plasma Membrane to ER Cholesterol Transport in Mammalian Cells, *Cell.* 175 (2018) 514–529.e20. <https://doi.org/10.1016/j.cell.2018.08.033>.
- [151] J. Tong, M.K. Manik, Y.J. Im, Structural basis of sterol recognition and nonvesicular transport by lipid transfer proteins anchored at membrane contact sites, *Proc. Natl. Acad. Sci. U. S. A.* 115 (2018) E856–E865. <https://doi.org/10.1073/pnas.1719709115>.
- [152] F.A. Horenkamp, D.P. Valverde, J. Nunnari, K.M. Reinisch, Molecular basis for sterol transport by St ART-like lipid transfer domains, *EMBO J.* 37 (2018) 1–15. <https://doi.org/10.15252/embj.201798002>.
- [153] V.I. Kutyavin, A. Chawla, Aster: A New Star in Cholesterol Trafficking, *Cell.* 175 (2018) 307–309. <https://doi.org/10.1016/j.cell.2018.09.025>.

- [154] M. Marek, V. Vincenzetti, S.G. Martin, Sterol biosensor reveals LAM-family Ltc1-dependent sterol flow to endosomes upon Arp2/3 inhibition, *J. Cell Biol.* 219 (2020). <https://doi.org/10.1083/jcb.202001147>.
- [155] J.P. Andersen, J. Zhang, H. Sun, X. Liu, J. Liu, J. Nie, Y. Shi, Aster-B coordinates with Arf1 to regulate mitochondrial cholesterol transport, *Mol. Metab.* 42 (2020) 101055. <https://doi.org/10.1016/j.molmet.2020.101055>.
- [156] Y. Elbaz-Alon, M. Eisenberg-Bord, V. Shinder, S.B. Stiller, E. Shimoni, N. Wiedemann, T. Geiger, M. Schuldiner, Lam6 Regulates the Extent of Contacts between Organelles, *Cell Rep.* 12 (2015) 7–14. <https://doi.org/10.1016/j.celrep.2015.06.022>.
- [157] M. Hölttä-Vuori, R.L. Uronen, J. Repakova, E. Salonen, I. Vattulainen, P. Panula, Z. Li, R. Bittman, E. Ikonen, BODIPY-cholesterol: A new tool to visualize sterol trafficking in living cells and organisms, *Traffic.* 9 (2008) 1839–1849. <https://doi.org/10.1111/j.1600-0854.2008.00801.x>.
- [158] E. Sezgin, F.B. Can, F. Schneider, M.P. Clausen, S. Galiani, T.A. Stanly, D. Waithe, A. Colaco, A. Honigmann, D. Wüstner, F. Platt, C. Eggeling, A comparative study on fluorescent cholesterol analogs as versatile cellular reporters, *J. Lipid Res.* 57 (2016) 299–309. <https://doi.org/10.1194/jlr.M065326>.
- [159] L.L. Listenberger, D.A. Brown, Fluorescent Detection of Lipid Droplets and Associated Proteins, *Curr. Protoc. Cell Biol.* 35 (2007) 24.2.1–24.2.11. <https://doi.org/10.1002/0471143030.cb2402s35>.
- [160] J. Spandl, D.J. White, J. Peychl, C. Thiele, Live cell multicolor imaging of lipid droplets with a new dye, LD540, *Traffic.* 10 (2009) 1579–1584. <https://doi.org/10.1111/j.1600-0854.2009.00980.x>.
- [161] D. Wüstner, F.W. Lund, C. Röhr, H. Stangl, Potential of BODIPY-cholesterol for analysis of cholesterol transport and diffusion in living cells Memorial Issue to Robert Bittman in Chemistry and Physics of Lipids, *Chem. Phys. Lipids.* 194 (2016) 12–28. <https://doi.org/10.1016/j.chemphyslip.2015.08.007>.
- [162] D. Wüstner, K. Solanko, How cholesterol interacts with proteins and lipids during its intracellular transport, *Biochim. Biophys. Acta - Biomembr.* 1848 (2015) 1908–1926. <https://doi.org/10.1016/j.bbamem.2015.05.010>.
- [163] T.J. Kim, Q. Wang, M. Shelor, G. Pratz, Single-cell radioluminescence microscopy with two-fold higher sensitivity using dual scintillator configuration, *PLoS One.* 15 (2020) 1–11. <https://doi.org/10.1371/journal.pone.0221241>.
- [164] B.R. Martin, B.F. Cravatt, Large-scale profiling of protein palmitoylation in mammalian cells, *Nat. Methods.* 6 (2009) 135–138. <https://doi.org/10.1038/nmeth.1293>.
- [165] M.D. Best, M.M. Rowland, H.E. Bostic, Exploiting bioorthogonal chemistry to elucidate protein-lipid binding interactions and other biological roles of phospholipids, *Acc. Chem. Res.* 44 (2011) 686–698. <https://doi.org/10.1021/ar200060y>.
- [166] C.Y. Jao, M. Roth, R. Welti, A. Salic, Metabolic labeling and direct imaging of choline phospholipids in vivo, *Proc. Natl. Acad. Sci. U. S. A.* 106 (2009) 15332–15337. <https://doi.org/10.1073/pnas.0907864106>.
- [167] J.J. Hulce, A.B. Cognetta, M.J. Niphakis, S.E. Tully, B.F. Cravatt, Proteome-wide mapping of cholesterol-interacting proteins in mammalian cells, *Nat. Methods.* 10 (2013) 259–264. <https://doi.org/10.1038/nmeth.2368>.
- [168] K. Hofmann, C. Thiele, H.-F. Schött, A. Gaebler, M. Schoene, Y. Kiver, S. Friedrichs, D. Lütjohann, L. Kuerschner, A novel alkyne cholesterol to trace cellular cholesterol metabolism and localization, *J. Lipid Res.* 55 (2014) 583–591. <https://doi.org/10.1194/jlr.D044727>.

- [169] C.Y. Jao, D. Nedelcu, L. V Lopez, T.N. Samarakoon, R. Welti, A. Salic Adrian Salic, Bioorthogonal probes for imaging sterols in cells HHS Public Access, *Chembiochem.* 16 (2015) 611–617. <https://doi.org/10.1002/cbic.201402715>.
- [170] C. Thiele, M.J. Hannah, F. Fahrenholz, W.B. Huttner, Cholesterol binds to synaptophysin and is required for biogenesis of synaptic vesicles, *Nat. Cell Biol.* 2 (2000) 42–49. <https://doi.org/10.1038/71366>.
- [171] J.C. Cruz, M. Thomas, E. Wong, N. Ohgami, S. Sugii, T. Curphey, C.C.Y. Chang, T.Y. Chang, Synthesis and biochemical properties of a new photoactivatable cholesterol analog 7,7-azocholestanol and its linoleate ester in Chinese hamster ovary cell lines, *J. Lipid Res.* 43 (2002) 1341–1347. <https://doi.org/10.1194/jlr.m200015-jlr200>.
- [172] S. Charrin, S. Manié, C. Thiele, M. Billard, D. Gerlier, C. Boucheix, E. Rubinstein, A physical and functional link between cholesterol and tetraspanins, *Eur. J. Immunol.* 33 (2003) 2479–2489. <https://doi.org/10.1002/eji.200323884>.
- [173] B.M. Castellano, A.M. Thelen, O. Moldavski, M. Feltes, R.E.N. van der Welle, L. Mydock-McGrane, X. Jiang, R.J. van Eijkeren, O.B. Davis, S.M. Louie, R.M. Perera, D.F. Covey, D.K. Nomura, D.S. Ory, R. Zoncu, Lysosomal cholesterol activates mTORC1 via an SLC38A9–Niemann-Pick C1 signaling complex, *Science* (80-. ). 355 (2017) 1306–1311. <https://doi.org/10.1126/science.aag1417>.
- [174] M.M. Budelier, W.W.L. Cheng, L. Bergdoll, Z.W. Chen, J.W. Janetka, J. Abramson, K. Krishnan, L. Mydock-McGrane, D.F. Covey, J.P. Whitelegge, A.S. Evers, Photoaffinity labeling with cholesterol analogues precisely maps a cholesterol-binding site in voltage-dependent anion channel-1, *J. Biol. Chem.* 292 (2017) 9294–9304. <https://doi.org/10.1074/jbc.M116.773069>.
- [175] M. Feltes, S. Moores, S.E. Gale, K. Krishnan, L. Mydock-McGrane, D.F. Covey, D.S. Ory, J.E. Schaffer, Synthesis and characterization of diazine alkyne probes for the study of intracellular cholesterol trafficking, *J. Lipid Res.* 60 (2019) 707–716. <https://doi.org/10.1194/jlr.D091470>.
- [176] N. Chauhan, Y.Y. Sere, A.M. Sokol, J. Graumann, A.K. Menon, A PhotoClick cholesterol-based quantitative proteomics screen for cytoplasmic sterol-binding proteins in *Saccharomyces cerevisiae*, *Yeast.* 37 (2020) 15–25. <https://doi.org/10.1002/yea.3448>.
- [177] B. Hu, C.T. Höfer, C. Thiele, M. Veit, Cholesterol Binding to the Transmembrane Region of a Group 2 Hemagglutinin (HA) of Influenza Virus Is Essential for Virus Replication, Affecting both Virus Assembly and HA Fusion Activity, *J. Virol.* 93 (2019) 1–23. <https://doi.org/10.1128/jvi.00555-19>.
- [178] D. Höglinger, A. Nadler, P. Haberkant, J. Kirkpatrick, M. Schifferer, F. Stein, S. Hauke, F.D. Porter, C. Schultz, Trifunctional lipid probes for comprehensive studies of single lipid species in living cells, *Proc. Natl. Acad. Sci. U. S. A.* 114 (2017) 1566–1571. <https://doi.org/10.1073/pnas.1611096114>.
- [179] D. Höglinger, A. Nadler, C. Schultz, Caged lipids as tools for investigating cellular signaling, *Biochim. Biophys. Acta - Mol. Cell Biol. Lipids.* 1841 (2014) 1085–1096. <https://doi.org/10.1016/j.bbalip.2014.03.012>.
- [180] N. Wagner, M. Stephan, D. Höglinger, A. Nadler, A Click Cage: Organelle-Specific Uncaging of Lipid Messengers, *Angew. Chemie - Int. Ed.* 57 (2018) 13339–13343. <https://doi.org/10.1002/anie.201807497>.
- [181] S. Feng, T. Harayama, D. Chang, J.T. Hannich, N. Winssinger, H. Riezman, Lysosome-targeted photoactivation reveals local sphingosine metabolism signatures, *Chem. Sci.* 10 (2019) 2253–2258. <https://doi.org/10.1039/C8SC03614D>.

- [182] J. Altuzar, J. Notbohm, F. Stein, P. Haberkant, S. Heybrock, J. Worsch, P. Saftig, D. Höglinger, Lysosome-targeted lipid probes reveal sterol transporters NPC1 and LIMP-2 as sphingosine transporters, (2021). <https://doi.org/10.1101/2021.11.10.468010>.
- [183] L. Voilquin, M. Lodi, T. Di Mattia, M.-P. Chenard, C. Mathelin, F. Alpy, C. Tomasetto, STARD3: A Swiss Army Knife for Intracellular Cholesterol Transport, *Contact*. 2 (2019) 251525641985673. <https://doi.org/10.1177/2515256419856730>.
- [184] R. Stoica, K.J. De Vos, S. Paillusson, S. Mueller, R.M. Sancho, K.F. Lau, G. Vizcay-Barrena, W.L. Lin, Y.F. Xu, J. Lewis, D.W. Dickson, L. Petrucelli, J.C. Mitchell, C.E. Shaw, C.C.J. Miller, ER-mitochondria associations are regulated by the VAPB-PTPIP51 interaction and are disrupted by ALS/FTD-associated TDP-43, *Nat. Commun.* 5 (2014) 3996. <https://doi.org/10.1038/ncomms4996>.
- [185] K.J. De vos, G.M. Mórotz, R. Stoica, E.L. Tudor, K.F. Lau, S. Ackerley, A. Warley, C.E. Shaw, C.C.J. Miller, VAPB interacts with the mitochondrial protein PTPIP51 to regulate calcium homeostasis, *Hum. Mol. Genet.* 21 (2012) 1299–1311. <https://doi.org/10.1093/hmg/ddr559>.
- [186] P. Gomez-Suaga, S. Paillusson, R. Stoica, W. Noble, D.P. Hanger, C.C.J. Miller, The ER-Mitochondria Tethering Complex VAPB-PTPIP51 Regulates Autophagy, *Curr. Biol.* 27 (2017) 371–385. <https://doi.org/10.1016/j.cub.2016.12.038>.
- [187] M.J. Phillips, G.K. Voeltz, Structure and function of ER membrane contact sites with other organelles, *Nat. Rev. Mol. Cell Biol.* 17 (2016) 69–82. <https://doi.org/10.1038/nrm.2015.8>.
- [188] I. Weidenfeld, M. Gossen, R. Löw, D. Kentner, S. Berger, D. Görlich, D. Bartsch, H. Bujard, K. Schönig, Inducible expression of coding and inhibitory RNAs from retargetable genomic loci, *Nucleic Acids Res.* 37 (2009) e50–e50. <https://doi.org/10.1093/nar/gkp108>.
- [189] J. Liu, Y. Wang, L. Song, L. Zeng, W. Yi, T. Liu, H. Chen, M. Wang, Z. Ju, Y.S. Cong, A critical role of DDRGK1 in endoplasmic reticulum homeostasis via regulation of IRE1 $\alpha$  stability, *Nat. Commun.* 8 (2017). <https://doi.org/10.1038/ncomms14186>.
- [190] F. Hensen, A. Moretton, S. Van Esveld, G. Farge, J.N. Spelbrink, The mitochondrial outer-membrane location of the EXD2 exonuclease contradicts its direct role in nuclear DNA repair, *Sci. Rep.* 8 (2018) 1–9. <https://doi.org/10.1038/s41598-018-23690-y>.
- [191] J.S. Cheah, S. Yamada, A Simple Elution Strategy for Biotinylated Proteins Bound to Streptavidin Conjugated Beads using Excess Biotin and Heat, *Biochem. Biophys. Res. Commun.* 493 (2017) 1522–1527. <https://doi.org/10.1016/j.bbrc.2017.09.168>.
- [192] R. Hua, D. Cheng, É. Coyaud, S. Freeman, E. Di Pietro, Y. Wang, A. Vissa, C.M. Yip, G.D. Fairn, N. Braverman, J.H. Brumell, W.S. Trimble, B. Raught, P.K. Kim, VAPs and ACBD5 tether peroxisomes to the ER for peroxisome maintenance and lipid homeostasis, *J. Cell Biol.* 216 (2017) 367–377. <https://doi.org/10.1083/jcb.201608128>.
- [193] C. Chen, J. Li, X. Qin, W. Wang, Peroxisomal Membrane Contact Sites in Mammalian Cells, *Front. Cell Dev. Biol.* 8 (2020) 1–9. <https://doi.org/10.3389/fcell.2020.00512>.
- [194] M. Mattiazzi Ušaj, M. Brložnik, P. Kaferle, M. Žitnik, H. Wolinski, F. Leitner, S.D. Kohlwein, B. Zupan, U. Petrovič, Genome-Wide Localization Study of Yeast Pex11 Identifies Peroxisome–Mitochondria Interactions through the ERMES Complex, *J. Mol. Biol.* 427 (2015) 2072–2087. <https://doi.org/10.1016/j.jmb.2015.03.004>.
- [195] N. Shai, M. Schuldiner, E. Zalckvar, No peroxisome is an island - Peroxisome contact sites, *Biochim. Biophys. Acta - Mol. Cell Res.* 1863 (2016) 1061–1069. <https://doi.org/10.1016/j.bbamcr.2015.09.016>.

- [196] J.L. Jacobs, J. Zhu, S.N. Sarkar, C.B. Coyne, Regulation of mitochondrial antiviral signaling (MAVS) expression and signaling by the mitochondria-associated endoplasmic reticulum membrane (MAM) protein Gp78, *J. Biol. Chem.* 289 (2014) 1604–1616. <https://doi.org/10.1074/jbc.M113.520254>.
- [197] J.R. Liang, E. Lingeman, T. Luong, S. Ahmed, M. Muhar, T. Nguyen, J.A. Olzmann, J.E. Corn, A Genome-wide ER-phagy Screen Highlights Key Roles of Mitochondrial Metabolism and ER-Resident UFMylation, *Cell.* 180 (2020) 1160-1177.e20. <https://doi.org/10.1016/j.cell.2020.02.017>.
- [198] B.B. Chu, Y.C. Liao, W. Qi, C. Xie, X. Du, J. Wang, H. Yang, H.H. Miao, B.L. Li, B.L. Song, Cholesterol transport through lysosome-peroxisome membrane contacts, *Cell.* 161 (2015) 291–306. <https://doi.org/10.1016/j.cell.2015.02.019>.
- [199] S. Cocklin, M. Jost, N.M. Robertson, S.D. Weeks, H.W. Weber, E. Young, S. Seal, C. Zhang, E. Mosser, P.J. Loll, A.J. Saunders, R.F. Rest, I.M. Chaiken, Real-time monitoring of the membrane-binding and insertion properties of the cholesterol-dependent cytolysin anthrolysin O from *Bacillus anthracis*, *J. Mol. Recognit.* 19 (2006) 354–362. <https://doi.org/10.1002/jmr.784>.
- [200] A. Ferrari, C. He, J.P. Kennelly, J. Sandhu, X. Xiao, X. Chi, H. Jiang, S.G. Young, P. Tontonoz, Aster Proteins Regulate the Accessible Cholesterol Pool in the Plasma Membrane, *Mol. Cell. Biol.* 40 (2020). <https://doi.org/10.1128/mcb.00255-20>.
- [201] S. Endapally, R.E. Infante, A. Radhakrishnan, Monitoring and modulating intracellular cholesterol trafficking using ALOD4, a cholesterol-binding protein, *Methods Mol. Biol.* 1949 (2019) 153–163. [https://doi.org/10.1007/978-1-4939-9136-5\\_12](https://doi.org/10.1007/978-1-4939-9136-5_12).
- [202] D. Wüstner, M. Mondal, I. Tabas, F.R. Maxfield, Direct observation of rapid internalization and intracellular transport of sterol by macrophage foam cells, *Traffic.* 6 (2005) 396–412. <https://doi.org/10.1111/j.1600-0854.2005.00285.x>.
- [203] M. Hao, S.X. Lin, O.J. Karylowski, D.W. Stner, T.E. McGraw, F.R. Maxfield, Vesicular and non-vesicular sterol transport in living cells: The endocytic recycling compartment is a major sterol storage organelle, *J. Biol. Chem.* 277 (2002) 609–617. <https://doi.org/10.1074/jbc.M108861200>.
- [204] J. Béthune, C.G. Artus-Revel, W. Filipowicz, Kinetic analysis reveals successive steps leading to miRNA-mediated silencing in mammalian cells, *EMBO Rep.* 13 (2012) 716–723. <https://doi.org/10.1038/embor.2012.82>.
- [205] A.K. Tharkeshwar, J. Trekker, W. Vermeire, J. Pauwels, R. Sannerud, D.A. Priestman, D. Te Vruchte, K. Vints, P. Baatsen, J.P. Decuypere, H. Lu, S. Martin, P. Vangheluwe, J. V. Swinnen, L. Lagae, F. Impens, F.M. Platt, K. Gevaert, W. Annaert, A novel approach to analyze lysosomal dysfunctions through subcellular proteomics and lipidomics: The case of NPC1 deficiency, *Sci. Rep.* 7 (2017) 1–20. <https://doi.org/10.1038/srep41408>.
- [206] N. Dyballa, S. Metzger, Fast and sensitive colloidal Coomassie G-250 staining for proteins in polyacrylamide gels, *J. Vis. Exp.* (2009) 2–5. <https://doi.org/10.3791/1431>.
- [207] A. Gay, D. Rye, A. Radhakrishnan, Switch-like responses of two cholesterol sensors do not require protein oligomerization in membranes, *Biophys. J.* 108 (2015) 1459–1469. <https://doi.org/10.1016/j.bpj.2015.02.008>.
- [208] V. Schoop, Supplementary Data to the Dissertation “Proximity biotinylation at organelle contact sites reveals GRAMD1B as a sterol transporter acting at the lysosome-ER interface,” (2022). <https://doi.org/10.17632/6k3ft58vb2.1>. <https://data.mendeley.com/datasets/6k3ft58vb2/1>.

## Appendix

Supplementary data can be found under the digital object identifier (DOI)

[10.17632/6k3ft58vb2.1](https://doi.org/10.17632/6k3ft58vb2.1) or under <https://data.mendeley.com/datasets/6k3ft58vb2/1> [208]

### Digitally provided data includes:

- Result-files of MS-spectral analysis using Max-Quant Result files
- Comparative GO-term analysis of proteomic datasets
- Detailed list of proteins identified in all three screens (also shown below)
- Videos of LDL particles in GFP-Gramd1B-expressing cells (raw and processed)
- ImageJ Macro-Script used to analyze LDL/GFP data (also shown below)
- DNA-maps of all plasmids mentioned in this thesis
- High-resolution versions of all figures

### Detailed list of proteins identified in all three screens

Screen	Gene name	Protein name	Uniprot ID
1, Lyso-ER	ACBD5	Acyl-CoA-binding domain-containing protein 5	B7Z2R7
1, Lyso-ER	ACSL3 ACS3	Fatty acid CoA ligase Acsl3	O95573
1, Lyso-ER	ANKLE2 KIAA0692	Ankyrin repeat and LEM domain-containing protein 2	Q86XL3
1, Lyso-ER	AUP1	Lipid droplet-regulating VLDL assembly factor AUP1	Q9Y679
1, Lyso-ER	BRAP	BRCA1-associated protein	J3KNN7
1, Lyso-ER	CCDC47 GK001	PAT complex subunit CCDC47	Q96A33
1, Lyso-ER	DDRGK1 C20orf116	DDRGK domain-containing protein 1	Q96HY6
1, Lyso-ER	FAF2 ETEA	FAS-associated factor 2	Q96CS3
1, Lyso-ER	FASTKD2 KIAA0971	FAST kinase domain-containing protein 2, mitochondrial	Q9NYY8
1, Lyso-ER	GRAMD1B hCG_39893	Protein Aster-B, HCG39893, isoform CRA_a	A0A024R3 M2
1, Lyso-ER	INF2 C14orf151	Inverted formin-2	Q27J81
1, Lyso-ER	LPCAT2 AGPAT11	Lysophosphatidylcholine acyltransferase 2	Q7L5N7
1, Lyso-ER	LRSAM1 TAL	E3 ubiquitin-protein ligase LRSAM1	Q6UWE0
1, Lyso-ER	LSG1	Large subunit GTPase 1 homolog	Q9H089
1, Lyso-ER	MOSPD2	Motile sperm domain-containing protein 2	Q8NHP6
1, Lyso-ER	NUP155 KIAA0791	Nuclear pore complex protein Nup155	O75694
1, Lyso-ER	OSBP OSBP1	Oxysterol-binding protein 1	P22059
1, Lyso-ER	OSBPL10 ORP10	Oxysterol-binding protein-related protein 10	Q9BXB5
1, Lyso-ER	OSBPL3 KIAA0704	Oxysterol-binding protein-related protein 3	Q9H4L5
1, Lyso-ER	OSBPL8 KIAA1451	Oxysterol-binding protein-related protein 8	Q9BZF1
1, Lyso-ER	OSBPL9 ORP9	Oxysterol-binding protein-related protein 9	Q96SU4
1, Lyso-ER	PTPN1 PTP1B	Tyrosine-protein phosphatase non-receptor type 1	P18031
1, Lyso-ER	RAB3GAP2 KIAA0839	Rab3 GTPase-activating protein non-catalytic subunit	Q9H2M9
1, Lyso-ER	SLC16A1 MCT1	Monocarboxylate transporter 1	P53985

1, Lyso-ER	SPTLC1 LCB1	Serine palmitoyltransferase 1	O15269
1, Lyso-ER	SQSTM1 ORCA	Sequestosome-1	Q13501
1, Lyso-ER	ST13	Hsc70-interacting protein	H7C3I1
1, Lyso-ER	STARD3 CAB1	StAR-related lipid transfer protein 3	Q14849
1, Lyso-ER	SUN1 KIAA0810	SUN domain-containing protein 1	O94901
1, Lyso-ER	TRPM7 hCG_39859	Non-specific serine/threonine protein kinase	H0YLN8
1, Lyso-ER	UBXN4 KIAA0242	UBX domain-containing protein 4	Q92575
1, Lyso-ER	USP33 KIAA1097	Ubiquitin carboxyl-terminal hydrolase 33	Q8TEY7
1, Lyso-ER	VAPA VAP33	Vesicle-associated membrane protein-associated protein A	Q9P0L0
1, Lyso-ER	VAPB UNQ484/PRO983	Vesicle-associated membrane protein-associated protein B/C	O95292
1, Lyso-ER	VPS13A CHAC	Vacuolar protein sorting-associated protein 13A	Q96RL7
1, Lyso-ER	VPS13C KIAA1421	Vacuolar protein sorting-associated protein 13C	Q709C8
1, Lyso-ER	ZDBF2 KIAA1571	DBF4-type zinc finger-containing protein 2	Q9HCK1

1, Mito-ER	ACBD5	Acyl-CoA-binding domain-containing protein 5	B7Z2R7
1, Mito-ER	ACSL3 ACS3	Fatty acid CoA ligase Acsl3	O95573
1, Mito-ER	AUP1	Lipid droplet-regulating VLDL assembly factor AUP1	Q9Y679
1, Mito-ER	BRAP	BRCA1-associated protein	J3KNN7
1, Mito-ER	CCDC47 GK001	PAT complex subunit CCDC47	Q96A33
1, Mito-ER	CPT1A CPT1	Carnitine O-palmitoyltransferase 1, liver isoform	P50416
1, Mito-ER	DDRKG1 C20orf116	DDRKG domain-containing protein 1	Q96HY6
1, Mito-ER	EXD2 C14orf114	Exonuclease 3'-5' domain-containing protein 2	Q9NVH0
1, Mito-ER	FAF2 ETEA	FAS-associated factor 2	Q96CS3
1, Mito-ER	HBS1L HBS1	HBS1-like protein	Q9Y450
1, Mito-ER	HLA-C HLAC	HLA class I histocompatibility antigen, C alpha chain	P10321
1, Mito-ER	LSG1	Large subunit GTPase 1 homolog	Q9H089
1, Mito-ER	MAVS IPS1	Mitochondrial antiviral-signaling protein	Q7Z434
1, Mito-ER	MOSPD2	Motile sperm domain-containing protein 2	Q8NHP6
1, Mito-ER	NUP155 KIAA0791	Nuclear pore complex protein Nup155	O75694
1, Mito-ER	OSBP OSBP1	Oxysterol-binding protein 1	P22059
1, Mito-ER	OSBPL10 ORP10	Oxysterol-binding protein-related protein 10	Q9BXB5
1, Mito-ER	OSBPL3 KIAA0704	Oxysterol-binding protein-related protein 3	Q9H4L5
1, Mito-ER	OSBPL9 ORP9	Oxysterol-binding protein-related protein 9	Q96SU4
1, Mito-ER	PTPN1 PTP1B	Tyrosine-protein phosphatase non-receptor type 1	P18031
1, Mito-ER	RMDN3 FAM82A2	Regulator of microtubule dynamics protein 3	Q96TC7
1, Mito-ER	SLC16A1 MCT1	Monocarboxylate transporter 1	P53985
1, Mito-ER	SQSTM1 ORCA	Sequestosome-1	Q13501
1, Mito-ER	ST13	Hsc70-interacting protein	H7C3I1
1, Mito-ER	STIM1	Stromal interaction molecule 1	E9PNJ4
1, Mito-ER	UBB	Polyubiquitin-B	J3QS39
1, Mito-ER	USP33 KIAA1097	Ubiquitin carboxyl-terminal hydrolase 33	Q8TEY7
1, Mito-ER	VAPA VAP33	Vesicle-associated membrane protein-associated protein A	Q9P0L0
1, Mito-ER	VAPB UNQ484/PRO983	Vesicle-associated membrane protein-associated protein B/C	O95292

1, Mito-ER	VPS13A CHAC	Vacuolar protein sorting-associated protein 13A	Q96RL7
1, Mito-ER	VPS13C KIAA1421	Vacuolar protein sorting-associated protein 13C	Q709C8
1, Mito-ER	ZW10	Centromere/kinetochore protein zw10 homolog	O43264
1, Endo-ER	ACBD5	Acyl-CoA-binding domain-containing protein 5	B7Z2R7
1, Endo-ER	ACSL3 ACS3	Fatty acid CoA ligase Acsl3	O95573
1, Endo-ER	ANKLE2 KIAA0692	Ankyrin repeat and LEM domain-containing protein 2	Q86XL3
1, Endo-ER	AP2A1 ADTAA	AP-2 complex subunit alpha-1	O95782
1, Endo-ER	AUP1	Lipid droplet-regulating VLDL assembly factor AUP1	Q9Y679
1, Endo-ER	BRAP	BRCA1-associated protein	J3KNN7
1, Endo-ER	CANX	Calnexin	P27824
1, Endo-ER	CCDC47 GK001	PAT complex subunit CCDC47	Q96A33
1, Endo-ER	CLU APOJ CLI	Clusterin	P10909
1, Endo-ER	DDRKG1 C20orf116	DDRKG domain-containing protein 1	Q96HY6
1, Endo-ER	EGFR ERBB	Epidermal growth factor receptor	P00533
1, Endo-ER	EIF3F EIF3S5	Eukaryotic translation initiation factor 3 subunit F	O00303
1, Endo-ER	FAF2 ETEA	FAS-associated factor 2	Q96CS3
1, Endo-ER	GRAMD1B	HCG39893, isoform CRA_a	A0A024R3 M2
1, Endo-ER	HBS1L HBS1	HBS1-like protein	Q9Y450
1, Endo-ER	LPCAT2 AGPAT11	Lysophosphatidylcholine acyltransferase 2	Q7L5N7
1, Endo-ER	LRPPRC LRP130	Leucine-rich PPR motif-containing protein, mitochondrial	P42704
1, Endo-ER	LSG1	Large subunit GTPase 1 homolog	Q9H089
1, Endo-ER	MACO1 TMEM57	Macoilin	Q8N5G2
1, Endo-ER	NDC1 TMEM48	Nucleoporin NDC1	Q9BTX1
1, Endo-ER	NSDHL H105E3	Sterol-4-alpha-carboxylate 3-dehydrogenase	Q15738
1, Endo-ER	NUP155 KIAA0791	Nuclear pore complex protein Nup155	O75694
1, Endo-ER	OSBP OSBP1	Oxysterol-binding protein 1	P22059
1, Endo-ER	OSBPL8 KIAA1451	Oxysterol-binding protein-related protein 8	Q9BZF1
1, Endo-ER	OSBPL9 ORP9	Oxysterol-binding protein-related protein 9	Q96SU4
1, Endo-ER	PLOD1 LLH	Procollagen-lysine,2-oxoglutarate 5-dioxygenase 1	Q02809
1, Endo-ER	PTPN1 PTP1B	Tyrosine-protein phosphatase non-receptor type 1	P18031
1, Endo-ER	RAB3GAP2 KIAA0839	Rab3 GTPase-activating protein non-catalytic subunit	Q9H2M9
1, Endo-ER	SOAT1 AACT	Sterol O-acyltransferase 1	P35610
1, Endo-ER	SPTLC1 LCB1	Serine palmitoyltransferase 1	O15269
1, Endo-ER	SRP54	Signal recognition particle 54 kDa protein	P61011
1, Endo-ER	ST13	Hsc70-interacting protein	H7C3I1
1, Endo-ER	TECR GPSN2	Very-long-chain enoyl-CoA reductase	Q9NZ01
1, Endo-ER	TMEM131 KIAA0257	Transmembrane protein 131	Q92545
1, Endo-ER	TMX1 TMX TXNDC	Thioredoxin-related transmembrane protein 1	Q9H3N1
1, Endo-ER	TRPM7 hCG_39859	Non-specific serine/threonine protein kinase	H0YLN8
1, Endo-ER	UBXN4 KIAA0242	UBX domain-containing protein 4	Q92575
1, Endo-ER	UFL1 KIAA0776	E3 UFM1-protein ligase 1	O94874
1, Endo-ER	USO1 VDP	General vesicular transport factor p115	O60763
1, Endo-ER	USP33 KIAA1097	Ubiquitin carboxyl-terminal hydrolase 33	Q8TEY7

1, Endo-ER	VAPA VAP33	Vesicle-associated membrane protein-associated protein A	Q9P0L0
1, Endo-ER	VPS13C KIAA1421	Vacuolar protein sorting-associated protein 13C	Q709C8
2, Lyso-ER	ACBD5 KIAA1996	Acyl-CoA-binding domain-containing protein 5	Q5T8D3
2, Lyso-ER	ASS1 ASS	Argininosuccinate synthase	P00966
2, Lyso-ER	ATN1 D12S755E	Atrophin-1	P54259
2, Lyso-ER	ATP1A1	Sodium/potassium-transporting ATPase subunit alpha-1	P05023
2, Lyso-ER	CANX	Calnexin	P27824
2, Lyso-ER	DDRGK1 C20orf116	DDRGK domain-containing protein 1	Q96HY6
2, Lyso-ER	ESYT1 FAM62A	Extended synaptotagmin-1	Q9BSJ8
2, Lyso-ER	HSPA8 HSC70	Heat shock cognate 71 kDa protein	P11142
2, Lyso-ER	IPO5 KPNB3	Importin-5	O00410
2, Lyso-ER	KTN1 CG1 KIAA0004	Kinectin	Q86UP2
2, Lyso-ER	TMPO LAP2	Lamina-associated polypeptide 2, isoform alpha	P42166
2, Lyso-ER	LEMD3 MAN1	Inner nuclear membrane protein Man1	Q9Y2U8
2, Lyso-ER	LRBA BGL CDC4L	Lipopolysaccharide-responsive and beige-like anchor protein	P50851
2, Lyso-ER	NDUFS1	NADH-ubiquinone oxidoreductase 75 kDa subunit	P28331
2, Lyso-ER	PCCB	Propionyl-CoA carboxylase beta chain, mitochondrial	P05166
2, Lyso-ER	PSMC2 MSS1	26S proteasome regulatory subunit 7	P35998
2, Lyso-ER	PTPN1 PTP1B	Tyrosine-protein phosphatase non-receptor type 1	P18031
2, Lyso-ER	RFC1 RFC140	Replication factor C subunit 1	P35251
2, Lyso-ER	RMDN3 FAM82A2	Regulator of microtubule dynamics protein 3	Q96TC7
2, Lyso-ER	RPSA LAMBR	40S ribosomal protein SA	P08865
2, Lyso-ER	RUVBL1 INO80H	RuvB-like 1	Q9Y265
2, Lyso-ER	STARD3 CAB1	StAR-related lipid transfer protein 3	Q14849
2, Lyso-ER	UGDH	UDP-glucose 6-dehydrogenase	O60701
2, Lyso-ER	VAPA VAP33	Vesicle-associated membrane protein-associated protein A	Q9P0L0
2, Lyso-ER	VAPB UNQ484/PRO983	Vesicle-associated membrane protein-associated protein B/C	O95292
2, Mito-ER	ABCD1 ALD	ATP-binding cassette sub-family D member 1	P33897
2, Mito-ER	ACBD5 KIAA1996	Acyl-CoA-binding domain-containing protein 5	Q5T8D3
2, Mito-ER	AHSA1 C14orf3	Activator of 90 kDa heat shock protein ATPase homolog 1	O95433
2, Mito-ER	ASS1 ASS	Argininosuccinate synthase	P00966
2, Mito-ER	ATP1A1	Sodium/potassium-transporting ATPase subunit alpha-1	P05023
2, Mito-ER	C11orf49	UPF0705 protein C11orf49	Q9H6J7
2, Mito-ER	CANX	Calnexin	P27824
2, Mito-ER	DHCR7 D7SR	7-dehydrocholesterol reductase	Q9UBM7
2, Mito-ER	ESYT1 FAM62A	Extended synaptotagmin-1	Q9BSJ8
2, Mito-ER	EXD2 C14orf114	Exonuclease 3'-5' domain-containing protein 2	Q9NVH0
2, Mito-ER	GDA KIAA1258	Guanine deaminase	Q9Y2T3
2, Mito-ER	GSPT2 ERF3B	Eukaryotic peptide chain release factor GTP-binding subunit ERF3B	Q8IYD1
2, Mito-ER	HSPA8 HSC70	Heat shock cognate 71 kDa protein	P11142

2, Mito-ER	IPO5 KPNB3	Importin-5	O00410
2, Mito-ER	TMPO LAP2	Lamina-associated polypeptide 2, isoform alpha	P42166
2, Mito-ER	LDHA PIG19	L-lactate dehydrogenase A chain	P00338
2, Mito-ER	MTREX DOB1	Exosome RNA helicase MTR4	P42285
2, Mito-ER	NUP62	Nuclear pore glycoprotein p62	P37198
2, Mito-ER	OSBPL11 ORP11	Oxysterol-binding protein-related protein 11	Q9BXB4
2, Mito-ER	OSBPL1A ORP1	Oxysterol-binding protein-related protein 1	Q9BXW6
2, Mito-ER	PCBP1	Poly(rC)-binding protein 1	Q15365
2, Mito-ER	PCBP2	Poly(rC)-binding protein 2	Q15366
2, Mito-ER	PTPN1 PTP1B	Tyrosine-protein phosphatase non-receptor type 1	P18031
2, Mito-ER	RAB3GAP1 KIAA0066	Rab3 GTPase-activating protein catalytic subunit	Q15042
2, Mito-ER	RMDN2 FAM82A	Regulator of microtubule dynamics protein 2	Q96LZ7
2, Mito-ER	RMDN3 FAM82A2	Regulator of microtubule dynamics protein 3	Q96TC7
2, Mito-ER	RTCB C22orf28	RNA-splicing ligase RtcB homolog	Q9Y3I0
2, Mito-ER	RUVBL1 INO80H	RuvB-like 1	Q9Y265
2, Mito-ER	STIP1	Stress-induced-phosphoprotein 1	P31948
2, Mito-ER	TBC1D4 AS160	TBC1 domain family member 4	O60343
2, Mito-ER	TBRG4 CPR2	FAST kinase domain-containing protein 4	Q969Z0
2, Mito-ER	VAPB UNQ484/PRO983	Vesicle-associated membrane protein-associated protein B/C	O95292
2, Mito-ER	VPS13A CHAC	Vacuolar protein sorting-associated protein 13A	Q96RL7
<hr/>			
2, Endo-ER	ABCF2 HUSSY-18	ATP-binding cassette sub-family F member 2	Q9UG63
2, Endo-ER	CAPN2 CANPL2	Calpain-2 catalytic subunit	P17655
2, Endo-ER	DSC1 CDHF1	Desmocollin-1	Q08554
2, Endo-ER	EGFR ERBB	Epidermal growth factor receptor	P00533
2, Endo-ER	HK2	Hexokinase-2	P52789
2, Endo-ER	HNRNPD AUF1	Heterogeneous nuclear ribonucleoprotein D0	Q14103
2, Endo-ER	TMPO LAP2	Lamina-associated polypeptide 2, isoform alpha	P42166
2, Endo-ER	PAIP1	Polyadenylate-binding protein-interacting protein 1	Q9H074
2, Endo-ER	PTPN1 PTP1B	Tyrosine-protein phosphatase non-receptor type 1	P18031
2, Endo-ER	RMDN3 FAM82A2	Regulator of microtubule dynamics protein 3	Q96TC7
2, Endo-ER	SERPINB6 PI6	Serpin B6	P35237
2, Endo-ER	TTI1 KIAA0406	TELO2-interacting protein 1 homolog	O43156
2, Endo-ER	VAPB UNQ484/PRO983	Vesicle-associated membrane protein-associated protein B/C	O95292
<hr/>			
3, Lyso-ER	ACBD5 KIAA1996	Acyl-CoA-binding domain-containing protein 5	Q5T8D3
3, Lyso-ER	ACTN4	Alpha-actinin-4	O43707
3, Lyso-ER	ALDH1A3 hCG_28035	Aldehyde dehydrogenase 1 family, member A3, isoform CRA_b	H0Y2X5
3, Lyso-ER	ALDH9A1 ALDH4	4-trimethylaminobutyraldehyde dehydrogenase	P49189
3, Lyso-ER	ANXA11 ANX11	Annexin A11	P50995
3, Lyso-ER	APEH D3F15S2	Acylamino-acid-releasing enzyme	P13798
3, Lyso-ER	ARPC2 ARC34	Actin-related protein 2/3 complex subunit 2	O15144
3, Lyso-ER	ASPRV1 SASP	Retroviral-like aspartic protease 1	Q53RT3
3, Lyso-ER	C3 CPAMD1	Complement C3	P01024

3, Lyso-ER	CAP1 CAP	Adenylyl cyclase-associated protein 1	Q01518
3, Lyso-ER	CAPNS2	Calpain small subunit 2	Q96L46
3, Lyso-ER	CISD1 C10orf70	CDGSH iron-sulfur domain-containing protein 1	Q9NZ45
3, Lyso-ER	CNST C1orf71	Consortin	Q6PJW8
3, Lyso-ER	CYB5B CYB5M	Cytochrome b5 type B	O43169
3, Lyso-ER	DDR GK1 C20orf116	DDR GK domain-containing protein 1	Q96HY6
3, Lyso-ER	DEFA3 DEF3	Neutrophil defensin 3	P59666
3, Lyso-ER	DSG4 CDHF13	Desmoglein-4	Q86SJ6
3, Lyso-ER	EFTUD2 KIAA0031	116 kDa U5 small nuclear ribonucleoprotein component	Q15029
3, Lyso-ER	EMD EDMD STA	Emerin	P50402
3, Lyso-ER	EPPK1	Epiplakin	A0A075B7 30
3, Lyso-ER	FGA	Fibrinogen alpha chain	A0A087W UA0
3, Lyso-ER	FGB	Fibrinogen beta chain [Cleaved into: Fibrinopeptide B; Fibrinogen beta chain]	P02675
3, Lyso-ER	FGG	Fibrinogen gamma chain	C9JEU5
3, Lyso-ER	FLNB FLN1L	Filamin-B	O75369
3, Lyso-ER	GNB2	Guanine nucleotide-binding protein G	E7EP32
3, Lyso-ER	H3-3B	Histone H3	K7EK07
3, Lyso-ER	HP	Haptoglobin	A0A087W U08
3, Lyso-ER	IGHG1	Immunoglobulin heavy constant gamma 1	P01857
3, Lyso-ER	IGHM	Immunoglobulin heavy constant mu	P01871
3, Lyso-ER	IGLC3	Immunoglobulin lambda constant 3	P0DOY3
3, Lyso-ER	IMPA2 IMP.18P	Inositol monophosphatase 2	O14732
3, Lyso-ER	IVL	Involucrin	P07476
3, Lyso-ER	TMPO LAP2	Lamina-associated polypeptide 2, isoforms beta/gamma	P42167
3, Lyso-ER	LGALS3 MAC2	Galectin-3	P17931
3, Lyso-ER	LMNA LMN1	Prelamin-A/C [Cleaved into: Lamin-A/C	P02545
3, Lyso-ER	MPO	Myeloperoxidase	P05164
3, Lyso-ER	PCNA	Proliferating cell nuclear antigen	P12004
3, Lyso-ER	PGRMC1 HPR6.6	Membrane-associated progesterone receptor component 1	O00264
3, Lyso-ER	PGRMC2 DG6	Membrane-associated progesterone receptor component 2	O15173
3, Lyso-ER	PLA2G4B	Cytosolic phospholipase A2 beta	P0C869
3, Lyso-ER	PSAPL1	Proactivator polypeptide-like 1 [Cleaved into: Saposin A-like; Saposin B-Val-like; Saposin B-like; Saposin C-like; Saposin D-like]	Q6NUJ1
3, Lyso-ER	PSMC4 MIP224	26S proteasome regulatory subunit 6B	P43686
3, Lyso-ER	RAB2A RAB2	Ras-related protein Rab-2A	P61019
3, Lyso-ER	RAB5A RAB5	Ras-related protein Rab-5A	P20339
3, Lyso-ER	RACGAP1 KIAA1478	Rac GTPase-activating protein 1	Q9H0H5
3, Lyso-ER	RMDN3 FAM82A2	Regulator of microtubule dynamics protein 3	Q96TC7
3, Lyso-ER	RPL26	60S ribosomal protein L26	P61254
3, Lyso-ER	S100A11 MLN70	Protein S100-A11	P31949
3, Lyso-ER	S100A16 S100F	Protein S100-A16	Q96FQ6

3, Lyso-ER	SERPINA1 AAT	Alpha-1-antitrypsin	P01009
3, Lyso-ER	SERPINB5 PI5	Serpin B5	P36952
3, Lyso-ER	SFN HME1	14-3-3 protein sigma	P31947
3, Lyso-ER	SPRR1B	Cornifin-B	P22528
3, Lyso-ER	SPRR2G	Small proline-rich protein 2G	Q9BYE4
3, Lyso-ER	STX1B STX1B1	Syntaxin-1B	P61266
3, Lyso-ER	STXBP1	Syntaxin-binding protein 1	A0A0D9SG 72
3, Lyso-ER	SYF2 CBPIN	Pre-mRNA-splicing factor SYF2	O95926
3, Lyso-ER	TF PRO1400	Serotransferrin	P02787
3, Lyso-ER	TNFRSF10A	Tumor necrosis factor receptor superfamily member 10A	F8U8C0
3, Lyso-ER	TOMM20 KIAA0016	Mitochondrial import receptor subunit TOM20 homolog	Q15388
3, Lyso-ER	TRAPPC3 BET3	Trafficking protein particle complex subunit 3	O43617
3, Lyso-ER	TREX2	Three prime repair exonuclease 2	Q9BQ50
3, Lyso-ER	TRIM29 ATDC	Tripartite motif-containing protein 29	Q14134
3, Lyso-ER	VAPA VAP33	Vesicle-associated membrane protein-associated protein A	Q9P0L0
3, Lyso-ER	VAPB UNQ484/PRO983	Vesicle-associated membrane protein-associated protein B/C	O95292
3, Mito-ER	ACBD5	Acyl-CoA-binding domain-containing protein 5	B7Z2R7
3, Mito-ER	ACBD5 KIAA1996	Acyl-CoA-binding domain-containing protein 5	Q5T8D3
3, Mito-ER	CISD1 C10orf70	CDGSH iron-sulfur domain-containing protein 1	Q9NZ45
3, Mito-ER	CSRP2 LMO5	Cysteine and glycine-rich protein 2	Q16527
3, Mito-ER	CYB5B CYB5M	Cytochrome b5 type B	O43169
3, Mito-ER	DDR GK1 C20orf116	DDR GK domain-containing protein 1	Q96HY6
3, Mito-ER	EMD EDMD STA	Emerin	P50402
3, Mito-ER	ERH	Enhancer of rudimentary homolog	G3V279
3, Mito-ER	H3-3B	Histone H3	K7EK07
3, Mito-ER	IPO5 KPNB3	Importin-5	O00410
3, Mito-ER	JCHAIN	Immunoglobulin J chain	C9JA05
3, Mito-ER	TMPO LAP2	Lamina-associated polypeptide 2, isoforms beta/gamma	P42167
3, Mito-ER	MAVS IPS1	Mitochondrial antiviral-signaling protein	Q7Z434
3, Mito-ER	MTFR1L	Mitochondrial fission regulator 1-like	E9PLD2
3, Mito-ER	MTPN	Myotrophin	P58546
3, Mito-ER	OCIAD1 ASRIJ	OCIA domain-containing protein 1	Q9NX40
3, Mito-ER	PGRMC1 HPR6.6	Membrane-associated progesterone receptor component 1	O00264
3, Mito-ER	PGRMC2 DG6	Membrane-associated progesterone receptor component 2	O15173
3, Mito-ER	RAB2A RAB2	Ras-related protein Rab-2A	P61019
3, Mito-ER	RHOA ARH12	Transforming protein RhoA	P61586
3, Mito-ER	RMDN2 FAM82A	Regulator of microtubule dynamics protein 2	Q96LZ7
3, Mito-ER	RMDN3 FAM82A2	Regulator of microtubule dynamics protein 3	Q96TC7
3, Mito-ER	RNF114	E3 ubiquitin-protein ligase RNF114	A0A096LN V3
3, Mito-ER	RPL27A	60S ribosomal protein L27a	E9PLL6

3, Mito-ER	RRP15 KIAA0507	RRP15-like protein	Q9Y3B9
3, Mito-ER	SERPINA1 AAT	Alpha-1-antitrypsin	P01009
3, Mito-ER	SPRR2G	Small proline-rich protein 2G	Q9BYE4
3, Mito-ER	TRAPPC3 BET3	Trafficking protein particle complex subunit 3	O43617
3, Mito-ER	TTC1 TPR1	Tetratricopeptide repeat protein 1	Q99614
3, Mito-ER	UBE2I	SUMO-conjugating enzyme UBC9	H3BPC4
3, Mito-ER	VAPA VAP33	Vesicle-associated membrane protein-associated protein A	Q9P0L0
3, Mito-ER	VAPB UNQ484/PRO983	Vesicle-associated membrane protein-associated protein B/C	O95292
<hr/>			
3, Endo-ER	COMT	Catechol O-methyltransferase	P21964
3, Endo-ER	CS	Citrate synthase	A0A0C4DG I3
3, Endo-ER	CSRP2 LMO5	Cysteine and glycine-rich protein 2	Q16527
3, Endo-ER	DSG4 CDHF13	Desmoglein-4	Q86SJ6
3, Endo-ER	EGFR ERBB	Epidermal growth factor receptor	P00533
3, Endo-ER	EIF3C EIF3S8	Eukaryotic translation initiation factor 3 subunit C	Q99613
3, Endo-ER	GDA KIAA1258	Guanine deaminase	Q9Y2T3
3, Endo-ER	HP	Haptoglobin	A0A087W U08
3, Endo-ER	IGHM	Immunoglobulin heavy constant mu	P01871
3, Endo-ER	IVL	Involucrin	P07476
3, Endo-ER	JCHAIN	Immunoglobulin J chain	C9JA05
3, Endo-ER	PFAS KIAA0361	Phosphoribosylformylglycinamide synthase	O15067
3, Endo-ER	PGRMC1 HPR6.6	Membrane-associated progesterone receptor component 1	O00264
3, Endo-ER	RTF2 C20orf43	Replication termination factor 2	Q9BY42
3, Endo-ER	SERPINA1 AAT	Alpha-1-antitrypsin	P01009
3, Endo-ER	TRAPPC3 BET3	Trafficking protein particle complex subunit 3	O43617

## ImageJ Macro-Script used to analyse LDL/GFP data (also shown below)

```
// Images of two channels must be saved as image sequences in separate folders
// Global paramters:
pxs=0.05; //pixel size in µm

d0=pxs*20*15; //radius of first circle
d1=pxs*20*25; //radius of second circle
d2=pxs*20*100; //radius of third circle
dn=3; //number of circles

waitForUser("Close ROI manager? Open particle images")
run("Image Sequence...");
dir = getDirectory("image");
File.makeDirectory(dir+"/Maxima");
File.makeDirectory(dir+"/singleROIs");
setSlice(1);
print("nSlices =" + nSlices);

//find maxima and draw regions of interest
//first circle
for (i=1; i<=nSlices; i++){
    run("Find Maxima...", "noise=20 output=List exclude");
    print("nResults = " + nResults);
    List.set(i,nResults);
    for (n=0; n< nResults; n++) {
        x= getResult("X", n);
        y= getResult("Y", n);
        print(n+1+": x="+x+", y="+y);
        makeOval(x-(d0/2), y-(d0/2), d0, d0);
        roiManager("Add");
    }
    saveAs("Results", dir+"/Maxima/locations"+i+".txt");
    run("Select None");
    run("Next Slice [>]");
}
list = List.getList();
print(list);

setSlice(1);
//second circle
for (i=1; i<=nSlices; i++){
    run("Find Maxima...", "noise=20 output=List exclude");
    print("nResults = " + nResults);
    List.set(i,nResults);
    for (n=0; n< nResults; n++) {
        x= getResult("X", n);
        y= getResult("Y", n);
        print(n+1+": x="+x+", y="+y);
        makeOval(x-(d1/2), y-(d1/2), d1, d1);
        roiManager("Add");
    }
    saveAs("Results", dir+"/Maxima/locations"+i+".txt");
    run("Select None");
    run("Next Slice [>]");
}
list = List.getList();
```

```

print(list);
setSlice(1);

//third circle
for (i=1; i<=nSlices; i++){
    run("Find Maxima...", "noise=20 output=List exclude");
    print("nResults = " + nResults);
    List.set(i,nResults);
    for (n=0; n< nResults; n++){
        x= getResult("X", n);
        y= getResult("Y", n);
        print(n+1+": x="+x+", y="+y);
        makeOval(x-(d2/2), y-(d2/2), d2, d2);
        roiManager("Add");
    }
    run("Select None");
    run("Next Slice [>]");
}

//measure signal of ROIs in LDL channel as a quality control
c=0;
for (d=1; d<=dn; d++){
    setSlice(1);
    for (j=0; j<nSlices;j++){
        run("Select All");
        run("Measure");
        run("Next Slice [>]");
    }
    saveAs("Results", dir+"/singleROIs/Measurement-Results_total.txt");
    run("Clear Results");
    setSlice(1);

    for (j=0; j<nSlices;j++){
        resultnr= List.get(j+1);
        print ("Slice "+j+": "+resultnr+"results");
        for (m=0; m<resultnr; m++){
            roiManager("Select", c);
            print("c="+c);
            run("Measure");
            c=c+1;
        }
        run("Next Slice [>]");
    }
    saveAs("Results",
    dir+"/singleROIs/Measurement-Results_All-ROIs_"+d+".txt");
    run("Clear Results");
}
close();

//Open GFP images
waitForUser("Don't close ROI manger! Open GFP images")
run("Image Sequence...");
dir = getDirectory("image");
File.makeDirectory(dir+"/singleROIs");

c=0;
//measure total signal for all slices
for (d=1; d<=dn; d++){
    setSlice(1);
    for (j=0; j<nSlices;j++){

```

```

        run("Select All");
        run("Measure");
        run("Next Slice [>]");
    }
    saveAs("Results",
    dir+"/singleROIs/Measurement-Results_total.txt");
    run("Clear Results");
    setSlice(1);

    //measure signal in all previously recorded ROIs
    for (j=0; j<nSlices;j++){
        resultnr= List.get(j+1);
        print ("Slice "+j+": "+resultnr+"results");
        for (m=0; m<resultnr; m++){
            roiManager("Select", c);
            print("c="+c);
            run("Measure");
            c=c+1;
        }
        run("Next Slice [>]");
    }

    saveAs("Results", dir+"/singleROIs/Measurement-Results_All-ROIs_"+d+".txt");
    run("Clear Results");
}
close();

//Re-open LDL images for random measurements

waitForUser("Close ROI manager! Open particle images")
run("Image Sequence...");
dir = getDirectory("image");
File.makeDirectory(dir+"/Maxima");
File.makeDirectory(dir+"/singleROIs");
setSlice(1);
print("nSlices =" + nSlices);

for (i=1; i<=nSlices; i++){
    run("Find Maxima...", "noise=20 output=List exclude");
    print("nResults = " + nResults);
    List.set(i,nResults);
    for (n=0; n< nResults; n++){
        x= getResult("X", n) + ((random()*200)-100);
        //shifts X by random number between -100 and +100
        y= getResult("Y", n) + ((random()*200)-100);
        //shifts Y by random number between -100 and +100
        print(n+1+": x="+x+", y="+y);
        makeOval(x-(d0/2), y-(d0/2), d0, d0);
        roiManager("Add");
        makeOval(x-(d1/2), y-(d1/2), d1, d1);
        roiManager("Add");
        makeOval(x-(d2/2), y-(d2/2), d2, d2);
        roiManager("Add");
    }
    saveAs("Results", dir+"/Maxima/locations"+i+".txt");
    run("Select None");
    run("Next Slice [>]");
}
list = List.getList();

```

```

print(list);

setSlice(1);

c=0;

setSlice(1);
for (j=0; j<nSlices;j++){
    run("Select All");
    run("Measure");
    run("Next Slice [>]");
}
saveAs("Results", dir+"/singleROIs/Measurement-Results_total.txt");
run("Clear Results");
setSlice(1);

for (j=0; j<nSlices;j++){
    resultnr= List.get(j+1);
    print ("Slice "+j+": "+resultnr+"results");
    for (m=0; m<resultnr; m++){
        roiManager("Select", c);
        print ("c="+c);
        run("Measure");
        c=c+1;
        roiManager("Select", c);
        print ("c="+c);
        run("Measure");
        c=c+1;
        roiManager("Select", c);
        print ("c="+c);
        run("Measure");
        c=c+1;
    }
    run("Next Slice [>]");
}
saveAs("Results", dir+"/singleROIs/Measurement-Results_All-ROIs_"+d+".txt");
run("Clear Results");

close();

waitForUser("Open GFP images")
run("Image Sequence...");
dir = getDirectory("image");
File.makeDirectory(dir+"/singleROIs");

c=0;

setSlice(1);
for (j=0; j<nSlices;j++){
    run("Select All");
    run("Measure");
    run("Next Slice [>]");
}
saveAs("Results", dir+"/singleROIs/Measurement-Results_total.txt");
run("Clear Results");
setSlice(1);

for (j=0; j<nSlices;j++){
    resultnr= List.get(j+1);

```

```

//careful, entries in ROI manager are in different order than before
//measure all circles for each location, then advance to next

print ("Slice "+j+": "+resultnr+"results");
for (m=0; m<resultnr; m++) {
    roiManager("Select", c);
    print("c="+c);
    run("Measure");
    c=c+1;
    roiManager("Select", c);
    print("c="+c);
    run("Measure");
    c=c+1;
    roiManager("Select", c);
    print("c="+c);
    run("Measure");
    c=c+1;
}
run("Next Slice [>]");
}

saveAs("Results", dir+"/singleROIs/Measurement-Results_All-ROIs_rand.txt");
run("Clear Results");
close();
waitForUser("Done!")

```

## Acknowledgements

I am very thankful to Doris Höglinger, who gave me the opportunity to work on this project, while letting me climb my way up to my personal “Mount PhD” at my own pace on the paths I choose for myself. No matter where or how, she always remained available with two open ears and hands full of nudges towards the more fruitful paths.

Special thanks also goes to Britta Brügger and Sebastian Schuck for their scientific input as members of my Thesis Advisory Committee and as reviewers of this dissertation and to Daniela Mauceri for agreeing to be part of my defense committee.

I am also grateful to all my former and current colleagues in the Höglinger lab for the stimulating work atmosphere they created and especially to Jutta for taking a huge load off everyone’s mind and back and for providing us with our weekly rations of cookies.

Further, I want to thank all the people of the third floor for their open ears and helping hands. Here, special thanks goes to Julien Béthune and his whole group for the help with the Split-BioID assays and all the chai lattes, laughs and gossip.

I also thank our collaborators in Berlin, Benno Kuroпка in the group of Christian Freund and Helge Ewers, as well as the Heidelberg Core facilities for Mass Spectrometry and Cell Sorting.

I want to thank all the friends I made during my time here and the ones who came before them, for staying with me during late nights and early mornings, patiently listening to my frustrations randomly mixed with rambling lectures about recipes, ramen and fermentation. Naturally, the same level of gratitude goes to my family, who has been equally patient, understanding and helpful this whole time.

Most importantly though, I want to thank my mother and my wife Janine for their endless support and always believing in me no matter what. You two made me who I am and I could not have done it without either of you.